

Novel Pyroelectric and Switched Ferroelectric Ion Sources in Mass Spectrometry: Implementation and Applications

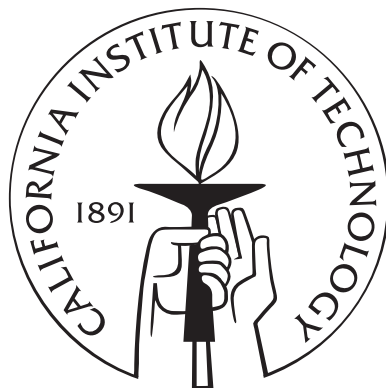
Thesis by

Evan L. Neidholdt

In Partial Fulfillment of the Requirements

for the Degree of

Doctor of Philosophy



California Institute of Technology

Pasadena, California

2010

(Defended January 21, 2010)

© 2010

Evan L. Neidholdt

All Rights Reserved

For April
and In Loving Memory of

Charles R. Downs
1923-2007

M. June Sinning
1927-2008

Hank G. Germon
1930-2007

It was two weeks from the date I submitted my application to the graduate program in Chemistry at Caltech when I received a call from Mitchio Okumura, with the message that I was accepted into the Chemistry option at Caltech. In another two weeks, I would then receive a condolences letter from Stanford that I wasn't accepted into their program. In an exercise in 'Acceptance Letter Logic,' (not to be confused with 'relay logic' or 'transistor-transistor-logic') it became apparent that Caltech was my future. The solution was further defined and bounded because this was truly the 'reach' school in my graduate school applications, and the one to which I would be a damn fool if I didn't attend.

I have not strayed from this opinion for my entire tenure here at Caltech. From the first year here, when I was fortunate enough to take a chemical kinetics course and learn RRKM theory from the 'M' himself, to my last years, characterized by fruitful collaboration with members within and outside of the Chemistry department, I attribute my success to the sum total of interactions between myself and those around me. There are several people that deserve direct acknowledgment for contribution to my success in graduate school at Caltech.

Chemistry Instrument Shop staff Mike Roy and Steve Olson, for expert production of necessary parts for my often mechanically convoluted experimental setups; as well as guidance when I decided to machine my own parts;

Chemistry Electronics Shop lead Tom Dunn, for much needed advice and electronics book loans when I faced a unique challenge in my electronics projects;

Current and past members of the Beauchamp group at Caltech, including Changho Sohn, Hugh Kim, Ron Grimm, Rob Hodyss, Heather Sumner, Lin Feng, and Tae-Young Kim, for many excellent collaborations (Rob and Heather: FRIPS; Ron, Hugh, Changho, Tae-Young: FIDI) and discussions about science and for sometimes helping me forget about science for a little while;

My good friends in the Atwater Group at Caltech, especially Mike Kelzenberg, Gerald Miller, Ryan Briggs, and Ken Diest for the same;

Nathan Dalleska of the Caltech Environmental Analysis Center for his expertise in classic analytical chemistry, as well as for excellent collaborations;

Prof. Ryan Julian, UC Riverside (also a former Beauchamp group member) for discussions and article preprints regarding free radical chemistry;

My summer students in the Caltech SURF and MURF programs Eleanor Waxman, Jillian Thayer, Diane Plummer, Kristin Whitely, and Tony Jia (Caltech Amgen Scholar) for fruitful collaboration. Jillian and I worked on studies utilizing the FRIPS methodology, while Diane and I worked on site-specific cleavage at aspartic acid sites in peptides with multiple aspartic acid residues. Eleanor and I worked on ozonolysis of peptides using FIDI; Kristin and I explored using 18-crown-6 ether as a sensitivity enhancer when performing ESI on neurotransmitters. Tony and I worked on FIDI, exploring selectivity of ionization for surface active species.

Nick Brunelli, for excellent collaboration and measurements with his nanoRDMA instrument;

Pete Schultz, for encouraging me to apply to graduate schools I'd never thought I could get into;

John W. Kenney III, for expert training in the finer points of experimental science while I was an undergraduate;

and my adviser, Jack Beauchamp. Jack's experience and insight are invaluable, and I thank him for keeping me focused on the important things in my projects. Specifically, I think Jack has an eye for avoiding getting caught up in periphery and instead striving to tell a good story about the research.

More extensive mention and thanks go to my wife April. Without the support and encouragement of her and her family, I would not have found in myself the courage, motivation, and emotional toughness necessary to successfully complete a Ph.D. at Caltech. I have dedicated this thesis (and by extension all my work at Caltech) to April as well as to the memory of her grandparents, all of whom were there to tell me how proud they were of me in the way only grandparents can. I can't thank them and the rest of the family enough.

Abstract

Instrumentation development for ambient mass spectrometry is an ever-changing and ever-growing field, often emphasizing the development of field-portable, ruggedized instrumentation. This thesis presents work in the area of ion source development. Specifically, two novel ionizers for mass spectrometry are constructed, implemented, and tested on a variety of systems. The first, the ambient pressure pyroelectric ion source (APPIS) comprises a z-cut lithium niobate or lithium tantalate pyroelectric crystal which is subjected to thermal cycling. Thermal cycling and the pyroelectric effect result in the buildup of excess charge on the z-faces of the material. For a temperature change of only 30 K, an electrical potential as high as 7.0×10^4 V could be built up if no discharging occurs. At ambient pressure, electrical discharges occur between the oppositely charged crystal faces and regions of different potentials on the same crystal face. Monitoring of the discharges using an inductive pickup reveals that the time frame of ion production corresponds to that of electrical activity on the crystal face. Additionally, the ions observed in the mass spectra differ when different ambient gas compositions are present. This, and comparison to APCI experiments reveals that ionization with APPIS is a gas phase process and observed product ion species are highly dependent on ambient gas composition. An application of APPIS, whereby APPIS is used as an ion source for the detection of chemical warfare agents, is presented. Agents in the V and G classes possess amine functionality, and as a result have relatively high proton affinities and are well suited to ionization and detection using chemical ionization with APPIS. Simulants for the nerve agents VX and Tabun were detected as singly protonated species using APPIS. A second ion source for ambient mass spectrometry is also presented, the switched ferroelectric

plasma ionizer (SwiFerr). The source comprises a 1 mm thick plate of barium titanate with an electrode on one face and a grounded metallic grid on the opposite face. If an audio frequency high voltage waveform is applied to the electrode, domain structure is formed and the high electric fields across domain walls give rise to electron emission and plasma formation. At ambient pressure, the plasma produces chemical ionization reagent ions which participate in proton transfer reactions with trace species in ambient air. The source is useful for examining organic vapors and solid samples. Solid sampling is achieved through use of a pneumatic aspirator, which can aspirate powders into the SwiFerr source for analysis. Powders of the drugs loperamide and ibuprofen were ionized and detected using SwiFerr. A second-generation SwiFerr source has been designed and implemented, and is described. The second-generation source is constructed in a unibody fashion, such that the rear electrode, grid, and electrical contact wires are attached as a single unit using conductive adhesives. This allows for a source which is further miniaturized and capable of insertion into a standard Swagelok fitting, for ease of integration into existing instrumentation. The source is particularly sensitive, and an application involving detection of trace explosives is presented. Nanogram quantity samples of TNT were ionized and detected with SwiFerr after volatilization using a rudimentary thermal desorption apparatus. Sensitive detection of TNT suggests use of SwiFerr in applications where sensitive detection in field portable instrumentation is desired. To this end, plans for a stand-alone power supply for this ionizer as well as a supply designed for operating the source in a constant discharge mode at low power are presented in an appendix. Additional work not related to ion source development is also presented in this thesis. Chapter 6 presents advances in free radical initiated peptide sequencing (FRIPS). The 20 amino acid basis set has been analyzed for reactivity with acetyl radical, and distinct reactivity classes are observed. Chapter 7 presents a study of regioselective cleavage at aspartic acid residues by various cations. Selective cleavage at aspartic acid is observed for any cation which is not mobile along the peptide backbone, and fragmentation proceeds through a salt bridge mechanism.

Contents

Abstract	vi
List of Figures	xi
List of Tables	xv
List of Schemes	xvi
1 Introduction	1
2 Compact Ambient Pressure Pyroelectric Ion Source for Mass Spectrometry	7
2.1 Introduction	8
2.2 Experimental	8
2.3 Results and Discussion	12
2.4 Conclusion	18
3 Ionization Mechanism of the Ambient Pressure Pyroelectric Ion Source (APPIS) and Its Applications to Chemical Nerve Agent Detection	19
3.1 Introduction	20
3.2 Experimental	21
3.3 Results and Discussion	24
3.4 Conclusion	31

4	Switched Ferroelectric Plasma Ionizer (SwiFerr) for Ambient Mass Spectrometry	34
4.1	Introduction	35
4.2	Experimental	38
4.2.1	Design and construction of SwiFerr ionizer	38
4.3	Results and Discussion	41
4.3.1	Ambient ionization of vapor phase and solid samples	41
4.3.2	Limit of detection for organic vapors	44
4.3.3	Optimization of parameters for source operation	44
4.4	Conclusion	47
5	Second-Generation Switched Ferroelectric Source and its Application to Trace Explosives Detection	49
5.1	Introduction	50
5.2	Experimental	54
5.3	Results and Discussion	56
5.3.1	Limit of detection for organic vapors	59
5.3.2	Capacitance of revised source; Power usage	59
6	Free Radical Initiated Peptide Sequencing: Reactions of Carbon Centered Radicals with Amino Acids in Model Peptides	63
6.1	Introduction	64
6.2	Experimental	66
6.3	Results and Discussion	68
6.3.1	Peptides containing residues X=G,A,P	68
6.3.2	Peptides containing residues X=D,N,H,Y,F,V,W	71
6.3.3	Peptides containing residues X=S,T	76
6.3.4	Peptides containing residues X=K,Q,E,R,M,C,I,L	76
6.4	Conclusion	78

7	Regioselective Cleavage at Aspartic Acid Sites in Model Peptides	87
7.1	Introduction	87
7.2	Experimental	89
7.3	Results and Discussion	90
7.3.1	Cleavage of protonated (AAD) ₅ AA	90
7.3.2	Cleavage of the peptide (AAD) ₅ AA with sodium cation	90
7.3.3	(AAD) ₅ AAR, R(AAD) ₅ AA,R(AAD) ₅ AAR	94
7.3.4	Cleavage of the peptide (AAD) ₅ AA by the guanidinium ion	97
7.4	Conclusion	100
A	Electronics and Experimental Designs for Improved Operation of SwiFerr and APPIS	101
A.1	Introduction	102
A.2	Experimental	103
A.2.1	Design and construction of drift cell	103
A.3	Results and Discussion	103
A.3.1	Rate of ion production with APPIS; Increasing rate with appropriate grid	103
A.3.2	Operation of SwiFerr using a ‘stand alone’ power supply	107
A.3.3	Timescale of discharge with SwiFerr; Constant discharge mode SwiFerr	108
A.4	Statistical Methods	116
B	Pulsed High Voltage Power Supply for Field Induced Droplet Ionization Experiments	124
B.1	Introduction	124
B.2	Component Reduction; Supply Changes	126
B.3	Description of Instrument	126
B.3.1	Global control design	128
B.3.2	Hardware interface	128
B.4	Experiment Start-Up Procedures	130

List of Figures

1.1	Liquid nitrogen cooled pyroelectric crystal allowed to warm in air . . .	3
1.2	Pyroelectric crystal with layer of grease on surface	3
1.3	Visualization of a switched ferroelectric plasma using a 60 second photographic exposure	4
1.4	Miniaturized SwiFerr source and housing next to a dime for scale . . .	4
2.1	Schematic of APPIS source	9
2.2	Charging of crystal faces on temperature change	11
2.3	Negative ion mass spectrum of 1,1,1,3,3,3-hexafluoroisopropanol and temporal variation of total ion yield as the crystal is cooled	13
2.4	Negative ion mass spectrum of sublimed benzoic acid and temporal variation of total ion yield as the crystal is cooled	14
2.5	Positive ion mass spectrum of triethylamine and temporal variation of ion yield as the crystal is heated	15
2.6	Positive ion mass spectrum of triphenylamine and temporal variation of ion yield as the crystal is heated	16
3.1	Generation Two APPIS apparatus	22
3.2	Temporal variation of induction current and ion signal for cations and anions	25
3.3	Comparison of signal resultant from APPIS and APCI under different sampling conditions	27
3.4	Mass spectrum of BAET (simulant for VX) and DEPA (simulant for Tabun)	30

3.5	Mass spectrum of 4 ppm pyridine in doped nitrogen.	32
4.1	Domain formation in a switched ferroelectric	36
4.2	Schematic of SwiFerr source	39
4.3	Mass spectra of test compounds using SwiFerr	42
4.4	Reactant ions observed for SwiFerr	43
4.5	Positive mode mass spectrum of 4 ppm pyridine in nitrogen	45
4.6	Power consumption of SwiFerr source	46
5.1	Miniaturized SwiFerr source near a dime for scale	52
5.2	Schematic of second-generation SwiFerr ion source	53
5.3	Mass spectrum of 4-cyanobenzoic acid by thermal desorption SwiFerr MS	57
5.4	Mass spectrum of 20 ng TNT using thermal desorption SwiFerr	58
5.5	Mass spectrum of diethyl ether at 2 ppm and correlation of signal with concentration	60
5.6	Variation of power consumed with frequency	61
6.1	FRIPS spectrum of model peptide AARAAAPAA	69
6.2	Bar graph showing relative intensities for residues losing 44 amu	70
6.3	FRIPS spectrum of AARAAAYAA	72
6.4	Chart showing relative abundances of products for those residues react- ing to form M_{a7} fragments	73
6.5	Correlation of $\beta\text{H-C}$ bond dissociation energies with observed backbone fragmentation	75
6.6	FRIPS spectra of AARAAASAA and AARAAATAA	77
6.7	Graph showing relative abundances of products resulting from side chain losses in the Xth residue	81
6.8	FRIPS spectra of AARAAALAA and AARAAIAA	82
7.1	Mass spectrum and CAD spectrum of the peptide $(\text{AAD})_5\text{AA}$	91
7.2	Cleavage of model peptide by sodium ion	92

7.3	Cleavage of protonated model peptide with arginine on either terminal end	95
7.4	Cleavage of singly and doubly charged R(AAD) ₅ AAR	96
7.5	Cleavage of model peptide by guanidinium cation	99
A.1	Schematic and photo of drift cell	104
A.2	Plot relating heating rate to ion production for a pyroelectric crystal .	105
A.3	Schematic for a stand-alone power supply for SwiFerr	109
A.4	Circuit for monitoring discharge current in SwiFerr experiment	110
A.5	Discharge profiles for SwiFerr at various frequencies	111
A.6	Simulated three phase excitation and resulting discharge	113
A.7	Schematic for three-phase generator	114
B.1	Original arrangement for supplying high voltage to FIDI source	127
B.2	Revised arrangement for supplying high voltage to the FIDI source . .	127
B.3	Photograph of pulsed power supply	131
B.4	Screen shot of control program for the experiment	132
B.5	Control circuitry for FIDI power supply	133
B.6	Schematic of circuit board in supply	134

List of Tables

3.1	Summary for the detection of CBW agent simulants by APPIS	30
6.1	Relative abundances of products observed from activation of model peptides containing X=G,A,P	84
6.2	Relative abundances of products observed from activation of model peptides containing X=D,N,H,Y,F,V,W	85
6.3	Relative abundances of products observed from activation of model peptides containing X=K,Q,E,R,M,C	86
A.1	Data for .1365 K per second	117
A.2	Data for .1527 K per second	117
A.3	Data for .1655 K per second	118
A.4	Data for .19 K per second	118
A.5	Data for .1907 K per second	119
A.6	Data for .2188 K per second	119
A.7	Data for .2651 K per second	120
A.8	Data for .27 K per second	120
A.9	Data for .3265 K per second	121
A.10	Data for .4368 K per second	121
A.11	Data for .6447 K per second	122
A.12	Data for 2.333 K per second	122
A.13	Data for 4 K per second	123
B.1	Pinouts for FIDI pulsed high voltage supply.	129

List of Schemes

6.1	Formation of acetyl radical conjugated to model peptide	67
6.2	Scheme for formation of Ma_n fragments by hydrogen abstraction followed by beta cleavage	74
6.3	Scheme for formation of c and a6 fragments for serine, threonine	80
6.4	Proposed mechanism for cleavage near isoleucine and leucine	83
7.1	Proposed mechanism for cleavage with a salt bridge intermediate for both sodium cation and protonated arginine	93
7.2	Proposed mechanism for cleavage by complexed guanidinium ion	98

Chapter 1

Introduction

Mass spectrometry has become a nearly universal tool in the field of chemical analysis. A very important use of the technique is for the identification of trace substances in the field. Performing a measurement without advanced sample preparation is often desired, as it is very often practical and convenient to avoid sample pre-processing. Mass spectrometric analysis without advanced sample preparation is termed ambient mass spectrometry owing to the fact that the necessary ionization and volatilization of the sample occurs at ambient pressure (approximately 1 atmosphere or 1.01×10^5 Pa on Earth). The subsequent ions for analysis are transferred from ambient pressure into vacuum where they are analyzed. Development of instrumentation for ambient mass spectrometry is an ever-changing and constantly growing field. All aspects, from the front-end ionizer to the back-end vacuum system are under constant development with the common goal of achieving simpler, more robust, and efficient instrumentation which can be implemented in future portable and ruggedized instrumentation. A portion of this thesis presents work pertaining to ambient pressure ion source development for mass spectrometry with a particular focus on miniaturization and minimization of power consumption for the devices.

Chapters 2 through 6 describe two novel ion sources for ambient mass spectrometry, the ambient pressure pyroelectric ion source (APPIS) and the switched ferroelectric plasma ionizer (SwiFerr). Chapter 2 describes the initial implementation and studies with APPIS, including ionization of some acidic and basic species such as amines and carboxylic acids. Chapter 3 details a study of ionization mechanism

operative in APPIS, as well as presents an application of APPIS, the detection of chemical warfare agents. APPIS is an ambient pressure ion source which utilizes the pyroelectric properties of lithium niobate or lithium tantalate to form ions from trace species in ambient air. Pyroelectricity is a property which is derived from crystal structure asymmetry, and the rearrangement of that crystal structure upon temperature cycling in the material. The result is the formation of net electrical potential on the order of 10^5 V on the faces of the crystal with a temperature change of as little as 30 K. A way to visualize the electric fields resulting from the pyroelectric effect is by immersing the crystal in liquid nitrogen and allowing it to warm up in air. Ice crystals form, and align themselves along electric field lines. Figure 1.1 is a photograph of a 4 x 6 x 5 mm crystal of lithium niobate which was immersed in liquid nitrogen and allowed to warm in air. The formed ice crystals have spontaneously oriented themselves along the electric field lines between the two z-faces of the material due to the electric field present between the two crystal faces.

The pyroelectric ion source has also proven quite robust in practical use. Contamination of the crystal face with dirt or grease appears not to affect source performance. Figure 1.2 is a photograph of a lithium tantalate crystal with a layer of Dow Corning silicone vacuum grease applied to it. Electrical discharges and ion production were observed in spite of the coating on the crystal surface, suggesting that APPIS may find application in harsh environments.

The switched ferroelectric plasma ionizer (SwiFerr) is an ion source for ambient mass spectrometry which utilizes the unique properties of ferroelectric materials to form a self-igniting, low-power plasma on the surface of the material and create ions by ambient pressure chemical ionization. By applying an audio frequency high voltage waveform to one face of the crystal with a grounded metal grid on the other face, domains are formed and electron emission and plasma result from the high electric fields across domain walls. Photography using a relatively long exposure time allows for the direct visualization of the plasma, seen as white light emanating from near the grid wires in the false-color photograph shown in Figure 1.3.

Chapter 4 details the construction and initial implementation of SwiFerr, as well

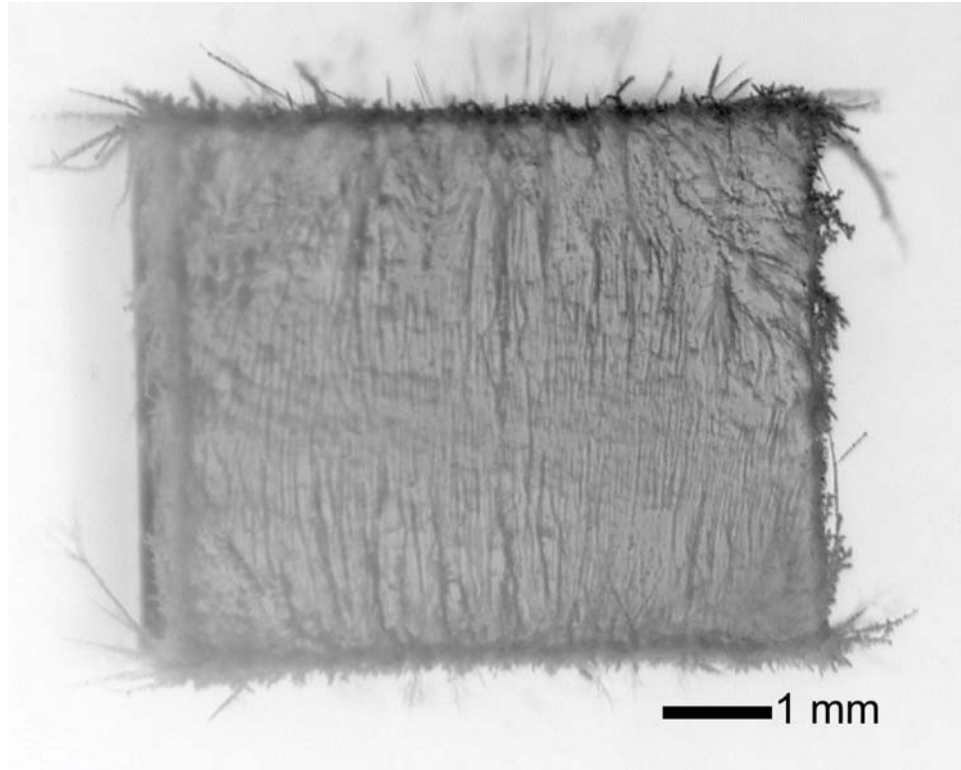


Figure 1.1: Liquid nitrogen cooled pyroelectric crystal allowed to warm in air

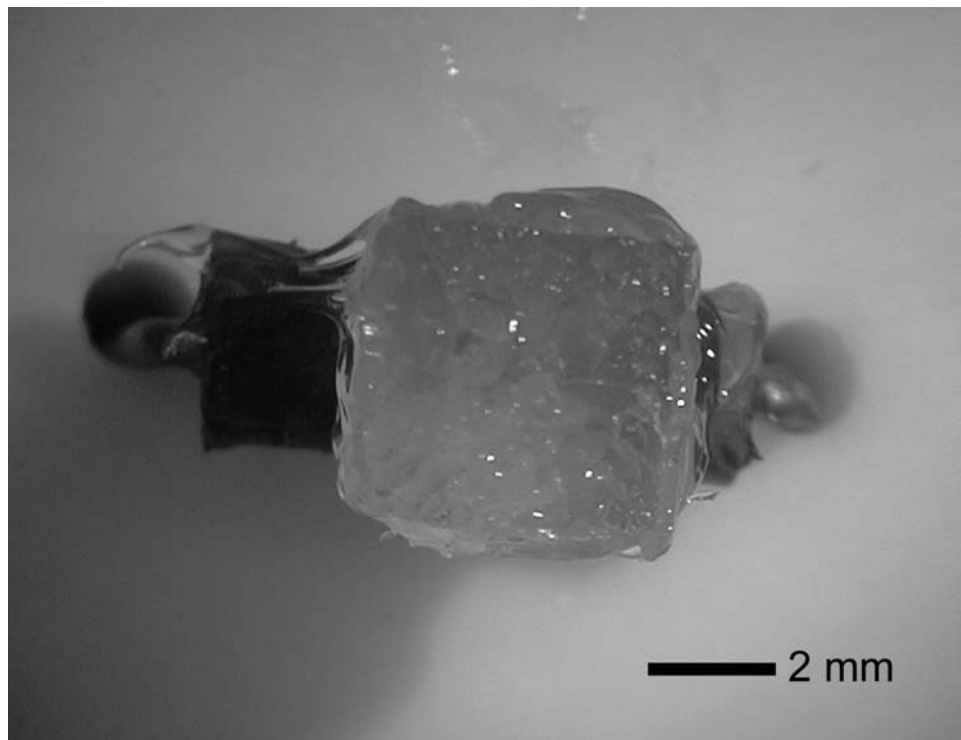


Figure 1.2: Pyroelectric crystal with layer of grease on surface

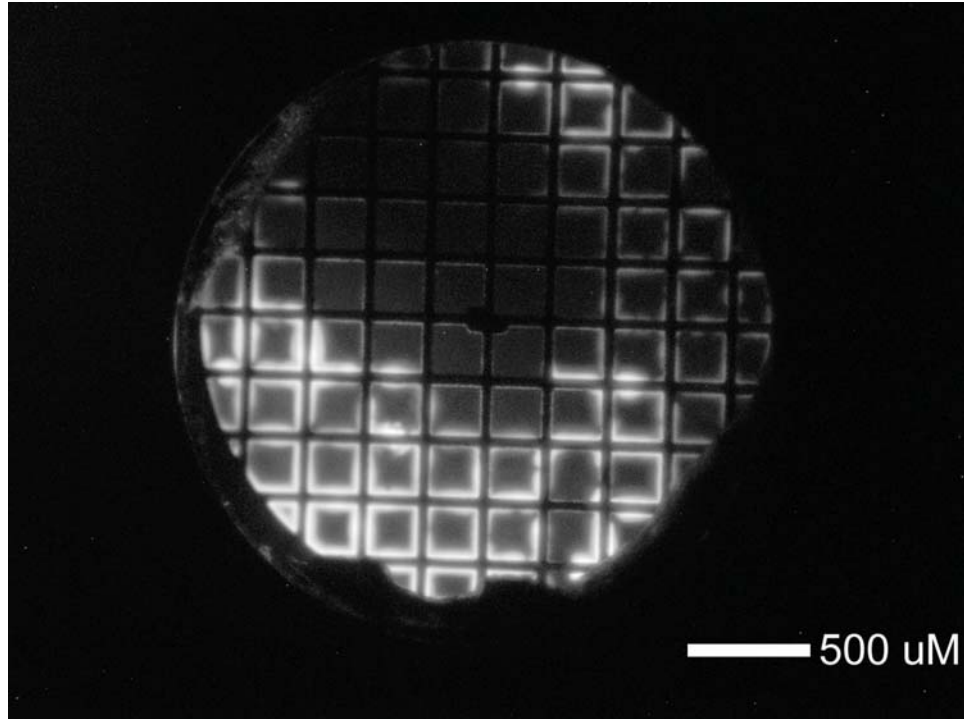


Figure 1.3: Visualization of a switched ferroelectric plasma using a 60 second photographic exposure

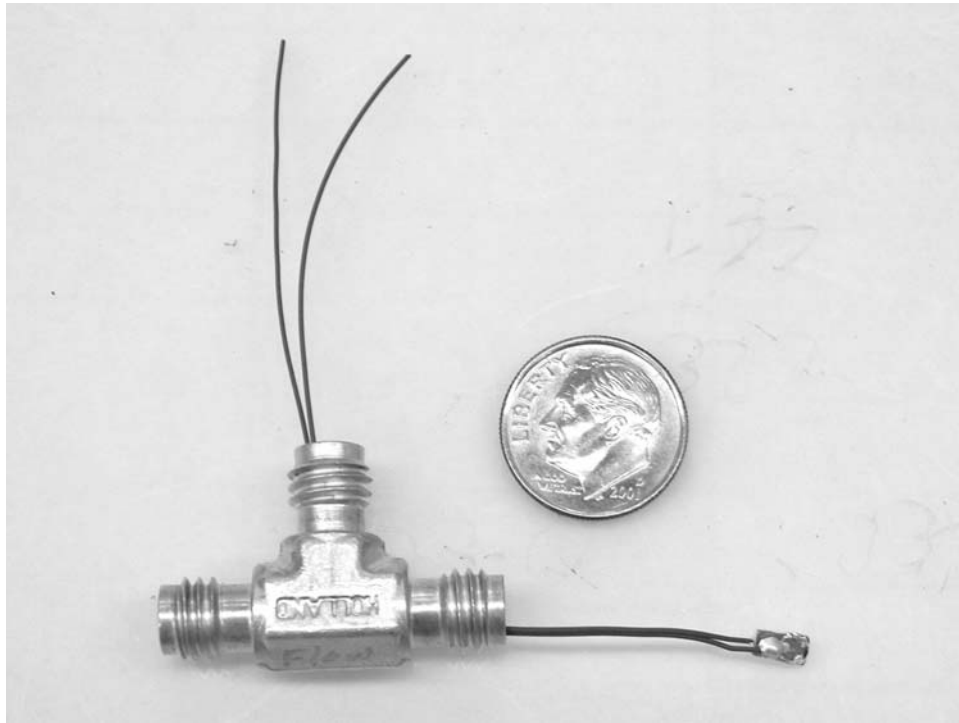


Figure 1.4: Miniaturized SwiFerr source and housing next to a dime for scale

as demonstrating the direct sampling of powders using the source. Chapter 5 describes the second-generation SwiFerr source, detection limits for the revised design, and an application of SwiFerr to practical analytical chemistry, which is the detection of explosives materials using SwiFerr. The first SwiFerr source utilizes a 5 x 5 x 1 mm thick plate of barium titanate (BaTiO_3) with machined mounting hardware which attaches directly to the atmospheric pressure inlet of an ion trap mass spectrometer. The second design SwiFerr source utilizes a crystal half the size, and is constructed using adhesives for an integrated mounting and electrical contacting package. The second design source fits inside a 1/8" Swagelok tee fitting, which allows for ease of integration and total sealing of the source region for purity and rejection of background species. Figure 1.4 is a photograph of the miniaturized source near a dime for scale, and the source is considerably smaller than the coin itself.

Other studies in this thesis not related to pyroelectric or switched ferroelectric ion sources are presented in Chapters 6 and 7. Chapter 6 describes advances in free radical initiated peptide sequencing (FRIPS), where model peptides containing each of the 20 common amino acids were analyzed for reactivity toward acetyl radical. Separate classes of reactions are observed for the same free radical which are selective for certain amino acids. Chapter 7 is a study of regioselective (residue specific) cleavage at aspartic acid sites in peptides containing multiple aspartic acid residues. Cleavage by a mobile proton, a tethered proton, sodium cation, and guanidinium ion is observed and differences in reactivity are noted between the different classes of cations.

Appendix A presents ideas for further work with both APPIS and SwiFerr. For APPIS, an embodiment involving a grounded grid on the surface of the material to enhance discharging during negative charge buildup is presented. For SwiFerr, schematics for a stand-alone power supply for the experiment as well as plans for a power supply for a constant-discharge operating mode is presented. It appears possible to produce a stable, self-igniting plasma at ambient pressure consuming only 0.10 W of power.

Appendix B presents the design and construction of a computer controlled, pulsed

power supply for the field induced droplet ionization (FIDI) experiment. Previous iterations of the experiment utilized manually controlled electronics, and after continued use in the lab suffered reliability problems. The current experiment employs a power supply which is computer controlled and considerably simpler than the original. Wiring diagrams for the control electronics as well as electrical schematics are included for future reference.

Chapter 2

Compact Ambient Pressure Pyroelectric Ion Source for Mass Spectrometry

(Reproduced in part with permission from Neidholdt, E.L.; Beauchamp, J.L. *Anal. Chem.* **2007**, *79*, 3945–3948. Copyright 2007 American Chemical Society.)

The construction and implementation of a compact, low power ambient pressure pyroelectric ionization source (APPIS) is presented. The source comprises a z-cut lithium niobate or lithium tantalate crystal with an attached resistive heater mounted in front of the atmospheric pressure inlet of an ion trap mass spectrometer. Positive and negative ion formation alternately results from thermally cycling the crystal over a narrow temperature range. Ionization of 1,1,1,3,3,3-hexafluoroisopropanol or benzoic acid results in the observation of the singly deprotonated species and their clusters in the negative ion mass spectrum. Ionization of triethylamine or triphenylamine with the source results in observation of the corresponding singly protonated species of each in the positive ion mass spectrum. Ion formation appears to result mainly from electrical discharges occurring on the surface of the crystal, and from one z face to another. This dielectric breakdown originates from the high electric fields generated at the surface of pyroelectric crystals when they are thermally cycled by as little as 30 K from ambient temperature. Ion formation is largely unaffected by contamination of the crystal faces. This robust source might prove particularly useful in applications where unattended operation in harsh environments, long service

lifetimes, and durability are desirable characteristics.

2.1 Introduction

The pyroelectric properties of lithium niobate (LiNbO_3) and lithium tantalate (LiTaO_3) make them uniquely useful in certain applications. Since pyroelectric crystals are non-centrosymmetric and possess a maximum of one axis of rotation, a nonzero dipole for each unit cell imparts a net polarization to the bulk crystal. The pyroelectric effect, which is the polarization change of the crystal due to temperature change, leads to an imbalance of charge in the crystal. In a cut crystal the two faces orthogonal to the z crystallographic axis become oppositely charged. This results in a net electrical potential on each z face of the crystal unless it is compensated in some manner.

Present uses of the pyroelectric effect include infrared detectors [1], the production and manipulation of focused and unfocused electron and ion beams under vacuum conditions [2]–[10], x-ray generation and x-ray fluorescence measurements [3], [11]–[15], and possibly the induction of nuclear reactions [16],[17]. Aside from one report of laser desorption of ions from lead lanthanum zirconate titanate (PLZT) [18], pyroelectric materials have not previously been employed as a source of ions for chemical analysis using mass spectrometry. A new application of these materials as the key component in a novel, compact ambient pressure pyroelectric ion source (APPIS) for mass spectrometry is reported.

2.2 Experimental

The source utilizes z cut LiNbO_3 and LiTaO_3 crystals of various dimensions which were purchased from Elan Ltd., St. Petersburg, Russia. The crystals were used as received from Elan, and did not have an electrode attached to any crystal face. Chemical samples were purchased from Aldrich (St. Louis, MO, USA) or Fluka (sold by Aldrich) and used without further purification. Figure 2.1 shows a schematic of the ion source. For the experiments described here, a 5 x 5 x 5 mm pyroelectric LiTaO_3

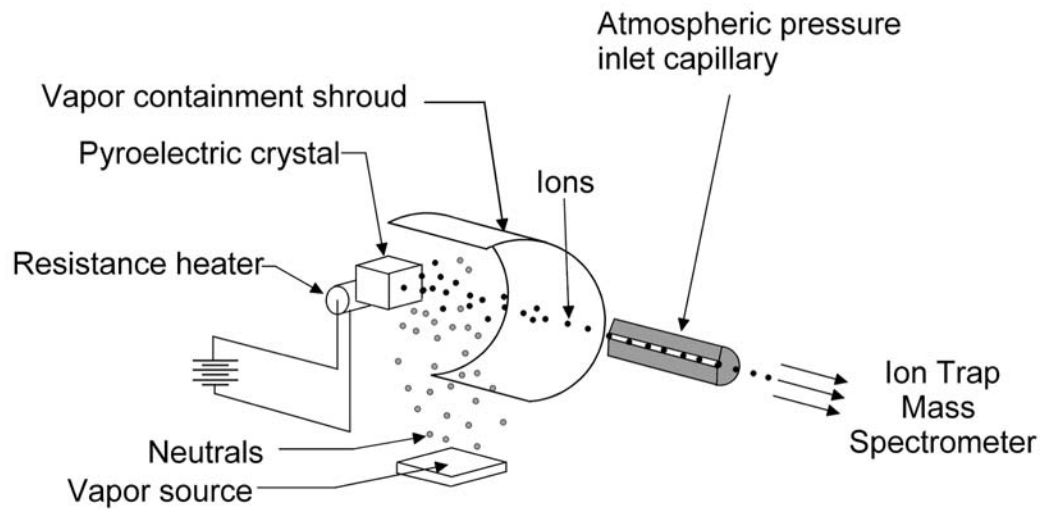


Figure 2.1: Schematic of APPIS source

Ions are produced at the $-z$ face of a pyroelectric crystal and travel through the vapor containment shroud to the atmospheric pressure inlet capillary of the mass spectrometer. The crystal is heated by a resistor cemented to the $+z$ face.

crystal is mounted with the $-z$ face exposed and a resistance heater attached to the $+z$ face. The heater is composed of a 62 ohm, 0.5 watt resistor which was epoxied to the crystal with Arctic Alumina Thermal Adhesive (Arctic Silver Inc, Visalia, CA, USA). Temperature is measured with a copper constantan thermocouple, interfaced with LabVIEW (National Instruments, Austin, TX, USA) by a National Instruments CompactDAQ thermocouple module.

Both cations and anions can be produced from a single face of the crystal, but not detected at the same time. Figure 2.2 illustrates the physical processes that occur on the $+z$ and $-z$ surfaces of a pyroelectric crystal as the temperature is varied. At a fixed temperature the net charge of the crystal face due to polarization is compensated by charged species of the opposite sign that accumulate at the interface [1]. A decrease in temperature leads to an increase in polarization and net deficits of compensating positive charge on the $-z$ face and compensating negative charge on the $+z$ face. As the crystal is heated, the decrease in polarization results in net surpluses of compensating positive charge on the $-z$ face and compensating negative charge on the $+z$ face. Hence, for a crystal whose $-z$ face is exposed, cations will be detected upon heating. While the crystal is cooling, anions will be detected. The source could have just as easily been constructed with the $+z$ face of the crystal exposed.

The source is operated at atmospheric pressure, and employs a shroud made of aluminum to contain sample vapor in the region near the crystal. Sample vapor is introduced into the source through a hole in the containment shroud. The source is mounted in place of the standard electrospray source on a Thermo Finnigan LCQ Deca quadrupole ion trap mass spectrometer, in front of the atmospheric pressure inlet capillary. Except for the ion source replacement, the mass spectrometer was not otherwise modified. The face of the crystal was 7 mm from the capillary inlet. This was determined experimentally to be the optimum distance for maximum signal intensity. The sample holder was fitted with a heater so that solid samples could be sublimed into the source. During all experiments, the atmospheric pressure inlet capillary was held at ground potential, and its temperature was 270 °C. To heat the crystal and sample holder, a pair of Harrison/HP Model 855C DC power supplies

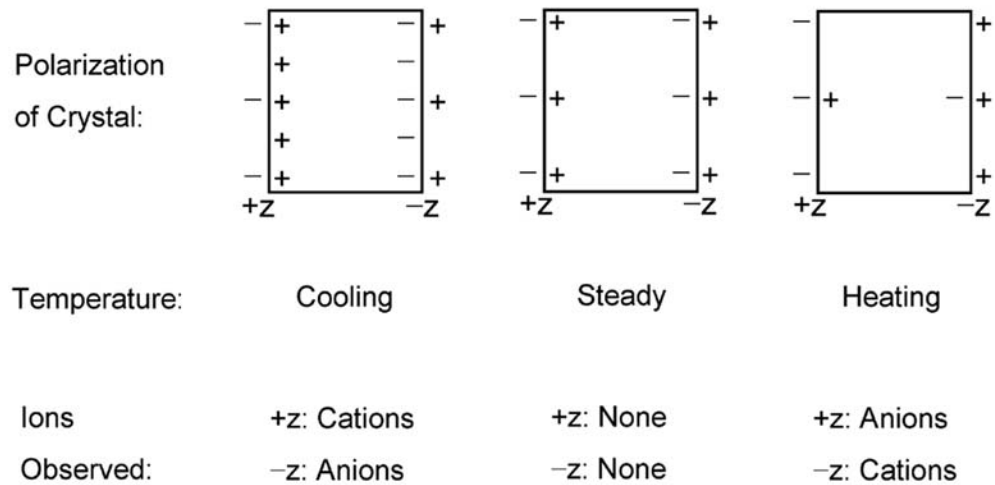


Figure 2.2: Charging of crystal faces on temperature change

At a fixed temperature, the net charge of the crystal face due to polarization is compensated by charge species of the opposite sign that accumulate at the interface. A decrease in temperature leads to an increase in polarization and a net surplus of negative compensating charges on the $-z$ face and positive compensating charges on the $+z$ face. As the crystal is heated, the decrease in polarization results in a net surplus of positive compensating charges on the $-z$ face and negative compensating charges on the $+z$ face.

passed current through the corresponding heating resistors. The supplies are remotely programmed using LabVIEW, facilitating recording of the temporal variation of ion yield as the temperature was cycled.

2.3 Results and Discussion

Figure 2.3a and Figure 2.3b are the negative ion mass spectrum of 1,1,1,3,3,3-hexafluoro-2-propanol and the temporal variation of ion abundance (total ion current) as the crystal temperature decreases, respectively. Abundant ions in the mass spectrum include the deprotonated alcohol, at 167.0 m/z, and the proton bound dimer of the deprotonated alcohol, at 334.9 m/z. Figure 2.4a and Figure 2.4b show similar data for the the negative ion mass spectrum of benzoic acid. The deprotonated acid appears in the mass spectrum at 121.1 m/z. Figure 2.5a and Figure 2.5b are the positive ion mass spectrum of triethylamine and the temporal variation of ion abundance as the crystal temperature is increased, respectively. The abundant ion in the mass spectrum is the protonated tertiary amine, at 102.2 m/z. Figures 2.6a and b show similar data for the positive ion mass spectrum of triphenylamine. The protonated tertiary amine appears in the mass spectrum at 246.2 m/z.

$$C = \frac{\epsilon_{cr}A}{d_{cr}} \quad (2.1)$$

Ion formation appears to result mainly from electrical discharge occurring between the two faces of the crystal. Large electrical potentials build up on the surfaces of the crystal as the temperature is cycled. If the pyroelectric crystal is thought of as a parallel plate capacitor, with the two crystal faces as plates and the dielectric being the metal oxide crystal material, the capacitance for the crystal is given as in Equation 2.1 where ϵ_{cr} is the dielectric constant for the crystal material, A is the area of the crystal z-face, and d_{cr} is the crystal thickness. The units of capacitance, Farads, are expressed as coulomb per volt, or charge per unit electrical potential as in Equation 2.2. The expression can be arranged to express voltage in terms of charge

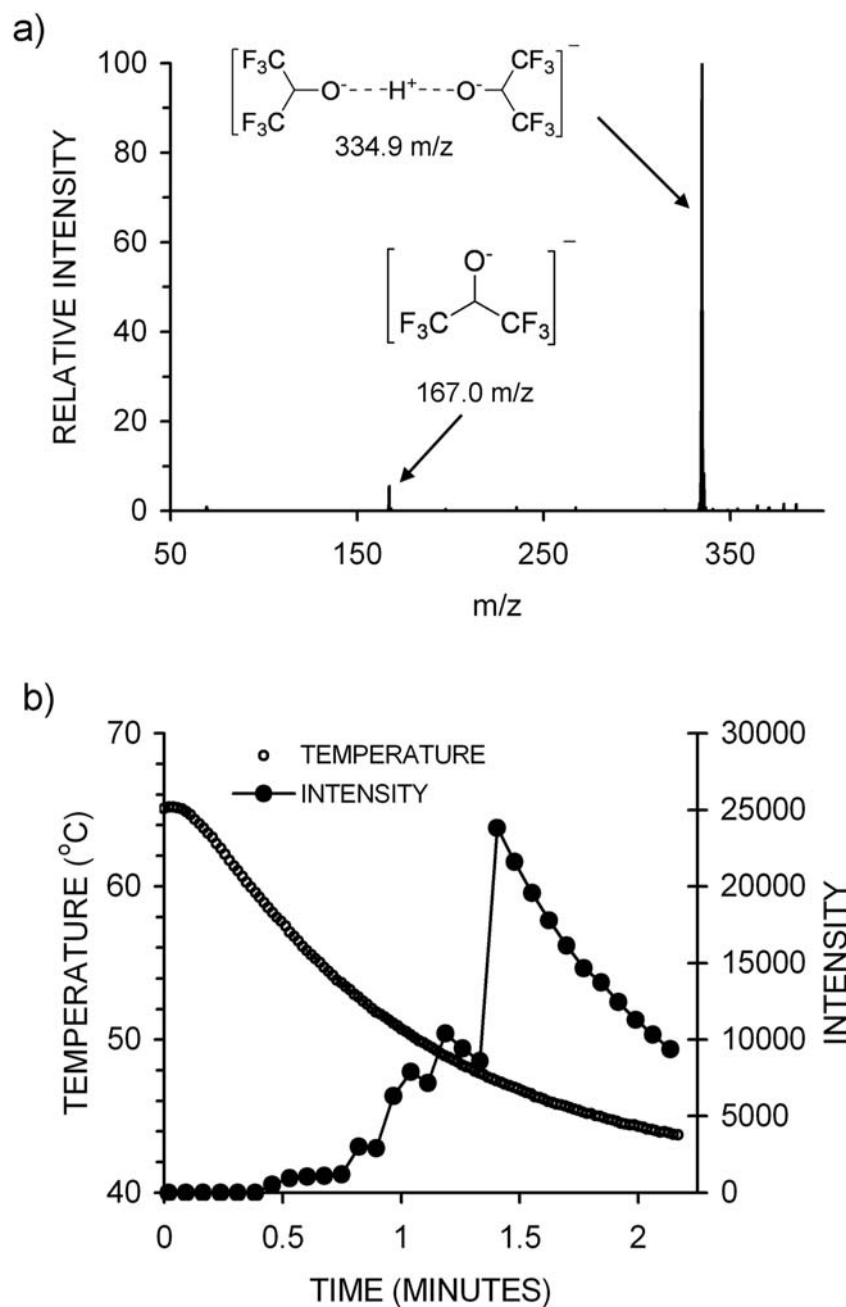


Figure 2.3: Negative ion mass spectrum of 1,1,1,3,3,3-hexafluoroisopropanol and temporal variation of total ion yield as the crystal is cooled

a) Seen in the mass spectrum is the deprotonated alcohol and the proton bound dimer of the alcohol. b) The abrupt changes in ion yield likely result from the occurrence of sporadic discharges as the crystal temperature is varied.

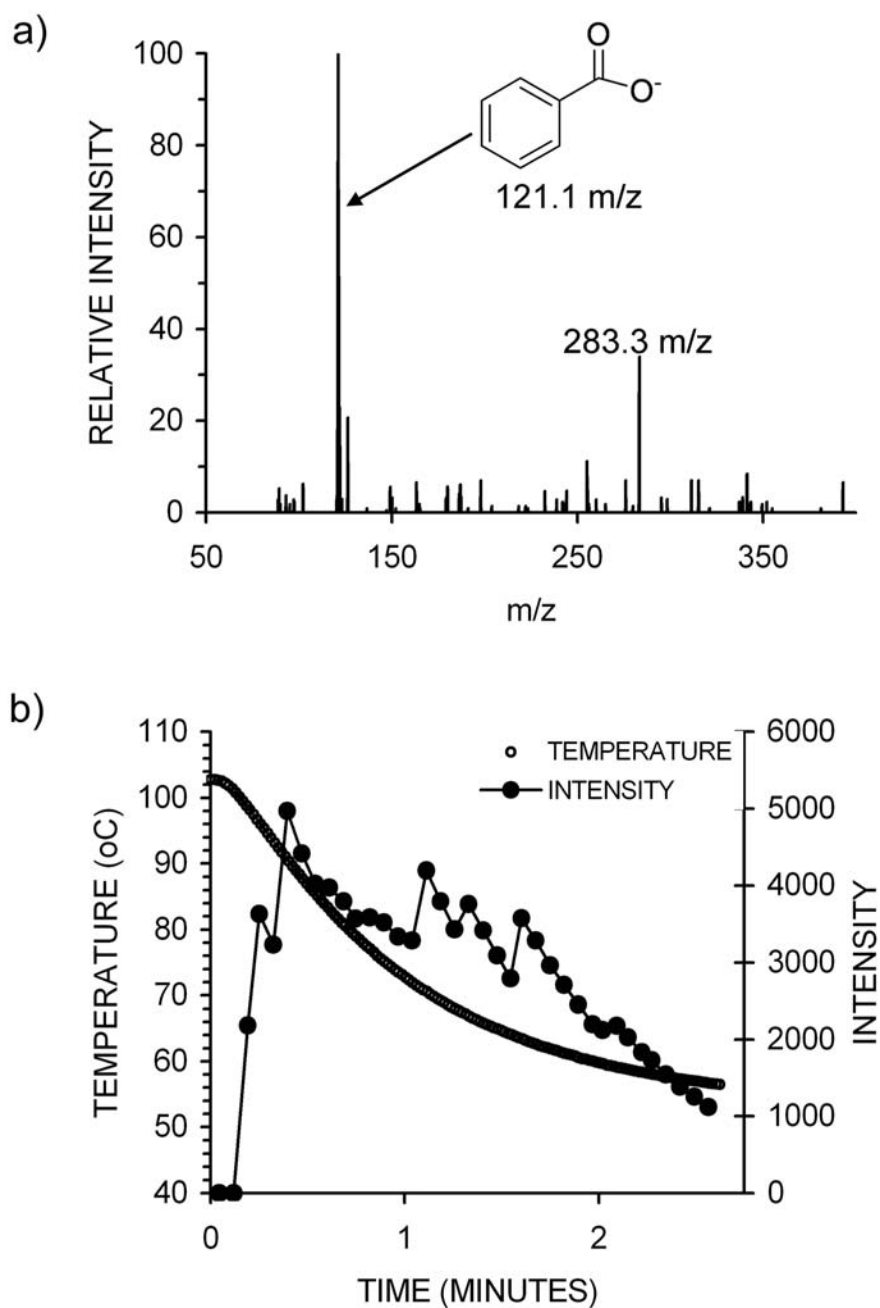


Figure 2.4: Negative ion mass spectrum of sublimed benzoic acid and temporal variation of total ion yield as the crystal is cooled

a) The deprotonated acid is observed in the mass spectrum. The peak at 283.3 m/z has not been identified. b) Sporadic ion production is again observed on cooling of the crystal, again likely due to the occurrence of electrical discharges as the crystal is cooled.

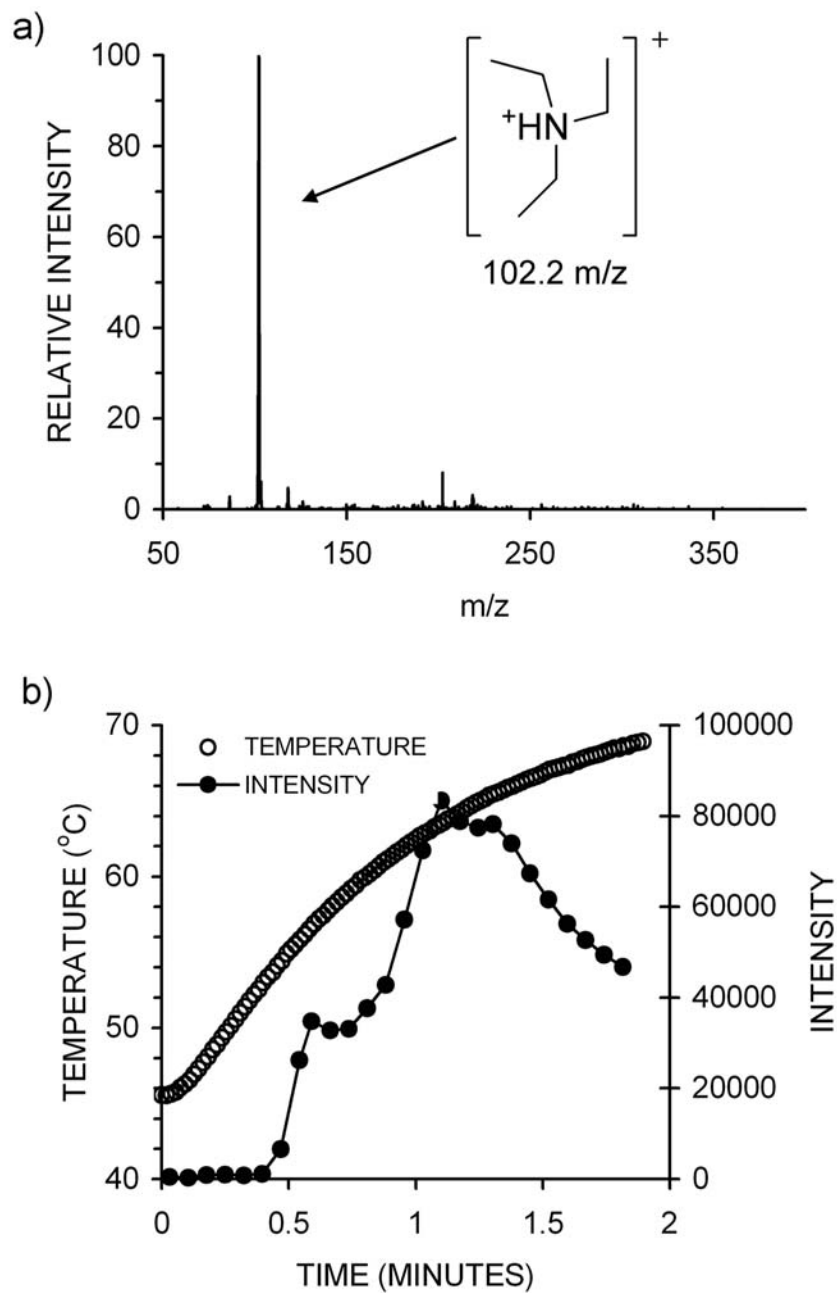


Figure 2.5: Positive ion mass spectrum of triethylamine and temporal variation of ion yield as the crystal is heated

a) The protonated amine is observed as the base peak in the mass spectrum. b) Temporal variation of ion yield as the crystal is heated.

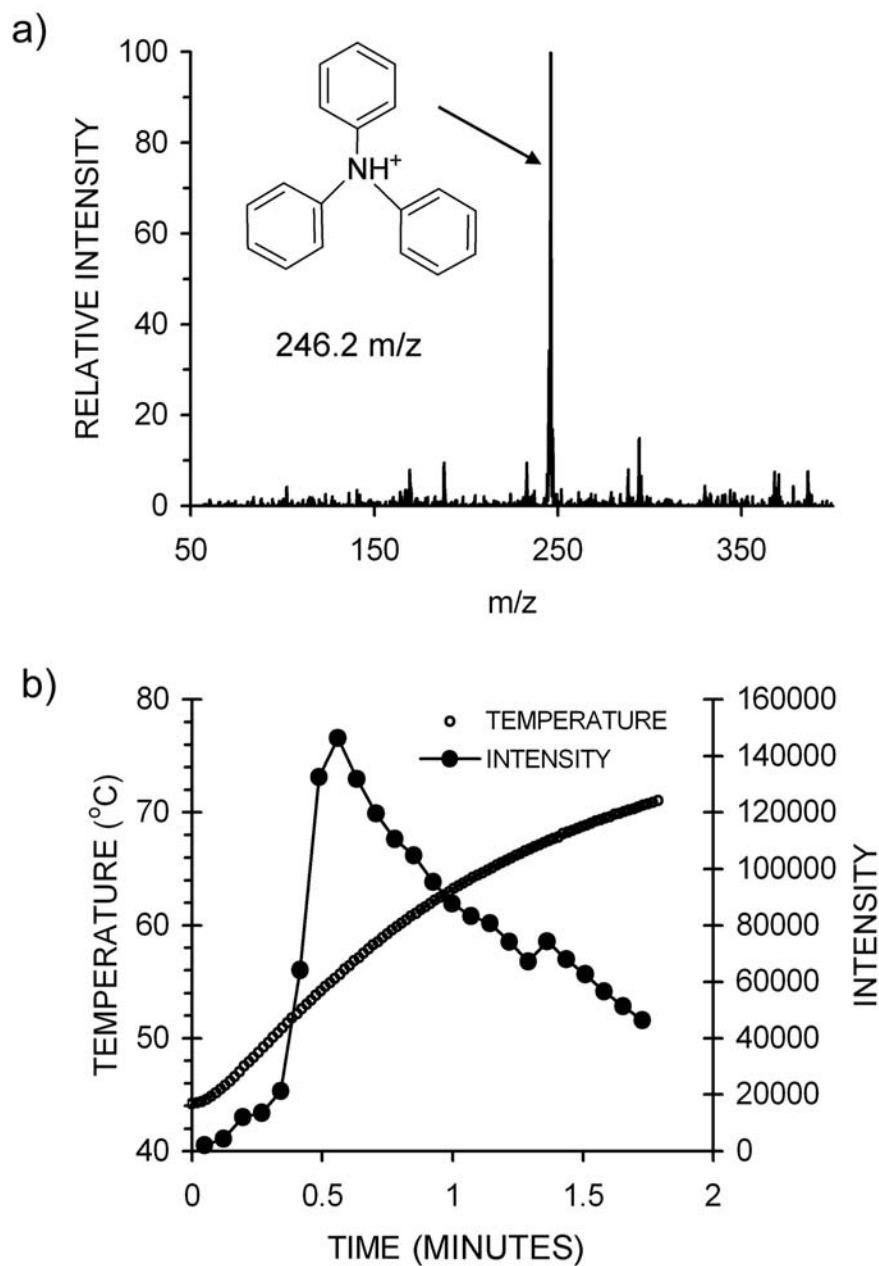


Figure 2.6: Positive ion mass spectrum of triphenylamine and temporal variation of ion yield as the crystal is heated

a) Positive ion mass spectrum of sublimed triphenylamine, showing the protonated amine. b) Temporal variation of ion yield as the crystal is heated. Ion production is again sporadic.

and capacitance.

$$C = \frac{Q}{V}, V = \frac{Q}{C} \quad (2.2)$$

If the expressions for capacitance of the pyroelectric crystal are included with Equation 2.2, the magnitude of the voltage on any plate of the crystal capacitor (crystal face) can be calculated using Equation 2.3.

$$V = \frac{Qd_{cr}}{\epsilon_{cr}A} \quad (2.3)$$

For a pyroelectric crystal, the charge build-up per unit area can be calculated by multiplying the material's pyroelectric coefficient, γ , by the temperature change in the experiment, as in Equation 2.4.

$$\frac{Q}{A} = \gamma\Delta T \quad (2.4)$$

Combining Equation 2.3 and Equation 2.4, the change in potential on the face of the crystal in response to a change in temperature ΔT is given by Equation 2.5.

$$V = \frac{d_{cr}\gamma\Delta T}{\epsilon_{cr}} \quad (2.5)$$

In Equation 2.5 γ is the pyroelectric coefficient, d_{cr} is the thickness of the crystal, and ϵ_{cr} is the dielectric constant of the crystal along the z axis ($\epsilon_{cr} = 46\epsilon_0$ for LiTaO₃, $\epsilon_{cr} = 30 \epsilon_0$ for LiNbO₃). For LiNbO₃, $\gamma = 70 \mu\text{C}/(\text{m}^2\text{K})$ and LiTaO₃, $\gamma = 190 \mu\text{C}/(\text{m}^2\text{K})$ [19]. For a lithium tantalate crystal with thickness $d_{cr} = 5 \text{ mm}$ subjected to a temperature change of 30 K, the potential of the crystal face could reach $7.0 \times 10^4 \text{ V}$ if no discharging occurred. The crystal face potentials can thus increase beyond the point of dielectric breakdown in air, causing a discharge to occur between the two z faces of the crystal. These discharges can be observed with the naked eye in a perfectly dark room; they can also be heard in a quiet room. Although the faces are discharged after a spark, continued temperature change begins the charge buildup process anew, leading to additional discharge. A discharge would produce

both positive and negative ions simultaneously, yet only one ion polarity is seen at a time. The polarity of ions seen in the mass spectrometer can be attributed to the sign of the charge on the crystal face facing the atmospheric pressure inlet at a particular moment. For example, a negatively charged crystal face will scavenge cations so that they are not detected by the mass spectrometer, while directing anions towards the capillary inlet.

2.4 Conclusion

A novel ion source for ambient mass spectrometry which utilizes the pyroelectric properties of lithium tantalate for the production of electrical discharges upon temperature cycling of the material is presented. The source is extremely durable; no particular care was taken to protect the surface of the crystal from scratches or contamination while being used. It was touched frequently by bare fingers, leaving visible fingerprints on the crystal surface, with no degradation in performance. As a more extreme test of durability, a 1–2 mm thick layer of Dow Corning silicone vacuum grease was applied to all exposed surfaces of the crystal. Electrical discharges and ion production were observed with the crystal in this state. The mass spectra collected with this coating present were no different than those obtained with a clean crystal. The source might prove particularly useful in applications where unattended operation in harsh environments, long service lifetimes, and durability are desirable characteristics. Such applications might include instrumentation for detection of organic molecules in space environments, the detection of CBW agents in battlefield situations, and the monitoring of volatiles from industrial accidents or chemical spills by first responders or hazardous materials cleanup teams.

Chapter 3

Ionization Mechanism of the Ambient Pressure Pyroelectric Ion Source (APPIS) and Its Applications to Chemical Nerve Agent Detection

(Reproduced in part with permission from Neidholdt, E.L.; Beauchamp, J.L. *J. Am. Soc. Mass Spectrom.* **2009**, *20*, 2093–2099. Copyright 2009 American Society for Mass Spectrometry.)

Studies of the ionization mechanism operative in the ambient pressure pyroelectric ionization source (APPIS), along with applications that include detection of simulants for chemical nerve agents are presented. It is found that ionization by APPIS occurs in the gas phase. As the crystal is thermally cycled over a narrow temperature range, electrical discharges near the surface of the crystal produce energetic species which, through reactions with atmospheric molecules, result in reactant ions such as protonated water clusters or clusters of hydroxide and water. These go on to react with trace neutrals via proton transfer reactions to produce the ions observed in mass spectra, which are usually singly protonated or deprotonated species. Further implicating gas phase ionization, observed product distributions are highly dependent on the composition of ambient gases, especially the concentration of water vapor and oxygen surrounding the source. For example, basic species such as triethylamine are

observed as singly protonated cations at a water partial pressure of 10 Torr. At a water pressure of 4 Torr, reactive oxygen species are formed and lead to observation of protonated amine oxides. The ability of the APPIS source to detect basic molecules with high proton affinities makes it highly suited for the detection of chemical nerve agents. This application is demonstrated using simulants corresponding to VX and GA (Tabun). With the present source configuration, pyridine is detected readily at a concentration of 4 ppm, indicating ultimate sensitivity is likely in the high ppb range.

3.1 Introduction

The design and implementation of a novel ambient pressure pyroelectric ion source (APPIS) for mass spectrometry was presented previously. The source comprises a thermally cycled pyroelectric crystal (lithium niobate or lithium tantalate) coupled with a neutral vapor source in front of the atmospheric pressure inlet of an ion trap mass spectrometer. Ions are produced at or near the crystal surface during periods of thermal cycling, and positive and negative ions are alternately produced upon heating and cooling, respectively, at the $-z$ face. Fragment ions are typically not observed in the mass spectrum, revealing that APPIS ionization is a “soft” ionization method. Acidic and basic species are typically observed as the corresponding deprotonated and protonated molecular ions, respectively.

Electrical discharges are observed at the faces of the crystal during thermal cycling, and we suggested that they may contribute to the detected ion signal. Ion sources using some form of electrical discharge are numerous and well-known, including various forms of glow discharge ionization [21]–[23] and corona discharge ionization [24]. Dielectric barrier discharge ionization [25] creates an AC discharge between a needle and a thin dielectric layer, under which lies an electrode which completes the discharge circuit, and ions can be desorbed from this dielectric layer and sampled by mass spectrometry. Since discharges may play an important part in APPIS ionization, we present here an investigation into the nature of the observed discharges and their relationship to ion production. A mechanism of ionization involving a form of

atmospheric pressure chemical ionization is proposed, whereby molecules which are detected as protonated species have undergone reaction with reactant ions present in humid air of the form $^+H(H_2O)_n$ or $^-OH(H_2O)_n$.

In addition to studies of the ionization mechanism, the utility of the source for the detection of simulants for chemical nerve agents is investigated. It was seen previously that volatile organic molecules with basic functional groups were detected as protonated species using APPIS mass spectrometry. Numerous chemical nerve agents contain basic functional groups and are likely well suited to detection by APPIS mass spectrometry. Previous investigations which have reported the detection of chemical nerve agents by ion mobility and mass spectrometry [26]–[28] use compounds similar in reactivity to the nerve agents, termed simulants. Diethyl phosphoramidate (DEPA) simulates Tabun (GA), and 2-(butylamino)ethanethiol simulates VX. We demonstrate the detection of these nerve agent simulants using APPIS and ion trap mass spectrometry. Lastly, a sensitivity study was performed using pyridine and it was found that pyridine is readily detectable down to concentrations of 4 parts per million, suggesting ultimate sensitivity of the current source implementation in the high part per billion range.

3.2 Experimental

Figure 3.1a shows a schematic of APPIS, which is installed in front of the atmospheric pressure inlet of an ion trap mass spectrometer (ThermoFinnigan LCQ Deca). For the experiments described here, a 5 x 5 x 5 mm pyroelectric LiTaO₃ crystal (Elan Ltd, St. Petersburg, Russia) is mounted with the $-z$ face exposed and a resistance heater attached to the $+z$ face. The heater comprises a 62 ohm, 0.5 watt resistor epoxied to the crystal with Arctic Alumina Thermal Adhesive (Arctic Silver Inc, Visalia, CA, USA). Temperature is measured with a copper constantan thermocouple, interfaced with LabVIEW (National Instruments, Austin, TX,) by a National Instruments CompactDAQ thermocouple module. The proposed ionization mechanism, discussed in further detail below, is depicted in Figure 3.1b and involves electrical discharges at

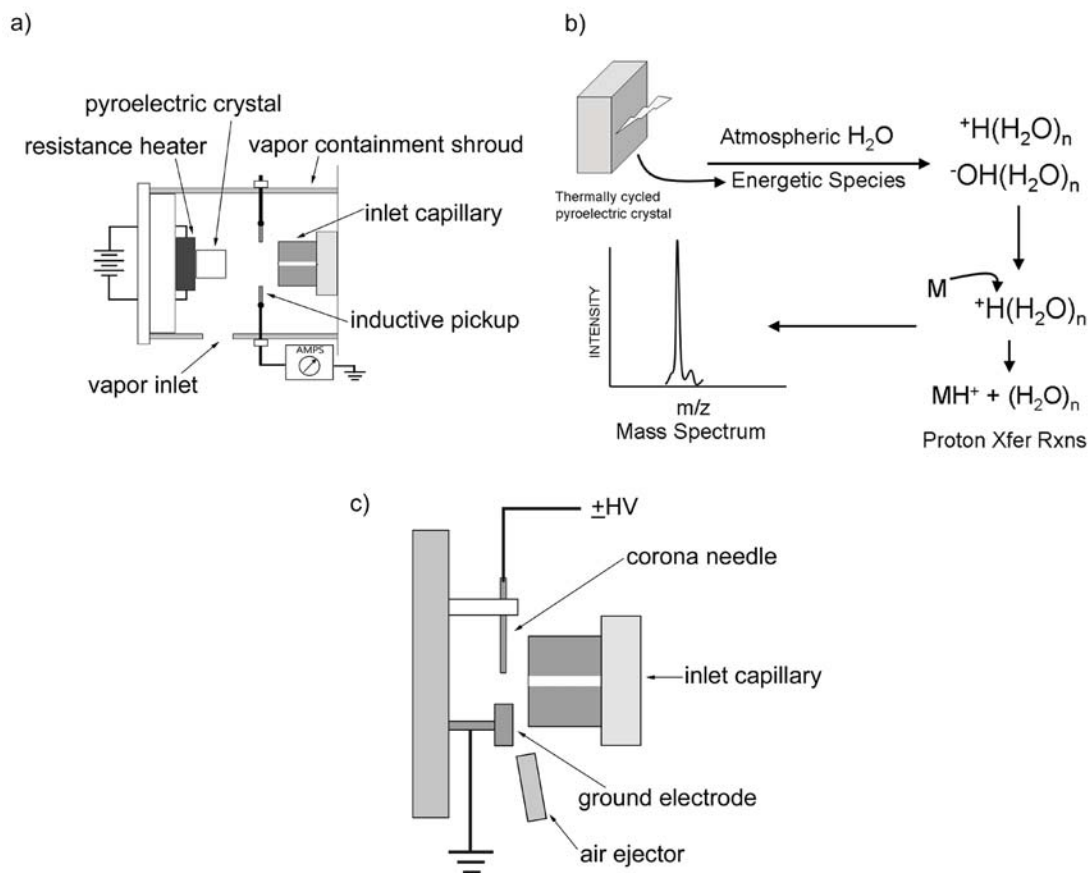


Figure 3.1: Generation Two APPIS apparatus

a) Schematic of APPIS source (to scale). Ions are produced at the $-z$ face of a pyroelectric crystal and travel through the vapor containment shroud to the atmospheric pressure inlet capillary of the mass spectrometer. The crystal is heated by a resistor cemented to the $+z$ face. An inductive pickup is placed so that induction current (That is, the flow of charge induced on the crystal face) can be monitored. b) Proposed ionization mechanism for APPIS. Electrical discharge on the crystal surface leads to the production of energetic species, which combine and react with atmospheric water clusters or clusters of hydroxide anion and water. These reactant ions take part in proton transfer reactions with basic and acidic species, leading to ionization of the analytes and observation of them in the mass spectrometer. c) Schematic of the corona discharge source. High voltage is applied to the needle and corona discharge occurs between the needle and ground electrode. Sample is introduced via pneumatic air ejector.

the crystal face. To monitor electrical activity on the crystal face the source was additionally fitted with an inductive pickup. The pickup comprises a stainless steel ring, to which an electrical connection was made, suspended inside the vapor containment shroud by support wires, 4 mm from and centered with the -z crystal face. The pickup is electrically insulated from the shroud and connected through a current measuring device to ground. Either a Keithley 485 autoranging picoammeter having a measured time constant of $\tau=2$ ms or an operational amplifier having a gain of 10^7 V/A and measured time constant of $\tau=100\mu\text{s}$ was used for current measurement. The picoammeter afforded better sensitivity to lower current levels, at the cost of an increased circuit response time. The operational amplifier, although less sensitive, allowed for better resolution of temporal features in the measured induction current. Induction current is the flow of charge induced on the pickup by the charged crystal face, detected as a current in the external circuit. The sign of the current measured is the same as the charge developed on the crystal face when current is defined as the flow of positive charge. The voltage outputs of the picoammeter and op-amp were monitored and recorded using LabVIEW with an NI9205 CompactDAQ input module (National Instruments, Austin, TX).

Figure 3.1c is a schematic of an atmospheric pressure chemical ionization (APCI) source which was constructed to compare ionization by this method to APPIS ionization. The APCI source comprised a direct current (DC) corona discharge in air placed in close proximity to the atmospheric pressure inlet of a ThermoFinnigan LCQ Deca ion trap mass spectrometer. An inlet capillary extension was added to the instrument in this case, so that the corona could be easily placed within 5 mm of the ion sampling inlet. A tungsten inert gas welding electrode, ground to a point, was used with a gap distance of 1–2 mm between the electrode point and ground. A starting potential of between 1500–3000 V was applied to the needle, which was connected to the high voltage power supply through a 10 M Ω , 1W current limiting resistor. Samples for APCI analysis were introduced into the corona using a fabricated pneumatic air ejector. To operate the ejector, compressed air expands from a small orifice which causes a reduced pressure region near the sample inlet, causing sample to be mixed

with air. The air/sample mixture is exhausted into the corona, and the ions produced are sampled through the atmospheric inlet capillary of the mass spectrometer.

Samples for determination of detection limits were prepared by on-line dilution using a Model 1010 gas diluter (Custom Sensor Solutions, Oro Valley, AZ, USA). Samples of pyridine were prepared by injecting 10–25 μL liquid pyridine into a 40 L capacity Tedlar sample bag, which was then filled with 40 L of dry nitrogen. 200 μL water was additionally injected into the bag to set a water partial pressure of approximately 6 torr (800 Pa), emulating atmospheric conditions. The sample bag was then connected to the sample input of the gas diluter, whose output was then connected to the gas inlet port of the APPIS source. Dilutions were performed with a diluent bag also containing nitrogen and water. The gas diluter has usable dilution settings from 2% to 100%, meaning available concentration ranged from 2 to 100 percent of the prepared concentration. Triethylamine and pyridine were from Fisher Scientific. Hexafluorobenzene and 1,1,1,3,3,3-hexafluoroisopropanol were from Fluka (sold by Sigma-Aldrich, St. Louis, MO). 2-(butylamino)ethanethiol, diethylphosphoramidate, and benzoic acid were from Sigma-Aldrich. All chemicals were used as received, without further purification.

3.3 Results and Discussion

Ions are observed in coincidence with electrical activity as detected by the inductive pickup. Figure 3.2a exhibits the temporal variation of induction current and total ion current as detected by the mass spectrometer during an experiment where the crystal is being heated, producing cations from triethylamine in air. In the present implementation, ion production appears to be strongly correlated with the more frequent, lower current discharges. Figure 3.2b illustrates the variation with time of induction current and total ion current for an experiment where anions from 1,1,1,3,3,3-hexafluoroisopropanol are detected. The crystal was first heated to a temperature near 80 degrees C (region not shown, from $t=0$ to $t=2$ min) and allowed to cool ($t=2$ to $t=6$ min, shown). In the anionic experiments there are many more of the higher

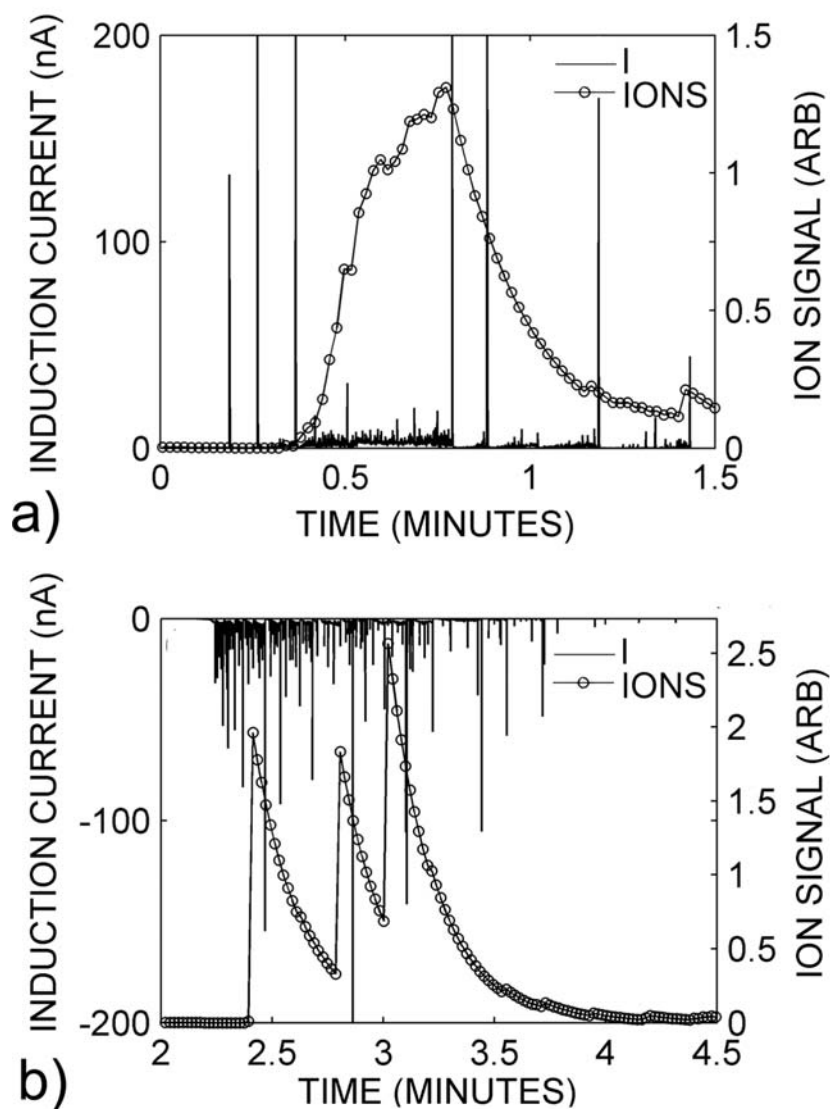


Figure 3.2: Temporal variation of induction current and ion signal for cations and anions

a) Temporal variation of ion signal and induction current for positive ion formation from triethylamine. The crystal was heated at a rate of approximately 0.5 K s^{-1} , from $t=0$ to $t=1.5$ min. The frequency of spark discharges is low relative to the lower intensity dark discharging, and most ions are produced during periods of dark discharging. b) Temporal variation of ion signal and induction current for negative ions from hexafluoroisopropanol. The crystal was first heated to a temperature of approximately 80 degrees C, and then allowed to cool at a rate of 0.5 K s^{-1} . As further discussed in this text, the frequency of sparking is high compared with that observed when the crystal is heated. Ion production occurs during the periods of electrical activity.

current discharges occurring during the time of ion production. This is likely due to the presence of electrons at the crystal surface, a consequence of the pyroelectric effect [14]. These electrons ‘prime’ the air with excess charge so that dielectric breakdown occurs more easily than in the case of a positively charged crystal. The discharges in each case correspond to a buildup of charge up to the point of dielectric breakdown, followed by a rapid flow of this charge to a region nearer to ground potential, either the opposite crystal face, a part of the metal mount near the crystal, or another region on the crystal face. Electrical discharges at the crystal face leading to ionization of analyte suggest a gas phase ionization mechanism. An APCI source was constructed to compare the results of ionization by stand-alone APCI with those of APPIS.

The APCI mass spectra of test compounds were essentially identical to the APPIS mass spectra of the same compounds when acquired under similar environmental conditions. Differences observed in the APCI and APPIS mass spectra can be accounted for by considering differences in gas composition associated with each experiment. APCI experiments were performed by injecting the sample into the corona using compressed air, which contains very little water vapor due to the fact that it is dried during production so as not to condense water vapor during the compression process. Any pneumatically assisted APCI experiments using the corona discharge source will take place in relatively dry air. Owing to the ambient pressure characteristics and projected future use of the source, APPIS experiments are typically performed by analyzing the sample vapor in an environment of ordinary laboratory air which is on average between 40 and 60 percent relative humidity, as determined by dew point measurements. This corresponds to a partial pressure of water in air of about 10 torr (1.3×10^3 Pa). Under the typical conditions for each experiment (dry air for APCI, humid air for APPIS), the mass spectra for triethylamine show distinctly different product yields.

APPIS mass spectra of triethylamine on typical day ($p(\text{H}_2\text{O}) = 10$ torr, 1.3×10^3 Pa) yield the protonated molecular ion as the base peak in the spectrum and a small percentage of what we assign as the protonated n-oxide of triethylamine. Figure 3.3a shows this result. When neat vapor is analyzed using the APCI source when lab air is

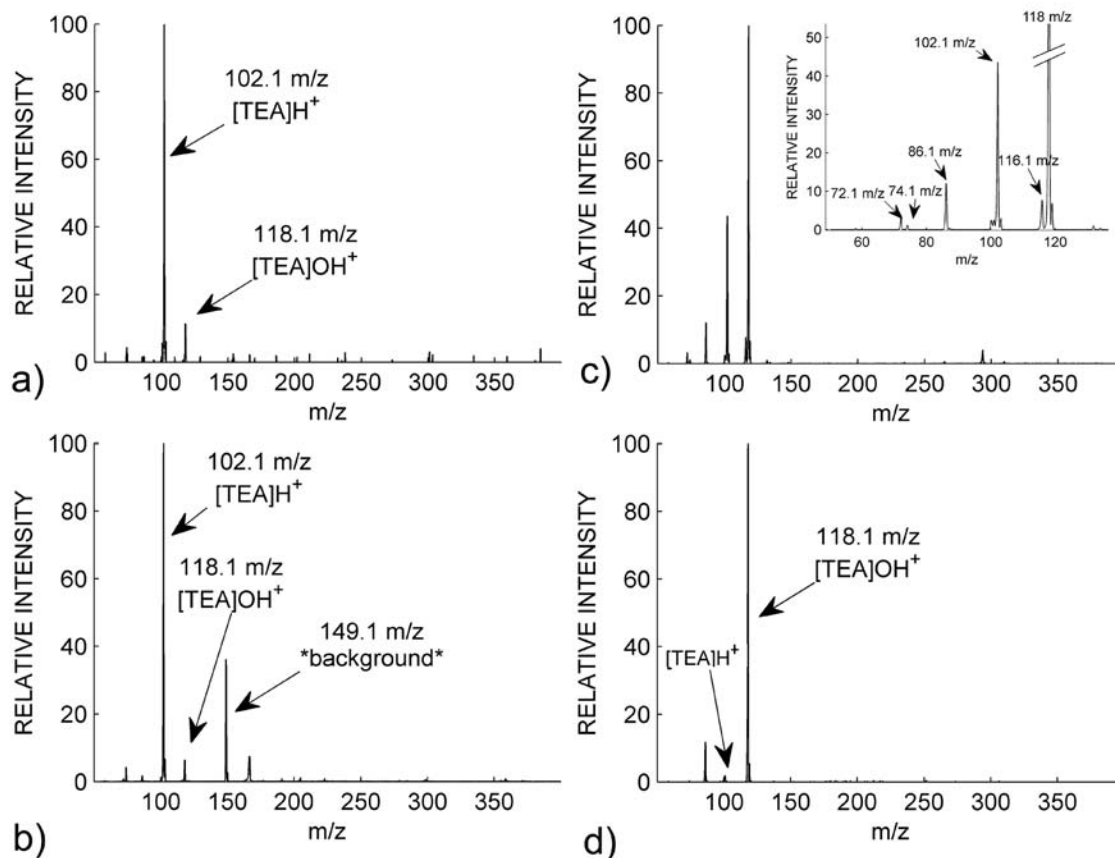


Figure 3.3: Comparison of signal resultant from APPIS and APCI under different sampling conditions

a) APPIS mass spectrum of triethylamine with ambient air at approx. 40–50% relative humidity. This is a typical APPIS spectrum in that it is consistent with previously measured spectra, and is free from sample oxidation artifacts. b) APCI mass spectrum of triethylamine where neat vapor is allowed near the corona discharge in ambient air of moderate humidity. Note the close match to a), indicating that in APCI the humidity of the air near the corona is important in determining the ionization products. The peak at 149.1 m/z appears without sample vapor present as well, implicating it as an unknown background contaminant in lab air. c) APCI mass spectrum of triethylamine using pneumatic air ejector for sample injection. Air is relatively dry around the corona due to use of compressed air as a carrier gas. d) APPIS mass spectrum of triethylamine with ambient air at approximately 20% relative humidity, as determined by dew point and wet bulb thermometer measurements. Air is dry near the crystal.

of 50 to 60% relative humidity, the spectra match the ‘average’ APPIS mass spectra (Figure 3.3b). An APCI mass spectrum of triethylamine using dry, compressed air (Figure 3.3c) yields triethylamine n-oxide as the most abundant ion with a significant percentage of protonated triethylamine. The formation of triethylamine n-oxide is likely a consequence of the redox conditions present during discharge, and others have observed similar addition of oxygen to triethylamine under oxidative conditions [29],[30]. Minor products observed (m/z 72.1, 74.1) are decomposition products of triethylamine n-oxide and are unique to that compound. These follow reactivity outlined by Ma and coworkers [31] of thermally induced decomposition of TEA-O during APCI. One additional minor product in the spectrum (116.0 m/z) is identified via a reaction pathway analogous to that summarized by Atkinson [32], whereby triethylamine reacts with hydroxyl radical and through subsequent carbon and oxygen centered radical intermediates the species $\text{CH}_3\text{CON}(\text{C}_2\text{H}_5)_2$, or N,N-diethylacetamide is formed. Having a molecular weight of 115 Da, the protonated N,N-diethylacetamide is observed at 116.0 m/z . These oxidation products are formed along with the protonated species during ionization. Relative humidity of the air around the source region will determine the concentrations of reagent ions and thus the ratio of ionization products. We observe that with moderately humid conditions, the product from direct protonation is more likely to be observed than the oxidation products. The water clusters are dominant with high humidity, whereas the oxidative reagents play a prominent role with low humidity. On days when relative humidity in the lab is low (20 to 30% relative humidity) the APPIS mass spectra in lab air nearly match the APCI mass spectra using dry compressed air (Figure 3.3d). This modulation of product distributions by ambient gas composition not only indicates that ionization by APPIS involves gas phase processes, similar to APCI, but also that this source parameter, relative humidity of the gas surrounding the source, must be considered in interpreting source response.

An ionization mechanism is suggested involving observed electrical discharges near the face of the crystal resulting in reagent ions which take part in chemical ionization reactions with analytes to result in the observed ionization products. Figure 3.1b

is a cartoon illustrating the proposed sequence of events leading to observation of an ion in the mass spectrometer. An excess of electrical charge is developed on the crystal face as a result of temperature cycling, and this charge is neutralized through electrical discharges either to the opposite crystal face, a region on the face of lesser charge due to uneven heating of the sample or crystal defects that lead to non-uniform charging of the surface, or a nearby grounded electrode. The transient signals from these discharges are measured using the inductive pickup fitted to the ionization source. Highly reactive and short lived products resulting from the discharge react with molecules in ambient air to form the reagent precursor ions which are directly observed in the ion trap mass spectrometer.

In addition to investigating the mechanism of ionization of APPIS, the range of substances which are ionizable with the pyroelectric ion source, as well as the performance characteristics of the source are investigated. APPIS is a particularly simple and robust ion source which lends itself to application in harsh environments. One important application of an ion source with these characteristics is the detection of chemical warfare agents. Simulants for chemical nerve agents in the V and G classes have been examined since they possess amine functionality, which has been shown to be advantageous for ionization using APPIS. Due to risks posed in working directly with these agents, compounds which simulate the reactivity of these agents are instead used. Hill and coworkers have used a number of these simulants in ion mobility experiments [26]–[28]. 2-(butylamino)-ethanethiol (BAET), which simulates the nerve agent VX, and diethylphosphoramidate (DEPA), which simulates Tabun, were tested in the laboratory using APPIS. Table 3.1 summarizes the ability of APPIS to ionize these compounds, which were detected as protonated molecular ions using the ion trap mass spectrometer (Figure 3.4). Although the simulant for Tabun has no amine functionality, the protonated phosphodiester was nonetheless detected. In this experiment the sample container was heated to produce significant vapor pressure of the simulants. The APPIS mass spectra for these compounds match the positive ion electrospray mass spectra. For BAET, a significant quantity of dimeric BAET was detected in both APPIS and electrospray mass spectra. This may result from

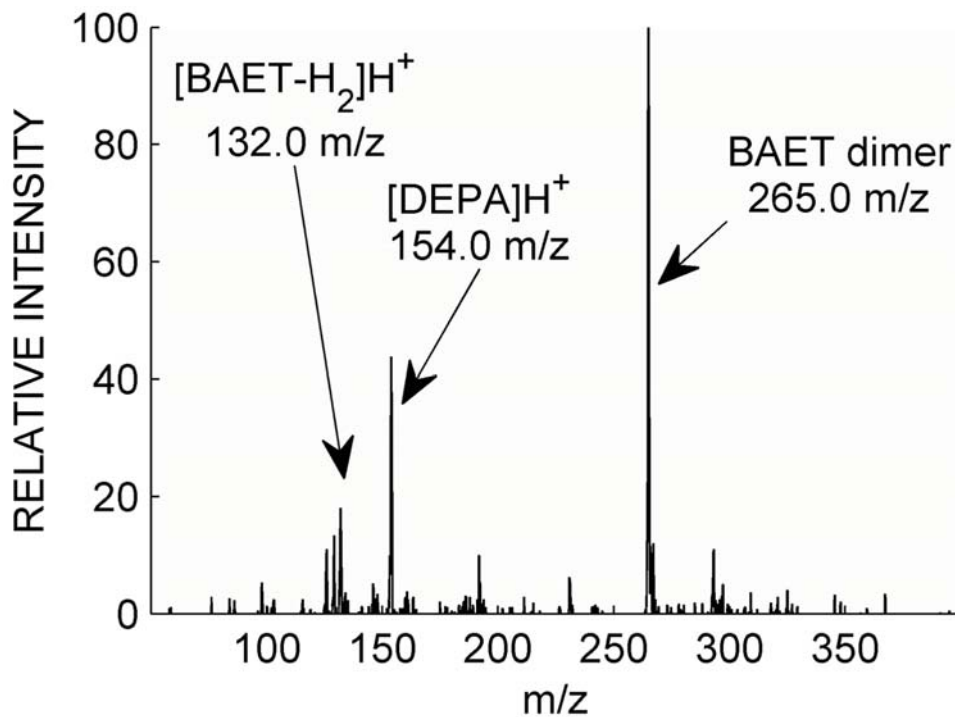


Figure 3.4: Mass spectrum of BAET (simulant for VX) and DEPA (simulant for Tabun)

Mass spectrum showing the detection of chemical nerve agent simulants with AP-PIS. The infused sample was 2-(butylamino)ethanethiol (BAET, simulant for VX, a member of the V agent class) and diethyl phosphoramidate (DEPA, simulant for Tabun, member of the G agent class). The protonated species are observed in the spectrum, with minimal fragmentation, allowing for the detection of signature masses of the stimulants which were detected either as singly protonated species or dimeric complexes in APPIS mass spectra. Table 3.1 lists specific identities for each peak.

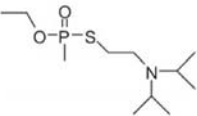
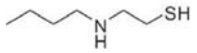
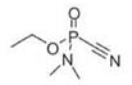
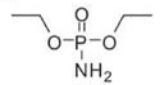
Agent	Simulant	Product ions	Assignment
 VX	 2-(Butylamino)-ethanethiol (BAET) MW 133.1	132.0 <i>m/z</i> 134.0 <i>m/z</i> 265.0 <i>m/z</i>	[BAET-H ₂]H ⁺ [BAET]H ⁺ [BAET-H ₂]-H ⁺ -[BAET]
 Tabun (GA)	 Diethylphosphoramidate (DEPA) MW 153.1	154.0 <i>m/z</i>	[DEPA]H ⁺

Table 3.1: Summary for the detection of CBW agent simulants by APPIS

high simulant concentrations and appropriate redox conditions at the time of ionization. Collision induced dissociation (CID) experiments verify the assignments given in Table 3.1.

Sample dilution experiments were performed to determine the performance and detection limits for APPIS. Pyridine was chosen as a test compound for performance evaluation. Samples of pyridine vapor were prepared in Tedlar sample bags and analyzed using APPIS. Figure 3.5 shows the detection of pyridine at a concentration of 4 ppm in nitrogen. Water was added to the sample bag as the reagent molecule, and is the proton source in this experiment. Detection of pyridine at a concentration of 4 ppm with a signal-to-noise ratio of approximately 10 indicates that the ultimate sensitivity of APPIS for this compound, in the current source configuration, is likely in the high part-per-billion (ppb) range.

3.4 Conclusion

Studies of the ionization mechanism operative with APPIS reveal that ion formation involves a gas phase process, occurring concurrently with electrical discharge activity on the surface of the crystal as it is thermally cycled. For both positive and negative ions, reactions occurring between gases surrounding the ionization source and the analyte molecules are responsible for ion production. Ionization with APPIS is sensitive to environmental factors, specifically the ambient concentration of water vapor at the time of spectrum acquisition. Low relative humidity (20% to 40 %, $p(\text{H}_2\text{O})=4$ torr or 530 Pa) yields ionization products that include target molecules oxidized by reactive oxygen species, whereas moderate humidity (40% to 70%, $p(\text{H}_2\text{O})=10$ torr or 1.3×10^3 Pa) yields primarily singly protonated cations or singly deprotonated anions. Mass spectra obtained with APPIS are similar to those recorded with atmospheric pressure chemical ionization using a corona discharge, further supporting the conjecture that electrical discharges are responsible for ion formation with APPIS. To extend the applications of APPIS, chemical nerve agent simulants were analyzed. The species 2-(butylamino)-ethanethiol (simulant for VX, member of the V agent class)

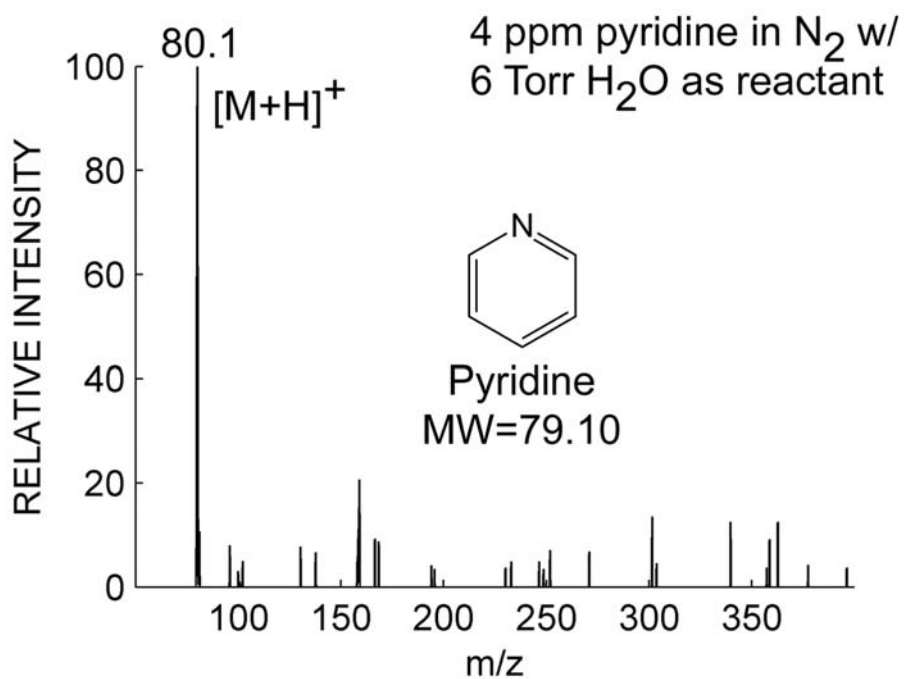


Figure 3.5: Mass spectrum of 4 ppm pyridine in doped nitrogen.

Mass spectrum of 4 ppm pyridine in nitrogen, with 6 Torr H₂O as reagent gas. Good signal-to-noise for the measurement indicates APPIS has an ultimate sensitivity for this chemical down to high part-per-billion range.

and diethyl phosphoramidate (simulant for Tabun, member of the G agent class) were detected either as singly protonated species or dimeric complexes in APPIS mass spectra, suggesting possible future use of an optimized source for the detection of volatile chemical warfare agents. Pyridine was readily detected down to concentrations of 4 ppm, suggesting ultimate sensitivity of APPIS for a fully optimized system in the high part-per-billion range.

Chapter 4

Switched Ferroelectric Plasma Ionizer (SwiFerr) for Ambient Mass Spectrometry

The implementation of a switched ferroelectric plasma ionizer (SwiFerr) for ambient analysis of trace substances by mass spectrometry is presented. The device utilizes the ferroelectric properties of barium titanate (BaTiO_3) to take advantage of the high electric field resulting from polarization switching in the material. The source comprises a [001] oriented barium titanate crystal (5 x 5 x 1 mm) with a metallic rear electrode and a metallic grid front electrode. When a high voltage AC waveform is applied to the rear electrode to switch polarization, the resulting electric field on the face of the crystal promotes electron emission and results in plasma formation between the crystal face and the grounded grid at ambient pressure. Interaction with this plasma and the resulting reagent ions effects ionization of trace neutrals. The source requires less than one watt of power to operate under most circumstances, ionizes molecules with acidic and basic functional groups easily, and has proven quite versatile for ambient analysis of both vapor phase and solid phase samples. Ionization of vapor phase samples of the organics triethylamine, tripropylamine, and tributylamine, and pyridine results in observation of the singly protonated species in the positive ion mass spectrum with sensitivity extending into the low ppm range. With acetic acid, deprotonated clusters dominate the negative ion mass spectrum. Aerodynamic sampling of powdered samples was used to record mass spectra of the pharmaceuticals

loperamide and ibuprofen. Chemical signatures, including protonated loperamide and ibuprofen, are observed for each drug. The robust, low-power source lends itself easily to miniaturization and incorporation in field portable devices used for the rapid detection and characterization of trace substances and hazardous materials in a range of different environments.

4.1 Introduction

Ambient mass spectrometry has been defined practically as any method of ionization allowing for the sampling of analyte from a surface or ambient atmosphere without advance sample preparation, occurring at ambient pressure. There are a number of somewhat distinct methodologies for ambient mass spectrometry. Several, like desorption electrospray ionization (DESI) [33], are derived primarily from electrospray ionization (ESI). Others utilize laser desorption to volatilize the sample, including ambient pressure matrix assisted laser desorption ionization (AP-MALDI) [34], [35]. These methodologies are combined in hybrid techniques which utilize both ESI and MALDI for sample volatilization and ionization, including MALDESI [36] and ELDI [37]. The last class of prominent methods are electrical discharge or plasma based, and include including the low temperature plasma probe [38] [39], direct analysis in real time (DART) [40] and plasma-assisted desorption/ionization (PADI) [41]. In just the last half decade, the field of ambient mass spectrometry has grown from just a few to nearly 40 different techniques. Excellent reviews on the subject of ambient ionization which give a comprehensive listing of the ionization sources available for both surface sampling [42] and ambient [43] mass spectrometry as well as ion mobility spectrometry [44] are also available.

An ambient pressure pyroelectric ionization source (APPIS) for mass spectrometry based on pyroelectric lithium tantalate has been recently described. Owing to their non-centrosymmetric crystal structure, pyroelectric materials possess a spontaneous polarization P_s which changes in magnitude with temperature change. The lithium tantalate material used in the APPIS source is also ferroelectric, another property

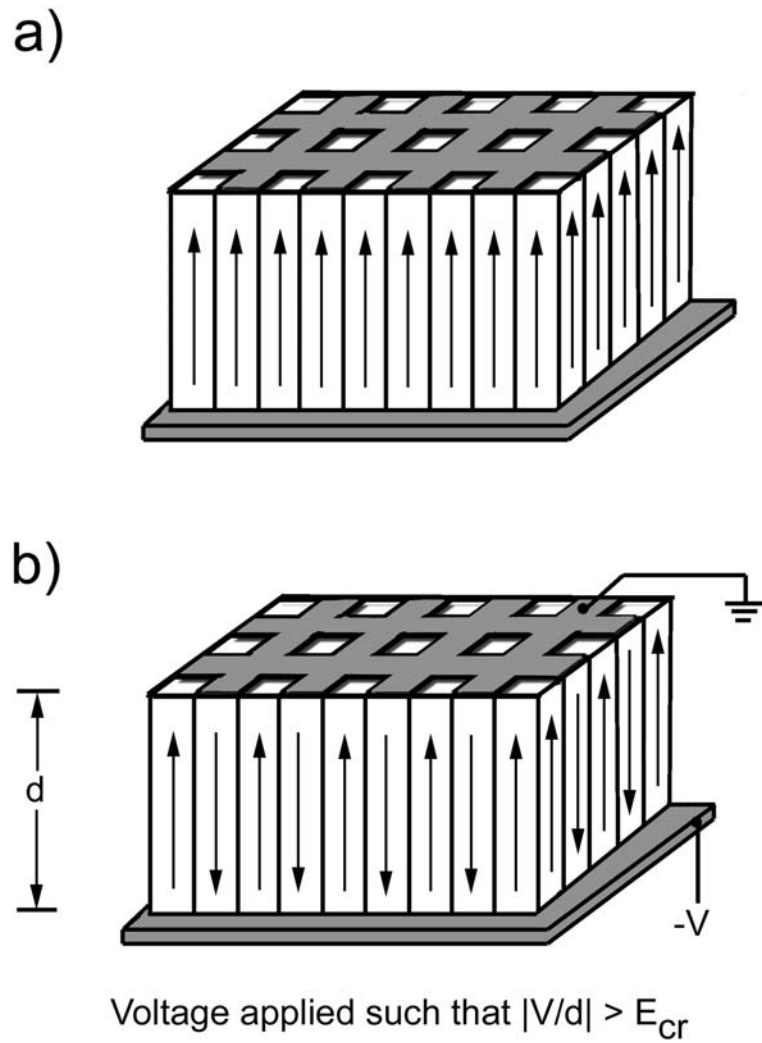


Figure 4.1: Domain formation in a switched ferroelectric

a) Crystal with uniform polarization, where the polarization of all regions is identical. b) Crystal with formed domains as a result of ferroelectric switching. Domain walls, or boundaries between regions of opposite polarization, are formed. At the surface of the material, an electric field exists across the domain wall.

dependent on a non-centrosymmetric crystal structure. Ferroelectric materials are unique in that they have a spontaneous polarization which is electrically switchable. The net polarization of a substance is a consequence of crystal structure asymmetry leading to a net dipole in the unit cell of the material. A material is uniformly polarized when all regions have the same polarization, as in Figure 4.1a. Because the material is ferroelectric, the polarization of any region can be changed by applying an electric field greater than the coercive field E_c . If a grid electrode is present, such as in Figure 4.1b, regions with different orientations of P_s (termed ‘domains’) are formed. The coercive field varies from material to material, and is dependent on the dielectric constant of the material in the direction of polarization as well as the bulk spontaneous polarization.

$$E_c = \pm \frac{2}{3\sqrt{3}} \sqrt{\frac{\alpha^3}{\beta}} \approx 0.385\alpha P_s \quad (4.1)$$

Equation 4.1 is an expression for calculating the coercive field for a material, where $\alpha = 1/(2\epsilon_{ij})$, $\beta \approx \alpha/P_s^2$, and ϵ_{ij} is the dielectric constant in the direction of polarization. Kim and co-workers [46] also observe that experimentally determined values for E_c are often at least one order of magnitude lower than calculated values, owing to physical processes occurring during domain wall formation. Experimentally, a coercive field of 20 kV mm⁻¹ is found for lithium niobate [47] while a field as little as 100 V mm⁻¹ is found for triglycine sulfate [48]. Barium titanate (BaTiO₃) has a coercive field of approximately 500 V mm⁻¹ [49].

A plasma can arise on the surface of a switched ferroelectric material as a consequence of electron emission resulting from the large electric field created across domain walls when a switching electrode is nearby. Ferroelectric electron emission is a well known and well studied phenomenon [50] that results in ionization of ambient gases at both reduced (ultra high vacuum) and ambient pressures. Switched ferroelectric plasmas resulting from electron emission have been used previously in a number of applications [51], mainly involving high current electron emitters. Although several reports of ion production by switched ferroelectrics at reduced pressure have been

published [52]–[55], ambient pressure plasma formation [56]–[59] has not previously been used as a source of ions for ambient mass spectrometric analysis.

A novel ion source for ambient mass spectrometry termed the switched ferroelectric plasma ionizer (SwiFerr) is presented, which utilizes the ambient pressure plasma resulting from a sample of barium titanate [001] whose polarization is switched by an audio frequency electric field. High yields of both anions and cations are produced by the source and easily detected using an ion trap mass spectrometer. Vapor phase samples of amines and volatile acids resulted in detection of the protonated and deprotonated species, respectively, in the observed mass spectra. Aerodynamic sampling was employed to analyze powders of drug tablets of loperamide and ibuprofen. A peak corresponding to the active pharmaceutical ingredient for each drug was observed in the mass spectra. Pyridine was detected at concentrations in the low part-per-million range in air, suggesting that the ultimate sensitivity of the source is the high ppb range. A detailed analysis of operating conditions to optimize sensitivity consistent with the goal of minimizing power consumption is presented. The low power consumption of the source suggests future incorporation into field portable instrumentation used for detection of trace substances and hazards in different situations.

4.2 Experimental

4.2.1 Design and construction of SwiFerr ionizer

Figure 4.2a is an overview of the arrangement of the SwiFerr source with respect to the mass spectrometer inlet. The ion source is attached to the atmospheric pressure inlet of an LCQ Deca XP ion trap mass spectrometer using a machined interface plate. Vapor or aerosol samples are drawn into the source due to the gas flow induced by the atmospheric pressure sampling capillary being backed by vacuum. An air gap of 1–2 mm is maintained between the source sample inlet and aspirator exhaust so that the source is not pressurized when the aspirator is operated using compressed air.

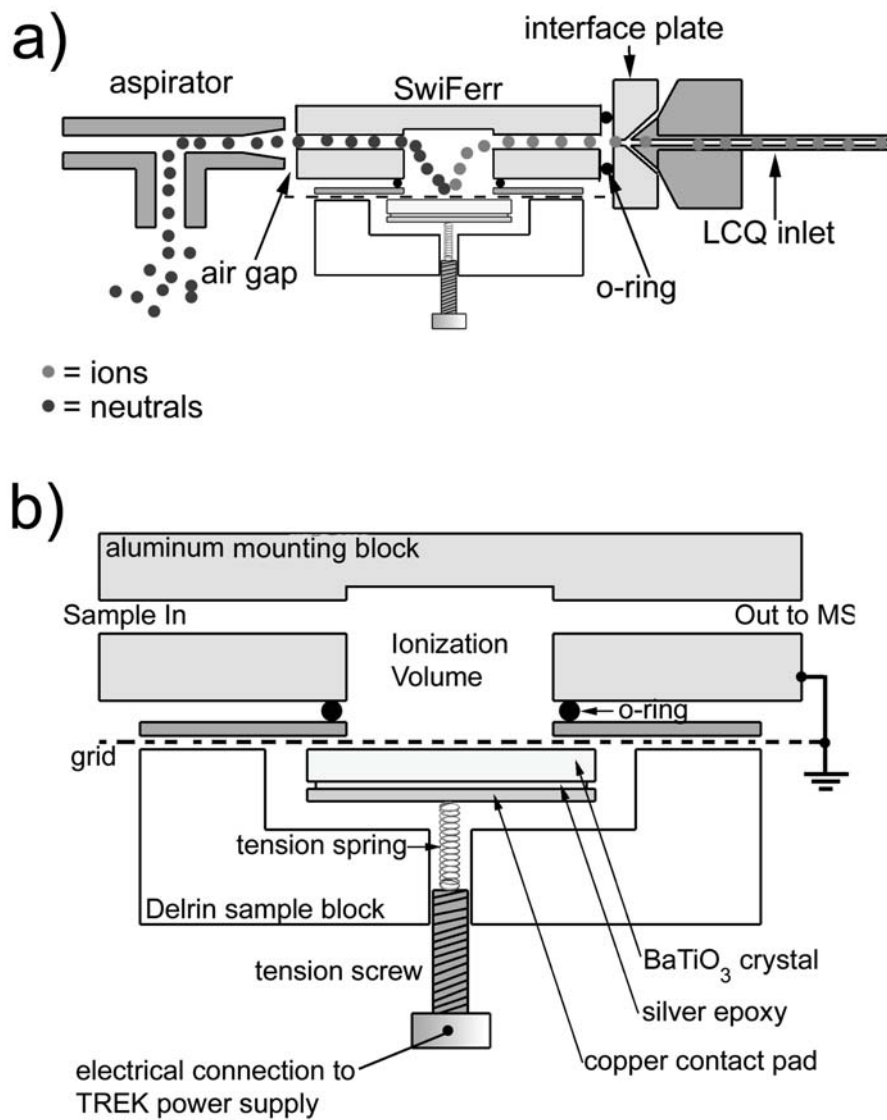


Figure 4.2: Schematic of SwiFerr source

a) Overview of the source arrangement in front of the mass spectrometer inlet. The source is attached to the atmospheric pressure inlet capillary using a machined interface plate. An air gap is maintained between the aspirator exhaust and source inlet.

b) Detail of the source. A 5 x 5 x 1 mm sample of [001] barium titanate with contact pad attached is placed in a Delrin sample block, and a copper mesh grid and aperture plate is placed on top of the sample. The aluminum mounting block is isolated from the aperture plate by an o-ring. Electrical connections to the source are made using the tension screw (connection point for high voltage waveform) and the grid. When affixed to the mass spectrometer, sample is drawn into the ‘sample in’ port, passed through the ionization volume where ionization occurs, and exits the source and enters the mass spectrometer. The grid and mounting block are maintained at ground potential throughout the experiment.

Figure 4.2b is a detailed schematic of the SwiFerr source itself. The device utilizes a 5 x 5 x 1 mm sample of single crystal barium titanate oriented in the [001] direction with one face polished (MTI Corporation, Richmond, CA, USA). Barium titanate has three phase transition temperatures, or Curie temperatures, and four phases, three of which are ferroelectric. Below 183 K, BaTiO₃ is rhombohedral, polarized along the [111] axis. From 183 K to 278 K it is orthorhombic, polarized along the [011] axis. From 278 K to 393 K, BaTiO₃ is tetragonal and polarized along the [001] axis and this is the orientation used in the current application owing to its intended use as an ionizer at ambient temperature and pressure. A contact pad comprising a 4.8 mm diameter disc cut from a 0.5 mm thick oxygen-free copper sheet is attached to the unpolished side of the crystal using silver conducting epoxy (MG Chemicals, Toronto, Ontario, Canada). A layer of silver epoxy achieving full coverage of the crystal face is first applied and allowed to cure before the contact pad is bonded using a second application of silver epoxy. The crystal with contact pad on one side is placed in a sample holder block machined from white Delrin, and a piece of woven copper mesh (0.230 mm diameter wire and 0.630 mm wire spacing) larger than the crystal surface area is placed on top of the face that does not have an electrode. An aperture plate (SS-PL-B-R187, Kimball Physics, Wilton, NH USA) is placed on top of the copper mesh. The aperture plate is vibrationally isolated from the mounting block using a silicone o-ring.

For detection of ions, a Thermo Scientific LCQ Deca XP ion trap mass spectrometer was used without modification other than the electrospray source being removed and replaced with the SwiFerr. Inlet capillary temperature was 40–70 °C, and the capillary was held at ground potential. To operate the source, an audio frequency high voltage sine wave was applied to the rear electrode of the barium titanate sample by making an electrical connection to the tension screw, while the copper mesh and aperture plate were maintained at ground potential by making an electrical connection to the mesh electrode. The waveform was generated using a TREK PM101494A high voltage amplifier/generator (TREK Inc, Medina, NY, USA) and can be varied in frequency from 0.1 to 10 kHz and in voltage from 0 to 20 kV p-p for testing purposes.

All chemicals were used as received, without further purification. Sample concentrations, when not specified, are unknown owing to the fact that the sample used was neat vapor arising from the room temperature vapor pressure of the sample being tested, or aerosol particles in the case of an sampled solids. For pharmaceutical sampling, a tablet of each drug was ground in a mortar and pestle before sampling. The tablets were commercial samples obtained from drug stores, rather than being pure samples of the active pharmaceutical ingredient purchased from a chemical supplier.

4.3 Results and Discussion

4.3.1 Ambient ionization of vapor phase and solid samples

SwiFerr was used to ionize and detect a variety of samples ranging from organic vapors to samples of drug tablets. Both cations and anions are produced by the source, and the ion signal observed appears continuous when an ion trap mass spectrometer is used for detection. Figure 4.3a shows mass spectra of the amines triethylamine, tripropylamine, and tributylamine ionized by SwiFerr under ambient conditions. The samples were introduced as neat vapor at room temperature. Each amine was detected as a singly protonated quasimolecular $(M+H)^+$ ion, owing to the basicity of tertiary amines. An aerodynamic sampling arrangement utilizing a pneumatic aspirator similar to that of Dixon [60] was used to sample powder from drug tablets. A tablet containing the pharmaceutical compound loperamide was crushed in a mortar and pestle and ground to a fine powder. The powder was aspirated into the SwiFerr source and the peak for loperamide was observed as the base peak in the mass spectrum (Figure 4.3b). Like the vapor phase samples, loperamide also contains tertiary amine functionality and was detected as the singly protonated species in the mass spectrum. Figure 4.3c is an example of negative ion production with SwiFerr for a vapor phase sample of acetic acid. Deprotonated clusters of the acid dominate the SwiFerr mass spectrum. The drug ibuprofen was aerodynamically sampled and detected using SwiFerr in the same manner as loperamide, except that anions were

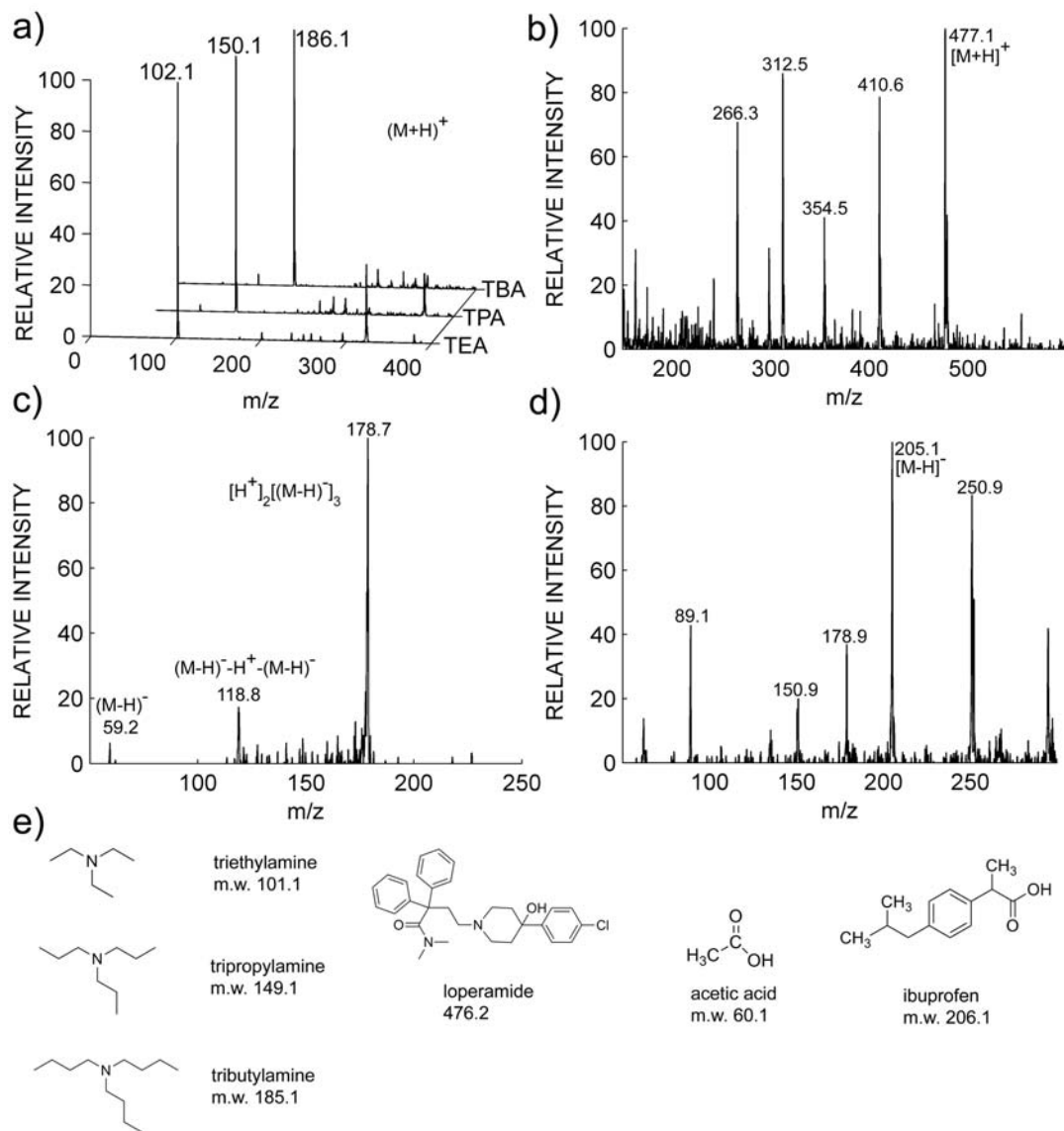


Figure 4.3: Mass spectra of test compounds using SwiFerr

a) Positive mode mass spectra of triethylamine, tripropylamine, and tributylamine ionized with SwiFerr. The singly protonated quasimolecular ion $(M+H)^+$ is observed for each amine. b) Positive mode mass spectrum of a ground tablet of loperamide ionized with SwiFerr. Protonated loperamide is observed as the base peak in the mass spectrum. c) Negative mode mass spectrum of acetic acid vapor obtained using SwiFerr. Monomeric acetic acid (m/z 59.2) as well as the proton bound dimer (m/z 118.8) and trimer (m/z 178.7) are observed. d) Negative mode mass spectrum of a ground tablet of ibuprofen ionized with SwiFerr. Deprotonated ibuprofen (m/z 205.1) is observed as the base peak in the mass spectrum. The peak at 250.9 is suspected to be due to the polymeric tablet coating. e) Structures and molecular weights for species in Figure 4.3a-d.

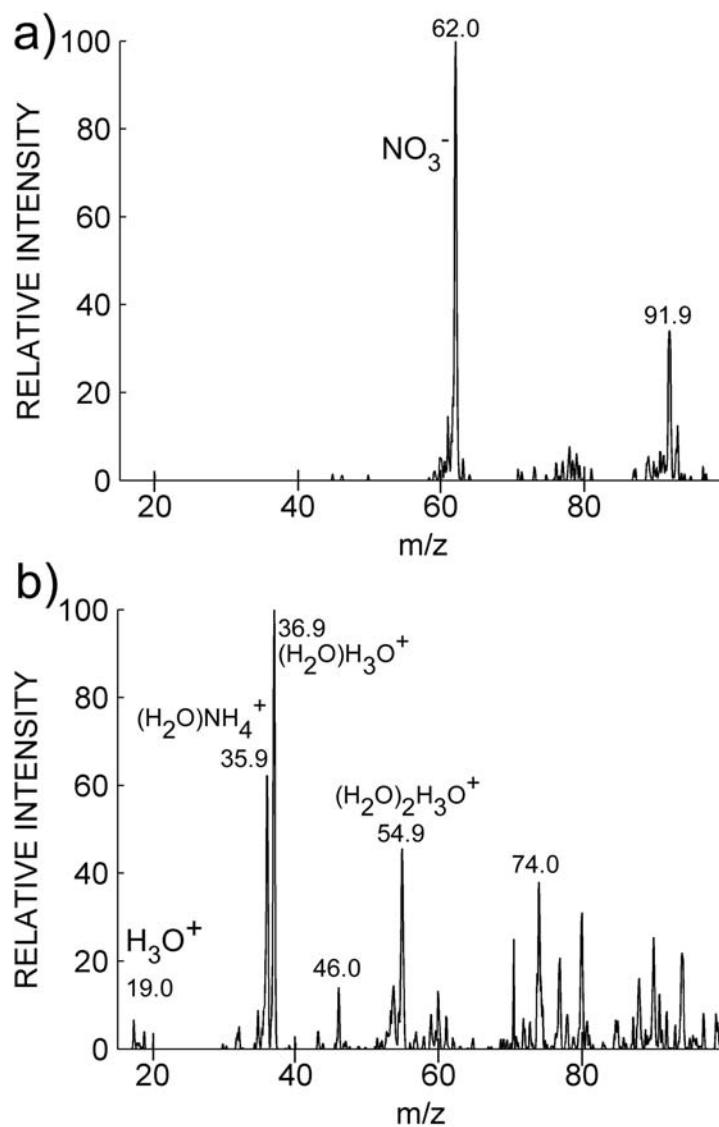


Figure 4.4: Reactant ions observed for SwiFerr

a) Negative mode mass spectrum of reagent ions resultant from the operation of SwiFerr in air. Nitrate anion was observed, and can take part in proton transfer reactions which ionize neutrals. b) Positive mode mass spectrum of ions resultant from the operation of SwiFerr in air. Hydrated protons (clusters of neutral water molecules and hydronium ion) are present which can take part in proton transfer reactions which ionize neutrals.

analyzed. Ibuprofen was detected as the singly deprotonated species in the mass spectrum (Figure 4.3d) owing to the fact that it possesses carboxylic acid functionality. The ability of SwiFerr to ionize acids and bases by deprotonation and protonation, respectively, suggests chemical ionization as the chief ionization mode of the source. Reactant ions such as nitrate anion and hydrated protons are directly observed in experiments measuring ions resultant from the operation of SwiFerr in air (Figure 4.4). The observed reactant ions take part in proton transfer reactions which can either deprotonate acids or protonate bases, and their presence indicates that the ionization mechanism operative in SwiFerr is ambient pressure chemical ionization, which is common for discharge based ion sources.

4.3.2 Limit of detection for organic vapors

The limit of detection (LOD) for some organic vapors with SwiFerr was investigated using mixtures of organic vapors in nitrogen doped with water vapor as the reactant ion. A sample of 50 ppm pyridine in nitrogen containing 6 Torr water vapor was analyzed using SwiFerr at various concentrations. Concentration was varied online using a model 1010 gas diluter (Custom Sensor Solutions, Oro Valley, AZ, USA) which allows for dilution of a prepared mixture by a factor of two to 50. In this case, a concentration from 25 to 1 part per million pyridine was available for analysis. Figure 4.5 is a mass spectrum of pyridine at a concentration of 4 ppm. Protonated pyridine appears at 80.1 m/z. Other peaks in the spectrum are not resultant from ionization of pyridine. Detection of pyridine readily at 4 ppm suggests ultimate sensitivity of the ionizer to concentration to be in the high part-per-billion range under optimal sampling conditions.

4.3.3 Optimization of parameters for source operation

Power consumption of the source was investigated by monitoring the RMS current required for source operation at various operating frequencies concurrently with ion signal observed in the mass spectrometer. Monitor functions on the TREK supply

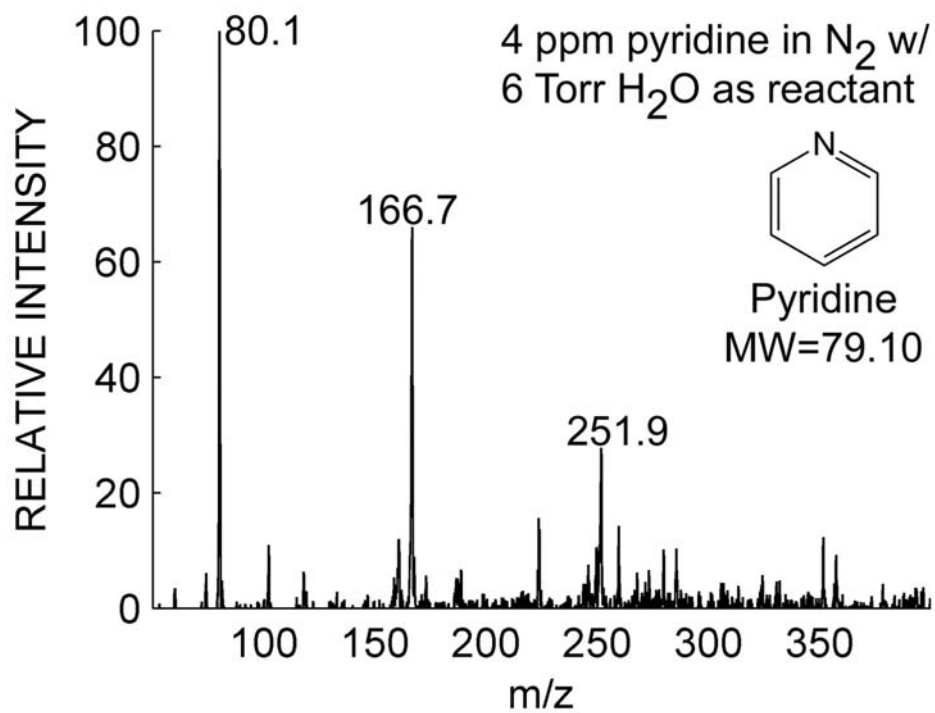


Figure 4.5: Positive mode mass spectrum of 4 ppm pyridine in nitrogen

Positive mode mass spectrum of 4 ppm pyridine in nitrogen doped with water obtained with SwiFerr. The ultimate sensitivity of SwiFerr is suspected to be in the part-per-billion range. Other peaks in the spectrum are likely impurities, and the intensities of these peaks are also modulated with concentration.

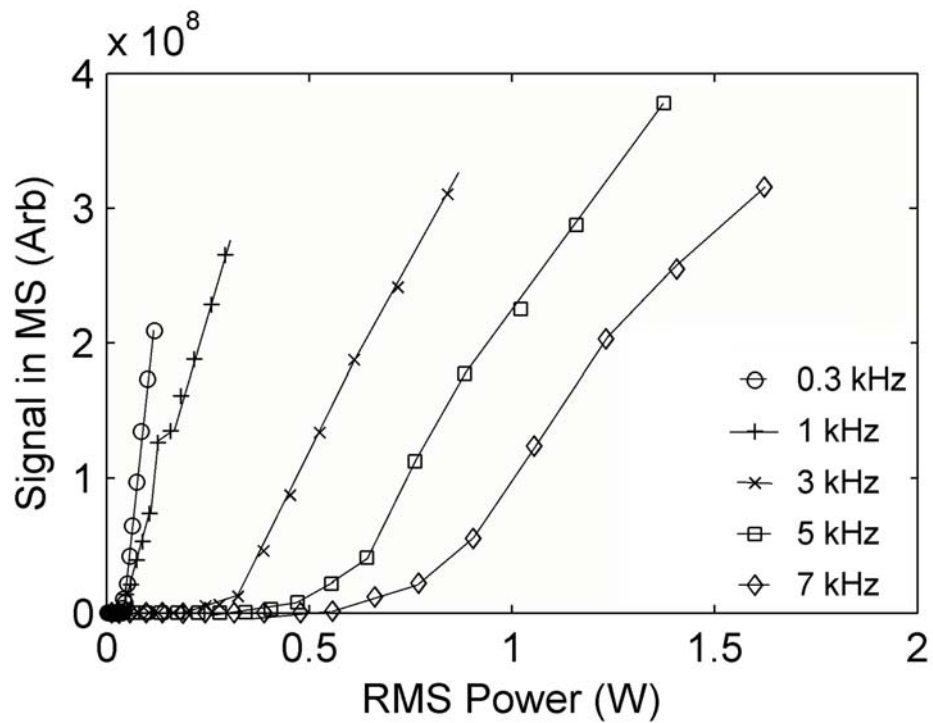


Figure 4.6: Power consumption of SwiFerr source

Plot of signal observed in mass spectrometer for a sample of lab air background versus RMS power for driving the crystal circuit at various frequencies. The source appears to ionize more efficiently at lower frequencies.

provided readings of RMS power as well as p-p voltage output. For a sample comprising laboratory air background, Figure 4.6 shows RMS power consumption for source operation. More power is consumed during operation at higher frequencies with no increase in ion signal, indicating that the source operates more efficiently at lower frequency. The fact that the current flowing in the circuit driving the switched crystal (and thereby power consumption by the source) increases with frequency is a result of the series RC nature of the circuit. The crystal itself has a characteristic resistance and capacitance which acts like a series RC element.

$$P = \frac{V_{RMS}^2}{\sqrt{R^2 + X_C^2}}, X_C \equiv \frac{1}{\omega C} \quad (4.2)$$

Equation 4.2 is an expression for the power flowing in the circuit, where R is the characteristic resistance and X_C is the capacitive reactance. Capacitive reactance X_C decreases with an increase in frequency, leading to a lower total impedance of the source ($\sqrt{R^2 + X_C^2}$) and increased current flow through the circuit element. Understanding the behavior of the SwiFerr source in the electrical circuit allows for the selection of optimal operating parameters with respect to power consumption and the level of ion signal detected. Since no gain is made in observed ion signal when operating at higher excitation powers, we typically operate the source at a frequency of 1 kHz and adjust the peak-to-peak excitation voltage to a level which produces a satisfactory ion signal for each specific experiment (typically below 354 V RMS). This corresponds to an operating power of approximately 0.2 W for this plasma ionizer.

4.4 Conclusion

A novel ion source for ambient mass spectrometry has been developed which utilizes the plasma formed on the surface of a switched ferroelectric material in close proximity to a grounded grid electrode for ionization of trace neutrals at ambient pressure, with good sensitivity and using very little power. Both anions and cations are observed from the same source arrangement due to chemical ionization because of reactive

species produced by the plasma. Basic species such as triethylamine, tripropylamine, and tributylamine, as well as the pharmaceutical loperamide, were detected as singly protonated cations in the mass spectra. Acidic species such as acetic acid and the pharmaceutical ibuprofen were detected as singly deprotonated anions. In the case of acetic acid, proton bound clusters of the anion were also detected. Sensitivity of the source to sample concentration was tested using a gas dilution method and pyridine was detected readily down to concentrations in the low part-per-million range, indicating performance of SwiFerr suitable for use in analytical applications. Lastly, electrical characteristics and power consumption of the source were analyzed. The source consumes less than one watt of power under normal operation, which is unique for a plasma based ionization technique. The variation of power consumption with frequency is a consequence of the capacitance of the crystal and the fact that higher frequencies excite that capacitance more efficiently. As a result, operation at lower frequencies is desired when the minimization of power consumption is a goal.

Chapter 5

Second-Generation Switched Ferroelectric Source and its Application to Trace Explosives Detection

A miniaturized embodiment of the switched ferroelectric plasma ionizer (SwiFerr) is presented. An ion source and housing half the size and more durable than the original design was constructed and tested with organic vapors and solid samples. The revised source design fits inside the bore of a modified 1/8" Swagelok tee fitting, which allows for the construction of a sealed source. Sealing the ion source allows for good sensitivity by increasing the probability of interaction between reagent ions and analytes. The miniaturized source is constructed in a unibody fashion using appropriate conductive and non-conductive adhesives and does not require external mounting hardware, which had been a source of contamination in the past. An application of the new source design is presented which is the detection of nanogram quantities of explosives. Trinitrotoluene (TNT) was introduced into the source using a rudimentary thermal desorption apparatus and ionization by SwiFerr produced the TNT radical anion which was detected with good sensitivity. The source consumes approximately 0.4 W of power under normal operation, which is well within the acceptable range for sources used in field portable instrumentation. Increased power usage for the miniaturized design relative to the original design is likely due to increased capacitance in the source, the source of which is most likely more efficient

polarization switching and plasma production.

5.1 Introduction

Continuous development in ambient pressure ionization sources has brought about the APPIS and SwiFerr sources, presented in previous chapters. Demonstrated applications of these sources include the analysis of generic organic vapors, chemical warfare agents, and the sampling of unknown powders by aspiration followed by analysis by mass spectrometry. An application not yet addressed has been the detection of various explosives materials using mass spectrometry, with ionization by either APPIS or SwiFerr. Some explosives, such as RDX or PETN, are detected as singly protonated cations [33] and both APPIS and SwiFerr ionize in suitable fashion as to be able to detect such chemicals. Reagent ions such as hydrated protons and ammonium cation are produced which can participate in proton transfer reactions with analytes having higher proton affinity than water, and are detected as cations. Other explosives, such as the nitrotoluenes and nitrobenzenes, are generally detected as anions [61], sometimes as singly deprotonated ions or as radical anions formed by electron attachment. The former case has been demonstrated with benzoic acid, hexafluoroisopropanol, and acetic acid; the case with electron attachment has not yet been demonstrated with APPIS or SwiFerr. Since both are electrical discharge based, and the electrical discharge arises from either high negative potentials on the crystal face (APPIS) or ferroelectric switching (SwiFerr) and both cases have been shown to produce free electrons, it should be possible to form radical anions by electron attachment using SwiFerr.

In the previous chapter, the first-generation design of the switched ferroelectric plasma ionizer (SwiFerr) was introduced. SwiFerr comprises a 1 mm thick crystal of [001] oriented barium titanate with an electrode on one side and a metallic grid electrode on the other. When a high voltage AC waveform is applied to the rear electrode while the front grid electrode remains at ground potential, domain structure is formed and the polarization of some regions is switched. The high electric fields

across domain walls that are present during polarization switching promote electron emission and plasma formation from the material. Plasma formation at ambient pressure which results in reagent ions for chemical ionization is the chief mode of ionization of this source. Reactions involving proton transfer with reagent ions such as ${}^+H(H_2O)_n$ and NO_3^- were previously observed. Amines and other basic species were often observed as the singly protonated species, while acids were observed as singly deprotonated species in the mass spectrum.

Mounting and electrical connections for the source were achieved with machined parts, and sealing of the source was achieved using o-rings. When occasions of high analyte concentration occurred, the source would often become contaminated owing to the many surfaces for adsorption. In order to improve source performance, protect from contamination, and achieve further miniaturization, a revised construction of the SwiFerr source was made using a crystal half the size of the previous with different electroding and electrical contacting methods. The new source comprises a 2.5 x 5 x 1 mm thick barium titanate crystal with front and rear electrodes as well as electrical contacts constructed in a unibody fashion. The housing for the source is now a modified Swagelok tee fitting which not only contributes to improved sealing of the source but also aids in easily integrating SwiFerr into existing systems. Figure 5.1 is a photograph showing the source outside its housing, next to a dime for scale. The revised source exhibits good sensitivity, and an application whereby trace quantities of explosives are detected following thermal desorption is presented. Trinitrotoluene was introduced into the source using a rudimentary thermal desorption apparatus, and ionized by SwiFerr. The anion of TNT, as well as a peak corresponding to the loss of NO, was observed and is consistent with previous work on TNT using ambient ionization. Lastly, power consumption and capacitance measurements were made to characterize the source electrically.



Figure 5.1: Miniaturized SwiFerr source near a dime for scale

Miniaturized SwiFerr source near a dime for scale. The source is considerably smaller than the coin itself. The small size of the source should allow for easy integration into field portable devices for chemical analysis.

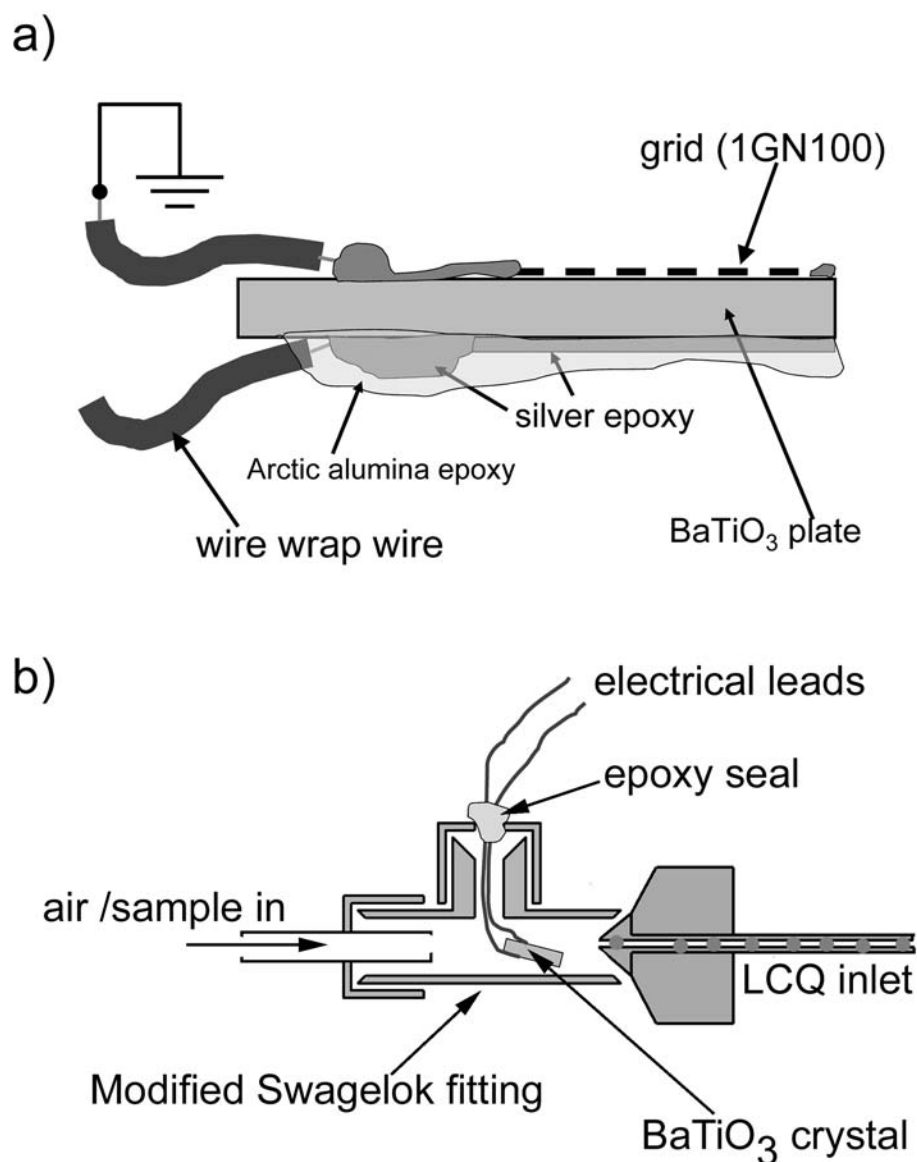


Figure 5.2: Schematic of second-generation SwiFerr ion source

Schematic of second-generation SwiFerr ion source. a) A 2.5 x 5 x 5 BaTiO₃ crystal has electrodes, a grid, and electrical contact wires attached using silver conducting epoxy. The high voltage side of the source is potted with Arctic Alumina thermal adhesive, which is non-conducting. Electrical contact wires are Kynar insulated wire-wrap wire. b) Crystal assembly is inserted into a 1/8" Swagelok tee fitting which has been modified by drilling the main bore out to 4.8 mm. Electrical wires exit through the top of the tee fitting and are sealed using five minute epoxy. Air and sample to be analyzed come in one side of the tee fitting, pass near the crystal and plasma, and exit the fitting into the ion trap mass spectrometer.

5.2 Experimental

Figure 5.2a is a schematic of the miniature SwiFerr source; Figure 5.2b shows the source arrangement in front of the mass spectrometer. The source comprises a 2.5 x 5 x 1 mm sample of [001] oriented barium titanate with rear and top electrodes, and attached electrical leads. To construct the source, a rear electrode of silver conducting epoxy (MG Chemicals, Toronto, Ontario, Canada) was applied to the unpolished side of the crystal. To apply the electrode, a mask of Scotch tape was used to create a rectangular area on the unpolished side of the sample so that a thin layer of the epoxy can be wiped onto the crystal. After ten minutes, the mask is removed, leaving a rectangular electrode on one side of the crystal. Suitable curing time is allowed for the electrode before affixing the grid to the other side. The grid used is a nickel transmission electron microscope (TEM) grid (1GN100, Ted Pella Company, Redding, CA, USA). Three small spots of silver epoxy are applied to the polished side of the crystal, and the grid is laid onto those spots and pressed so that the maximum amount of contact is achieved between the grid and crystal face. Suitable cure time for the grid adhesive is allowed before beginning to affix contact wires to the assembly. The rear contact wire is affixed using silver epoxy. The wires used were Kynar insulated wire used for wire-wrap electronics construction. The Kynar insulation has sufficient dielectric strength that voltages on the order of 500 V RMS can be used without sparking if the insulation comes in contact with a grounded surface. After the rear electrode wire is attached, suitable cure time is allowed before attaching the wire to the front grid. Electrical contacting to the front grid is achieved again with silver epoxy. The wire is attached to the crystal face near the grid, and a track of epoxy connects the grid to the wire. The last step in source construction is to pot the rear high voltage electrode with Arctic Alumina thermal adhesive (Arctic Silver, Visalia, CA, USA) so that the source can be placed in contact with grounded metal. After the source is sufficiently insulated with the thermal adhesive and the adhesive is allowed to cure for a sufficient amount of time, it can be inserted into its housing.

A housing was constructed from a 1/8" Swagelok tee fitting having a bore which

was drilled out to a diameter of 4.8 mm so that the source could be inserted into it. The source was inserted such that the wires came out the top of the tee fitting, and the end of the source was approximately 6 mm from the end of the fitting. This allows for tubing connections to the output of the source. The wires were fed through a 1/8" OD, 1/16" ID section of polyethylene tubing and sealed off using 5 minute epoxy. The housing was held in front of the atmospheric pressure inlet of a Thermo Scientific LCQ Deca XP ion trap mass spectrometer using clamps. Gas flow rate through the source was 1000 SCCM compressed air which was from the air compressor serving the lab building. The source was operated with a 900 V p-p sine wave at a frequency of 1 kHz from a TREK high voltage power supply/generator (TREK Inc, Medina, NY, USA).

Thermal desorption for study of explosives and other solid samples was achieved using a home-built apparatus. The device was constructed from a stainless steel Swagelok tee fitting which had been modified to accept a Thorlabs 15W cartridge heater. A slot was milled in the bottom portion of the fitting and the heater and a 10k thermistor were attached to the fitting using Arctic Alumina thermal adhesive. A Thorlabs TC200 temperature control unit was used to apply a temperature step function to the fitting, raising the temperature from 25 °C to 100 °C in approximately 20 seconds, which was sufficient for volatilization of small quantities of analyte. Analyte was deposited through the top port of the fitting with the gas flow turned off. Each chemical was present as a solution in acetonitrile. 2 μL was spotted onto the interior of the fitting and allowed to dry with gas flow turned off. The thermal desorption cell was then sealed and the gas flow turned on, followed by the heating which sublimed the sample. Ionization was achieved using SwiFerr, followed by detection in the ion trap mass spectrometer.

TNT was obtained from Sigma Aldrich (St. Louis, MO, USA) as a 1 mg/mL solution in acetonitrile. Serial dilution was used for preparing working solutions of TNT so that a 2 μL aliquot would allow for the deposition of nanogram quantities of the explosive. 4-cyanobenzoic acid was from Sigma. Samples for determination of detection limits for organic vapors were prepared by on-line dilution using a Model

1010 gas diluter (Custom Sensor Solutions, Oro Valley, AZ). Samples of diethyl ether were prepared by injecting 1 μL liquid diethyl ether into a 40 L capacity Tedlar sample bag, which was then filled with 33 L of air from the compressor supplying the lab building. The sample bag was then connected to the sample input of the gas diluter, whose output was then connected to the gas inlet port of the SwiFerr source. Dilutions were performed with a diluent bag also containing air from the laboratory supply. The gas diluter has usable dilution settings from 2% to 100%, meaning available concentration ranged from 2 to 100 percent of the prepared concentration.

5.3 Results and Discussion

As a proof of concept test for the thermal desorption apparatus, 4-cyanobenzoic acid was thermally desorbed and detected using SwiFerr. Figure 5.3 is a negative ion mass spectrum of thermally desorbed 4-cyanobenzoic acid, showing both the deprotonated acid as well as the proton bound dimer of the deprotonated acid. Good signal-to-noise was achieved for the measurement for a temperature change of approximately 100 °C. The acid was not expected to have significant vapor pressure relative to atmospheric pressure at room temperature, and a peak corresponding to the acid was not observed before heating. The successful detection of the substituted benzoic acid suggests that this thermal desorption apparatus is suitable for general use with nominally nonvolatile materials. For explosives detection, an aliquot of TNT in acetonitrile solution was deposited into the thermal desorption cell. Figure 5.4 is a mass spectrum of 20 ng TNT ionized with the miniature SwiFerr source after thermal desorption. Present in the mass spectrum are peaks for the TNT radical anion, as well as a peak for the species minus NO. This pattern is consistent with previous ambient ionization work done with TNT. The production of the radical anion of TNT illustrates the production of free electrons by SwiFerr, which is not unexpected owing to the presence of plasma. A new class of analytes are now detectable using SwiFerr, which is now not limited to those analytes ionized by proton transfer reactions.

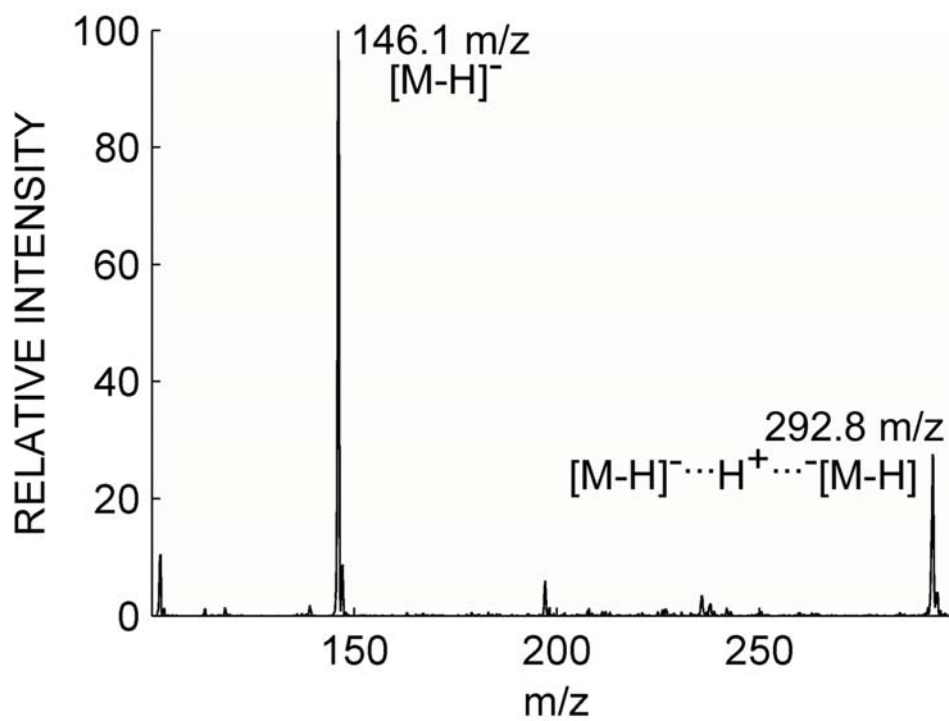


Figure 5.3: Mass spectrum of 4-cyanobenzoic acid by thermal desorption SwiFerr MS

Thermal desorption of a dried sample of 4-cyanobenzoic acid in acetonitrile sufficiently volatilized the sample so that ionization and detection with SwiFerr was possible. The deprotonated benzoic acid is observed in the mass spectrum as well as a proton bound dimer of the anion.

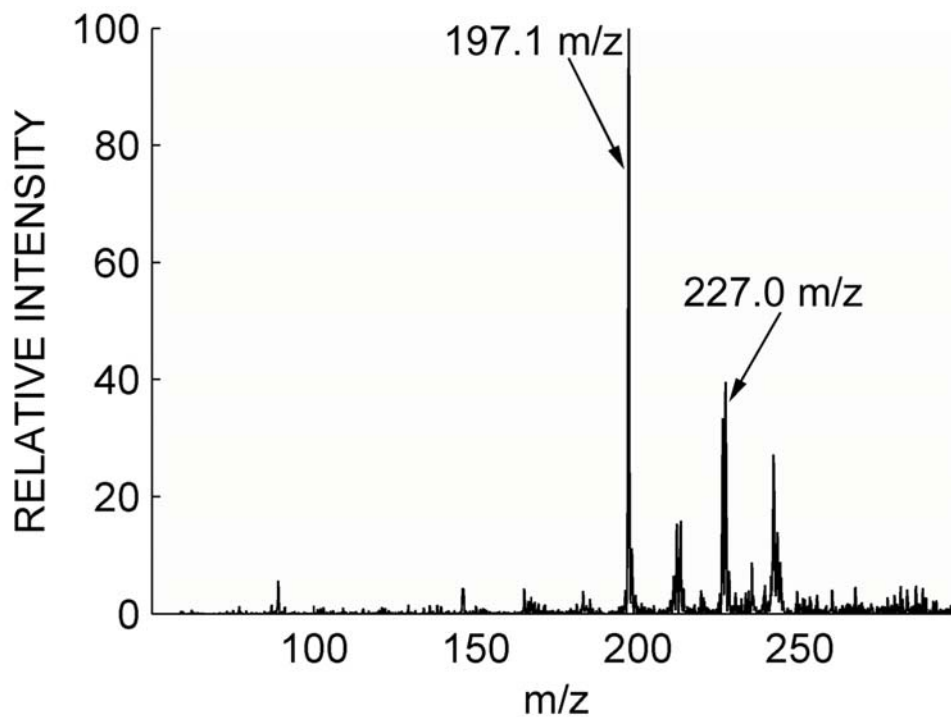


Figure 5.4: Mass spectrum of 20 ng TNT using thermal desorption SwiFerr

A 2 μL aliquot of 0.010 mg/mL TNT in acetonitrile was spotted into the thermal desorption cell. A temperature step function was applied and temperature was raised from 25 $^{\circ}\text{C}$ to 100 $^{\circ}\text{C}$ in a short time period. The radical anion of TNT is observed at 227.0 m/z. A product resulting from the loss of NO, at 197 m/z, is also observed. TNT has been seen previously to lose NO.

5.3.1 Limit of detection for organic vapors

Sample dilution experiments were performed to determine the performance and detection limits for SwiFerr. Diethyl ether was chosen as a test compound for performance evaluation. Samples of diethyl ether vapor were prepared in Tedlar sample bags and analyzed using SwiFerr. Figure 5.5a shows the detection of diethyl ether at a concentration of 2 ppm in air. Detection of diethyl ether at a concentration of 2 ppm with a signal-to-noise ratio of approximately 5 indicates that the ultimate sensitivity of SwiFerr for this compound, in the current source configuration, is likely in the high part per billion (ppb) range. Figure 5.5b is a plot relating sample concentration from the gas diluter to signal observed in the mass spectrometer. Decreased sensitivity at higher concentrations was observed and is likely due to saturation of the source region at high analyte concentrations as well a possible scenario where hydronium ion is a limiting reagent.



For Equation 5.1, at constant hydronium concentration and low $[M]$ there is sufficient reagent ion to produce a proportional amount of the species MH^+ . Once $[M]$ exceeds $[H_3O^+]$, MH^+ can no longer be created proportionally and sensitivity is lost. In practice with proton transfer reactions, especially commercial instrumentation, care is taken to maintain $[H_3O^+]$ at a level much higher than that of the analyte to avoid the problems with limiting reagents. In ambient air, with a water partial pressure of approximately 6–10 Torr, approximately 10000 ppm water is present, well in excess of any analyte concentration. With compressed air, care is taken not to condense water in the air lines and dewpoints are maintained at very low temperatures, meaning the compressed air is dry relative to ambient air.

5.3.2 Capacitance of revised source; Power usage

Since SwiFerr and its revised embodiment are intended for use in devices which are field portable, attention to the power consumption in the device is appropriate. It

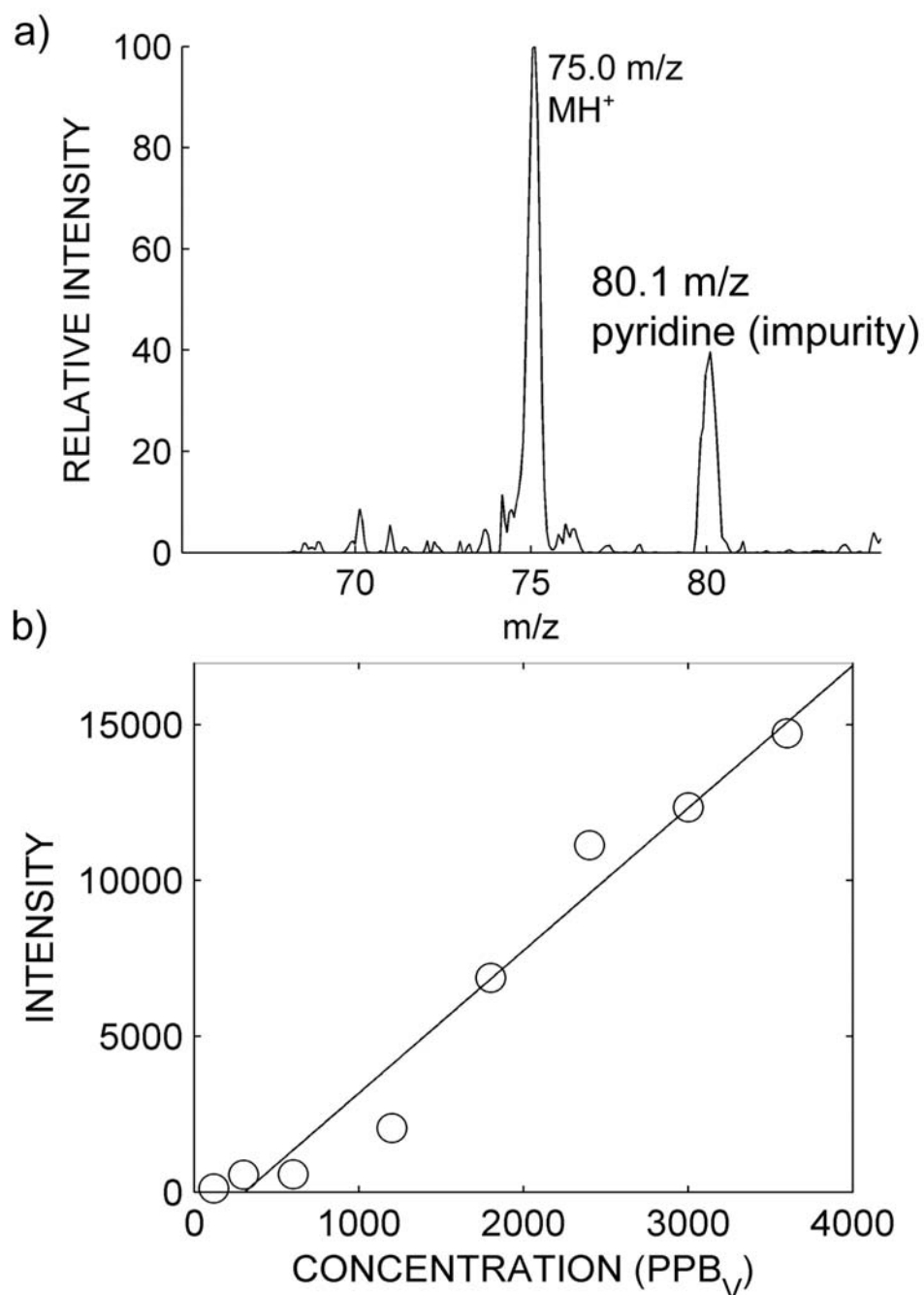


Figure 5.5: Mass spectrum of diethyl ether at 2 ppm and correlation of signal with concentration

a) Mass spectrum of diethyl ether at a concentration of 2 ppm. Good signal-to-noise ratio is achieved with background subtraction. b) Correlation of signal with concentration. Integrated signal for the diethyl ether peak rises in a linear fashion from approximately 100 ppb to 4 ppm. Above 4 ppm, saturation of the ion source region is thought to contribute to decreased signal.

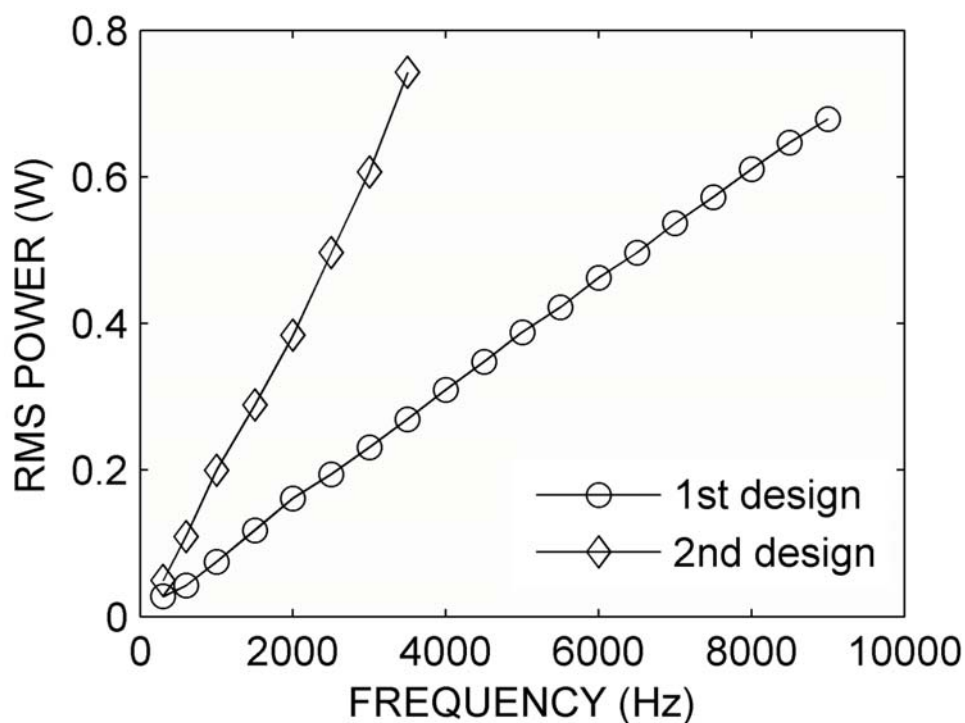


Figure 5.6: Variation of power consumed with frequency

Voltage was held constant at 600 V p-p (212 V RMS). The slope of the line is the capacitance of the crystal times the constant $V_{RMS}^2 2\pi f$. For the first SwiFerr embodiment, a capacitance of 2.7×10^{-10} F is calculated, while for the revised design a capacitance of 7.5×10^{-10} F is calculated. The increased capacitance in the revised source design is thought to originate from more efficient switching and plasma production as well as an effective increase in plate area for the capacitor created by the rear electrode, front grid electrode, and crystal dielectric material.

was found previously that lower frequency operation of the source is preferred with respect to power consumption, and that no gain in signal was found by operating at higher frequencies. Instead, higher frequency simply excited the source capacitance more efficiently and power consumption increased without a corresponding increase in signal. Power consumption varies significantly with frequency at constant voltage as shown in Figure 5.6 indicating that any resistive portion of impedance (the denominator in Equation 4.2) is negligible compared to capacitive effects.

$$P = V_{RMS}^2 2\pi f C \quad (5.2)$$

Reducing Equation 4.2 to the form of Equation 5.2 reveals that if a plot is made of power versus frequency, as in Figure 5.6 the slope of the line is the capacitance of the crystal times the constant $V_{RMS}^2 2\pi f$. Voltage was held constant at 600 V p-p (212 V RMS), and the capacitance values for the original SwiFerr source and the revised embodiment are 2.7×10^{-10} F and 7.5×10^{-10} F, respectively. Increased capacitance in the revised source design is suspected to result from more efficient polarization switching and plasma formation when using the TEM grid as opposed to the copper mesh. The TEM grid is a finer mesh, exposing more of the crystal face to ambient atmosphere and increasing the probability of favorable interaction between atmospheric water and the plasma. Also, the TEM grid being thinner effects better contact between the grid and crystal surface, increasing the electric fields across the domain walls at the surface as well as increasing the effective electrode area in the capacitor created by the front and rear electrode separated by the dielectric crystal.

Chapter 6

Free Radical Initiated Peptide Sequencing: Reactions of Carbon Centered Radicals with Amino Acids in Model Peptides

A systematic study of the reactivity of the acetyl radical with each of the 20 common amino acids has been performed. Vazo-68, a free radical initiator, was conjugated to the n-terminus of model peptides of the general sequence AARAAAXAA where X is any one of the 20 naturally occurring amino acids. With the radical initiator conjugated to the peptide, subsequent collisional activation generates a radical moiety where acetyl radical is attached to the n-terminus of the peptide. Activation of this radical species results mainly in reaction with the X amino acid and selective fragmentation of the peptide. Several distinct classes of reactivity are observed and the amino acids can be grouped according to their reactivity toward acetyl radical. Side chain specific fragmentations are observed for several amino acids, including leucine and isoleucine, allowing them to be readily distinguished. Fragmentation processes are attributed to hydrogen abstraction by the radical, typically followed by β -cleavage adjacent to the abstraction site.

6.1 Introduction

Proteins containing free radicals play important roles in many enzyme catalysis reactions [62]. In other environments, free radicals in peptides and proteins contribute to disease as well as the aging process [63]–[65]. As a result, there has been significant interest in the behavior of amino acids, peptides, and proteins that are attacked by radicals and the subsequent products of such reactions. Radical reactions can also elicit structural information about peptides and proteins, both in the gas phase and in solution. The solution phase radiolysis of such species has been extensively studied [66] and the reactions of hydroxyl radicals with amino acid side chains on proteins can be used to examine solvent-accessible sites in a protein [67], [68]. In these hydroxyl footprinting reactions, hydroxyl radicals preferentially react with side chains of amino acid residues.

In the gas phase, peptide radical cations can be generated by dissociation of complexes such as $[\text{Cu(II)}(\text{L}_3)\text{M}]^+$, where L_3 is a tridentate ligand [69]–[74]. The technique of electron capture dissociation consists of creating radical peptide or protein cations by irradiating a multiply charged biomolecule with low energy electrons [75]. The subsequent radical cation is then subjected to collisionally activated dissociation (CAD) to produce c and z type fragments. Many more backbone sites are cleaved in ECD than in collisional activation of non-radical peptides, resulting in more complete coverage of a peptide sequence [76]. Post-translational modifications such as phosphorylation and glycosylation are retained in the ECD process [77]–[79]. It is also possible to modify a peptide in solution to generate a radical species in the gas phase. Porter and co-workers modified lysine residues in solution to convert them to peroxy-carbamates and find that CAD of species complexed with Li^+ , Na^+ , K^+ , and Ag^+ gives a radical amine at the lysine side chain [80]. Further CAD of the radical peptide results mainly in fragmentation of the lysine side chain, but in some instances the peptide backbone is also cleaved.

Selective peptide cleavage by radical sites created photochemically has also been reported. Iodination of tyrosine residues followed by subsequent radical generation

by photolytic cleavage of the C–I bond creates a radical species which undergoes peptide backbone cleavage near the tyrosine residue [81]. Site specific fragmentation at phosphorylated residues was also achieved by insertion of a suitable C–S bond at a phosphorylated serine site in a peptide and subsequent radical formation by excitation of the attached naphthyl chromophore by ultraviolet radiation induced site specific cleavage in the modified peptide [82].

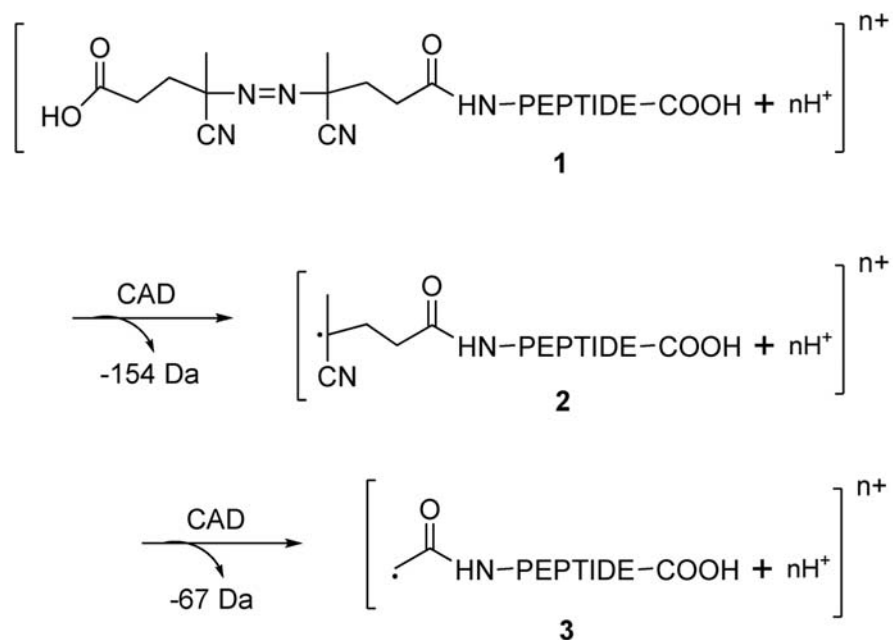
Recently, it has been proposed that selective fragmentation of a peptide can be achieved using free radical initiator-peptide conjugates [83]. A free radical initiator is covalently attached to a peptide on the N-terminus. Subsequently, the conjugate is electrosprayed into an ion trap mass spectrometer, where CAD results in free radical formation. Unlike ECD, singly charged peptides can be observed using this technique of free radical initiated peptide sequencing (FRIPS). Results for Angiotensin II were presented, showing the formation of *a* and *z* type ions. Here, the FRIPS technique is extended to examine a series of model peptides of general sequence AARAAAXAA (where X is any one of the 20 naturally occurring amino acids) in order to elucidate how the reaction of the carbon centered radical varies with each amino acid residue. Distinct classes of reactivity are observed, and principal fragmentation arising from the interaction of the radical moiety with any one of the amino acids can be classified into four groups. Two reactive classes include reactivity where backbone fragments are formed, one class comprises reactivity primarily of side chain losses from the amino acids, and one class exhibits loss of carbon dioxide from the modified peptide and no specific fragmentation is observed near the amino acid location in the sequence. For those amino acids exhibiting reactivity of the side chain, a fortuitous result is that leucine and isoleucine fragment in a different manner with the FRIPS technique, allowing for the identification of these isobaric amino acids during sequence determinations. Calculations of bond energies for the β hydrogen on the residue side chains correspond with the observed degree of cleavage for those residues exhibiting specific reactivity toward the radical and subsequent formation of modified *a* ions.

6.2 Experimental

Model peptides of the sequence AARAAAXAA (where X is any one of the 20 naturally occurring amino acids) were obtained from Biomer Technology (Hayward, CA, USA) as crude ($\approx 70\%$) purity. For the preparation of the peptide-radical initiator conjugate, The crude peptides were first diluted to 10 mg/mL in aqueous solution. For the conjugation reaction, A 20 μL aliquot of the peptide solution was combined with 10 μL of saturated Vazo-68 (DuPont) in aqueous solution and 10 μL of a stock 60 μM solution of *N*-(3-dimethylaminopropyl)-*N'*-ethylcarbodiimide hydrochloride, EDC. The mixture was allowed to react for a period of 1 to 8 hours, protected from light. Peptide conjugate purification and extraction was performed using C18 ZipTips (Millipore) in the standard fashion. This product (in 5 μL of a 1:1 water:methanol, 1% formic acid solution) was diluted to 250 μL with methanol and the solution was used for mass spectrometric studies with a Thermo Scientific LCQ Deca ion trap mass spectrometer. The mass spectrometer was without modification, and parameters for both the electrospray source and ion optics were varied to maximize the intensity of the ions of interest. Positive mode electrospray ionization was used for all experiments.

Peptide nomenclature in this chapter is derived from that of Biemann [85]. Modifications of the nomenclature are made to account for peptide conjugation to the free radical initiator and radical formation by collisional activation. Fragments that are modified by a radical are denoted Ma_n , $\text{Ma}_n\cdot$, etc. Radicals are created in the mass spectrometer from Vazo 68 as depicted in Scheme 6.1. Collisional activation of the conjugated peptide yields two major products: a fragment corresponding to the loss of 28 Da (loss of N_2), and another fragment corresponding to the loss of 154 Da. The latter ion is the free radical species generated by cleavage at the azo carbon. These processes are observed with all peptide-Vazo 68 conjugates we have studied thus far.

Subsequent dissociation of the radical species results in the formation of another radical ion formed by the loss of 2-methyl-acrylonitrile (loss of 67 Da). Also observed are a number of fragment ions, including *a* and *z* ions. Fragments with modifications



Scheme 6.1: Formation of acetyl radical conjugated to model peptide

Formation of acetyl radical conjugated to the model peptide. The initial conjugate, **1**, is formed using common conjugation chemistry which allows for the coupling of the free radical initiator having a carboxylic acid group to the n-terminus of a peptide. A stage of collisional activation produces species **2**. Activation of **2** can effect free radical chemistry, but is more commonly employed to obtain species **3** which contains the acetyl radical moiety. Species **3** is activated to perform a FRIPS experiment.

corresponding to radical **3** are observed, as well as fragments with modifications corresponding to radical **2**. The radical ion **3** can also be isolated and collisionally dissociated. In this chapter, results from the fragmentation of radical ion **3** will be discussed exclusively, as the fragment ions are exclusively from the radical **3**. Radical **3**-type ions are referred to throughout as ‘m(Peptide).’

6.3 Results and Discussion

Discussion of the reactivity of the radical species with each of the amino acids will be divided according to similar patterns of reactivity. It was found that of the 20 amino acids studied, four groups of reactivity were observed. One group comprises limited reactivity of the radical towards the X amino acid, resulting mainly in loss of 44 Da (loss of carbon dioxide) from the peptide. Another group shows formation primarily of an Ma_6 fragment. The largest group includes those amino acids exhibiting specific reactivity toward the X amino acid, and formation of an Ma_7 fragment. Lastly, a group where reactivity of the radical with the amino acid residue resulted in losses from the side chain of that amino acid.

6.3.1 Peptides containing residues X=G,A,P

Model peptides containing the residues G, A, or P did not exhibit specific backbone cleavage allowing for identification of the residue in sequence. Figure 6.1 is a mass spectrum depicting fragmentation of the modified peptide mAARAAAPAA, which is representative of reactivity of residues in this class. Loss of 44 amu is taken to be loss of carbon dioxide from the c-terminus of the peptide. Figure 6.2 shows the major fragmentation channels for each of the peptides in this class. Although a fragment corresponding to the loss of CO_2 was the major fragment observed, the peptide mAARAAAAAA also showed cleavage resulting in the formation of Ma_3 , Ma_5 , and Ma_6 fragments. No strong preference for cleavage position was observed with mAARAAAAAA, indicating that the acetyl radical moiety does not exhibit a distinct chain length specific (vinculoselective) cleavage behavior. A slight preference

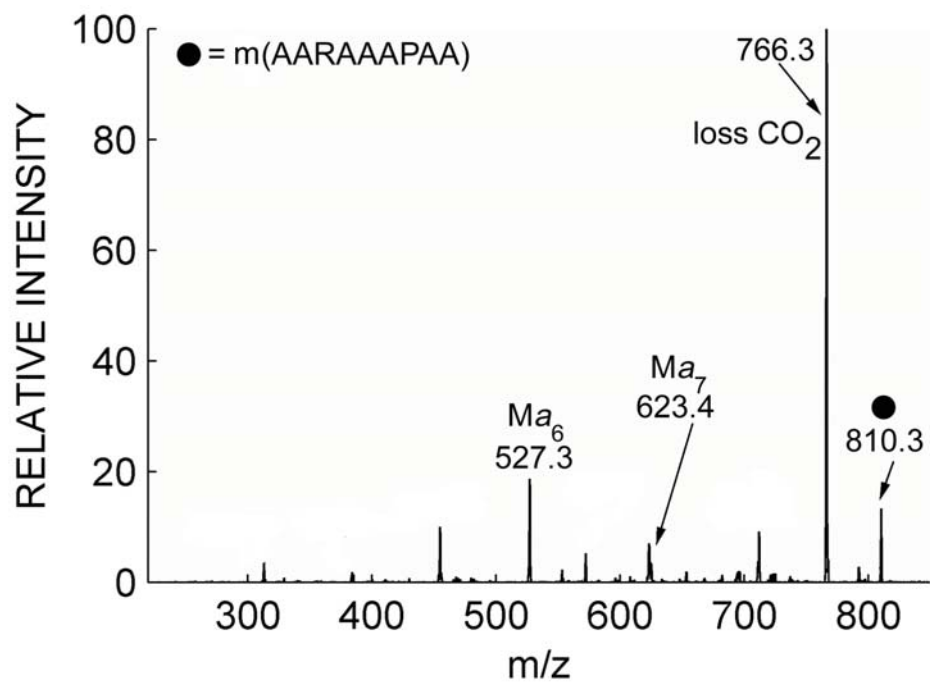


Figure 6.1: FRIPS spectrum of model peptide AARAAAPAA

FRIPS spectrum of the model peptide AARAAAPAA. Spectra for model peptides containing glycine and alanine are similar. The primary product is loss of 44 amu, which is assigned as loss of CO₂. Some *a* type fragmentation is also observed and may be a result of subsequent radical migration which will be discussed further in the text.

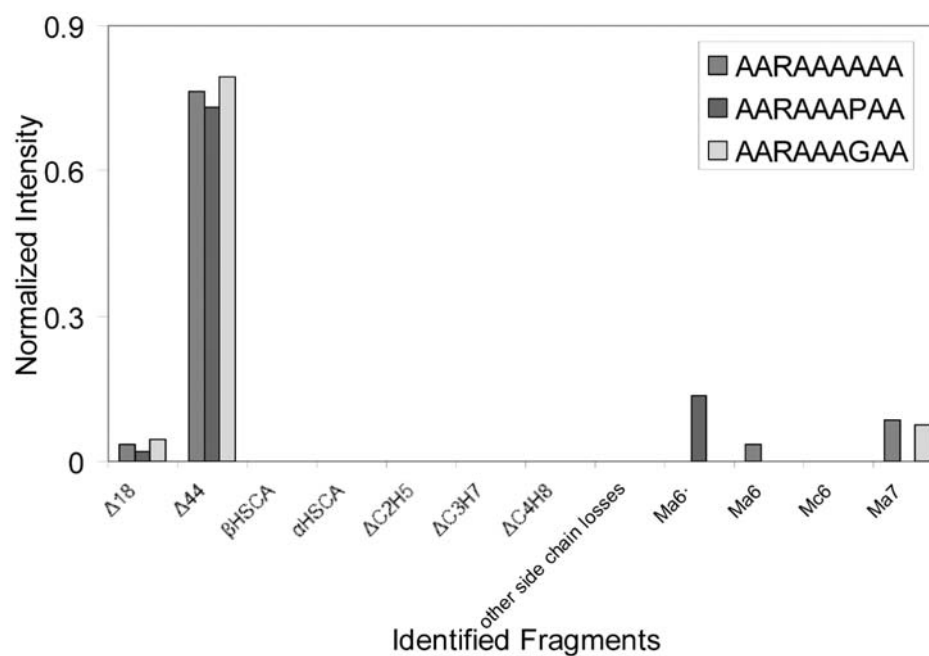


Figure 6.2: Bar graph showing relative intensities for residues losing 44 amu

Bar graph showing relative intensities for residues losing 44 amu. Glycine, alanine, and proline are included in this group. A slight preference for reaction at the X amino acid is observed for alanine, and the cause for this is under investigation.

does exist and is under investigation using molecular dynamics simulations to examine the possibility that contact between the acetyl radical and residues at the opposite end of the peptide are statistically more probable, and initial calculations have indicated this as a possibility.

6.3.2 Peptides containing residues X=D,N,H,Y,F,V,W

Site specific cleavage at the X residue site for the residues D, N, H, Y, F, V, and W in the model peptides was also observed. Figure 6.3 is the FRIPS spectrum for mAARAAAYAA, which is representative of reactivity of residues in this class. Primary fragments observed in the spectrum include Ma_7 and loss of CO_2 . Figure 6.4 gives relative abundances of the observed fragments. Fragmentation to form the Ma_7 fragment is thought to proceed *via* abstraction of the amino acid side chain β hydrogen, followed by β cleavage. Scheme 6.2 shows a possible fragmentation mechanism for this cleavage pattern as well as our convention for nomenclature of the hydrogens on a residue side chain. Assuming abstraction of the side chain β hydrogen, β cleavage on the C-terminal side of the amino acid gives the Ma_n fragment ion. The aromatic residues Y and F direct cleavage to the N-terminal side of the residue.

Since abstraction of the β hydrogen in a residue side chain appears to be the cause for fragmentation near the residue to form Ma_7 and other backbone fragments, the possible dependency on the bond dissociation energy for the $\beta H-C$ bond in each side chain on the degree of fragmentation was examined. A plot comparing the $\beta H-C$ bond energies for each residue in the class (data obtained from reference [84]) and the degree of reaction for each residue for the FRIPS experiment suggests a correlation. Degree of reaction was determined by comparing the sum of the relative abundances of the Mc_6 , $Ma_6\cdot$, and Ma_7 fragments with the relative abundance of the corresponding fragment where CO_2 loss was observed. The Mc_6 and $Ma_6\cdot$ fragments were considered because they also appear to arise from abstraction of a side chain hydrogen, which will be discussed in further detail below. Lower $\beta H-C$ bond energies appear to promote reaction, as was found with experiments using other radical sources [84].

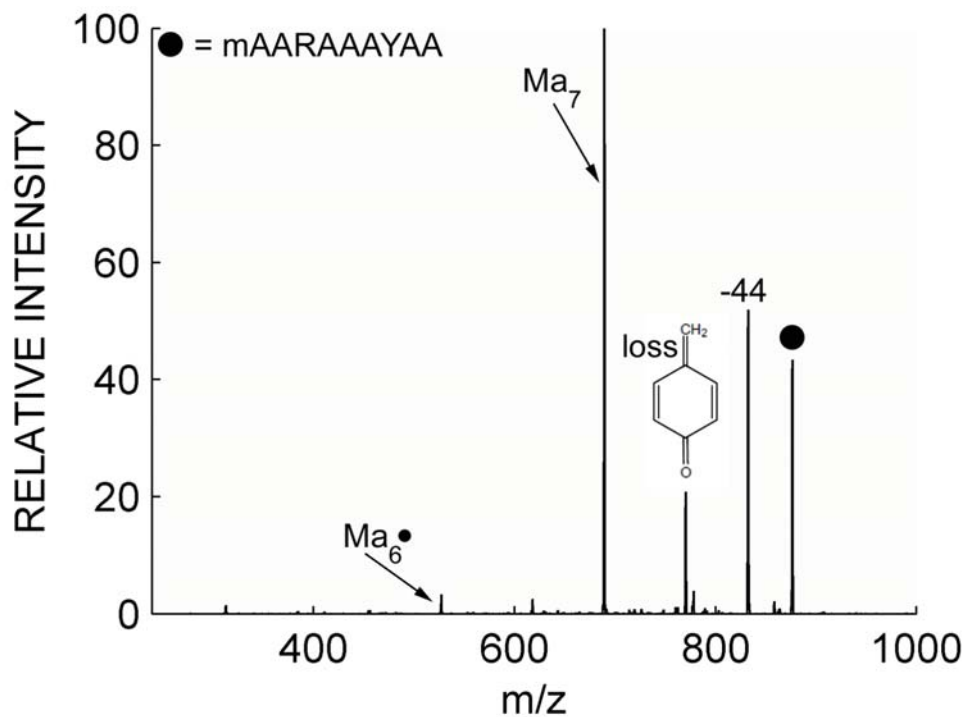


Figure 6.3: FRIPS spectrum of AARAAAYAA

FRIPS spectrum of model peptide containing $X=Y$. The primary fragment observed is the Ma_7 fragment, likely resultant from abstraction of hydrogen from the amino acid side chain. For tyrosine, loss of methide quinone (structure shown on plot) is also observed. Other residues in the class, including D, N, H, F, V, and W, react with acetyl radical in much the same way, through formation of a_7 fragments.

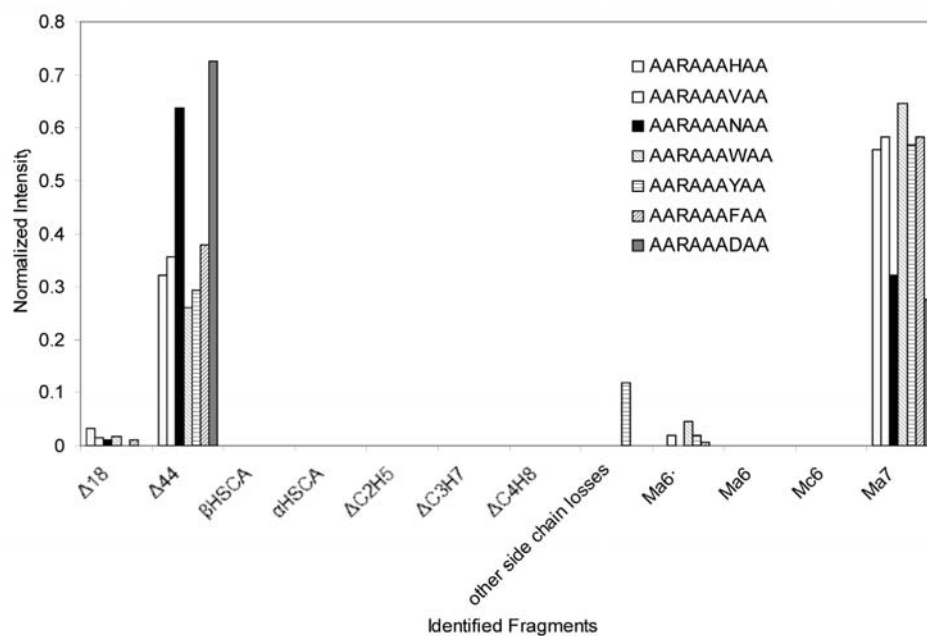
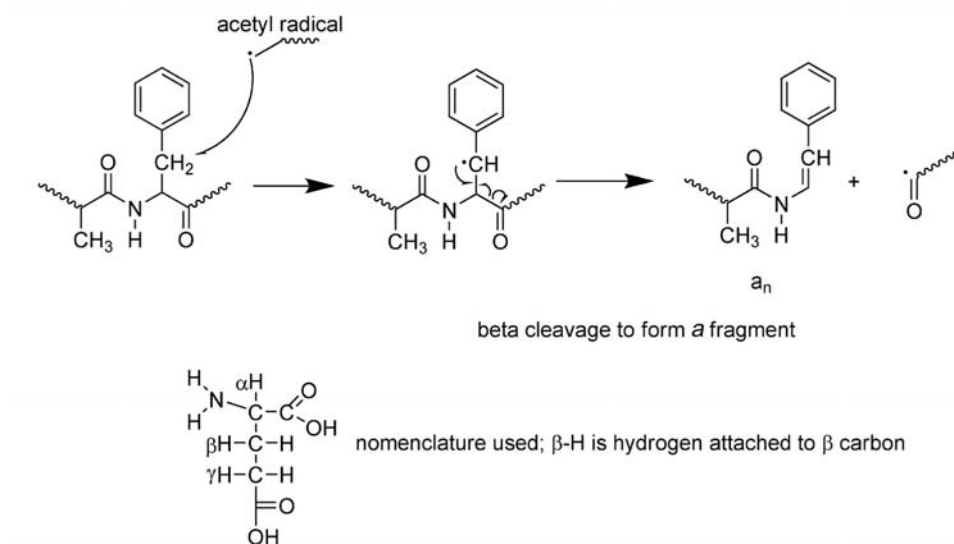


Figure 6.4: Chart showing relative abundances of products for those residues reacting to form Ma_7 fragments

Chart showing relative abundances of products for those residues reacting to form Ma_7 fragments. Specific reaction at the X amino acid residue is observed. Abstraction of hydrogen from the side chain followed by beta cleavage is thought to be the pathway for reaction with acetyl radical for each of these residues.



Scheme 6.2: Scheme for formation of Ma_n fragments by hydrogen abstraction followed by beta cleavage

Scheme for formation of Ma_n fragments by hydrogen abstraction followed by beta cleavage. Hydrogen abstraction from the amino acid side chain is effected by the acetyl radical, and beta cleavage follows. The mechanism shown here is for phenylalanine, a member of the class of amino acids exhibiting this reactivity and this scheme can be applied to any of the members of the class.

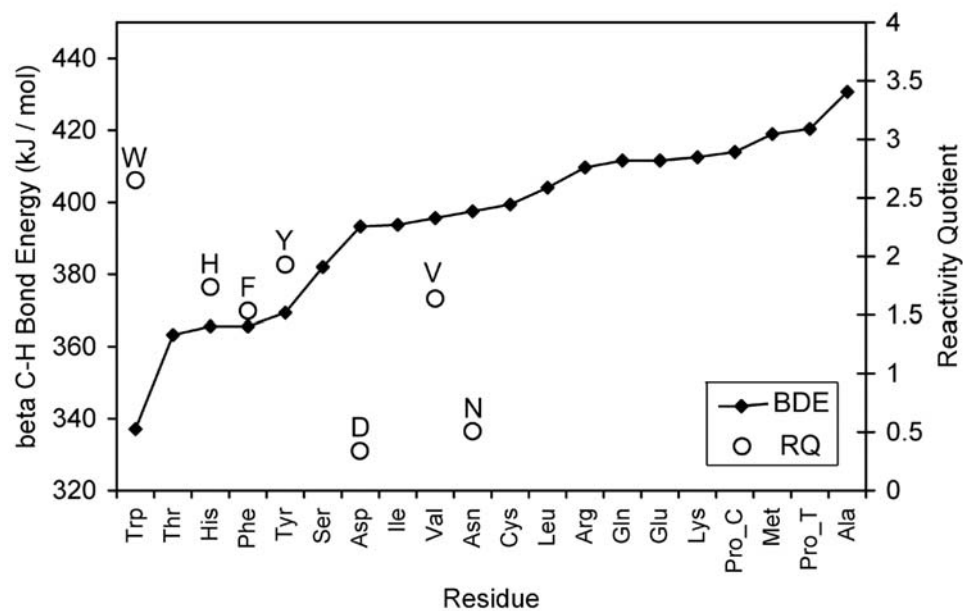


Figure 6.5: Correlation of β H-C bond dissociation energies with observed backbone fragmentation

A correlation is observed between the bond dissociation energy for the β H-C bond in each amino acid side chain and the degree of reaction of the radical moiety toward each residue site. Data for bond dissociation energies are taken from reference [84]. In general, lower β H-C bond energy appears to promote reaction.

6.3.3 Peptides containing residues X=S,T

Model peptides containing serine or threonine exhibited specific cleavage adjacent to the residue. Figure 6.6a shows the FRIPS spectrum of mAARAAASAA, while Figure 6.6b shows the FRIPS spectrum of mAARAAATAA. For mAARAAASAA, loss of CO₂ (-44) is observed, as well as a large fragment corresponding to $Ma_6\cdot$ and smaller fragments corresponding to Mc_6 , Ma_7 , and (to a smaller extent) Ma_3 . The majority of product fragments result from cleavage around the serine residue. For mAARAAATAA, a similar pattern of fragmentation is observed. If CO₂ loss is discounted, the peptides mAARAAASAA and mAARAAATAA fragment primarily into Mc_6 and $Ma_6\cdot$ ions. Scheme 6.3a is a scheme for formation of c ions following abstraction of hydrogen from the serine side chain. The subsequent formation of an aminoketyl radical intermediate which undergoes fragmentation to form the observed c ion is suspected. Formation of this radical and the subsequent fragmentation patterns forming c and z ions are identified in experiments by Moore and co-workers [86]. They also identify that although an aminoketyl type radical may be formed in many electron capture experiments (which have reactivity similar to free radical reactions) the result is not always c and z fragmentation because of the possibility of radical migration. Scheme 6.3b is a proposed mechanism for the formation of the observed $Ma_6\cdot$ fragment, which relies extensively on radical migration for the formation of the observed product. The observed neutral loss of HNC₂O directs suspicion of the proposed mechanism, which was developed based on considerations involving the formation of the observed fragments without extensive structural rearrangement.

6.3.4 Peptides containing residues X=K,Q,E,R,M,C,I,L

Other than peptide backbone fragmentation which include the formation of Ma_6 , $Ma_6\cdot$, and Ma_7 fragments, a final major class of reactivity are those residues exhibiting reaction primarily comprising losses from the amino acid side chains. These losses are attributed to either abstraction of α H or β H followed by subsequent neutral loss. Figure 6.7 gives relative abundances of species observed with side chain loss.

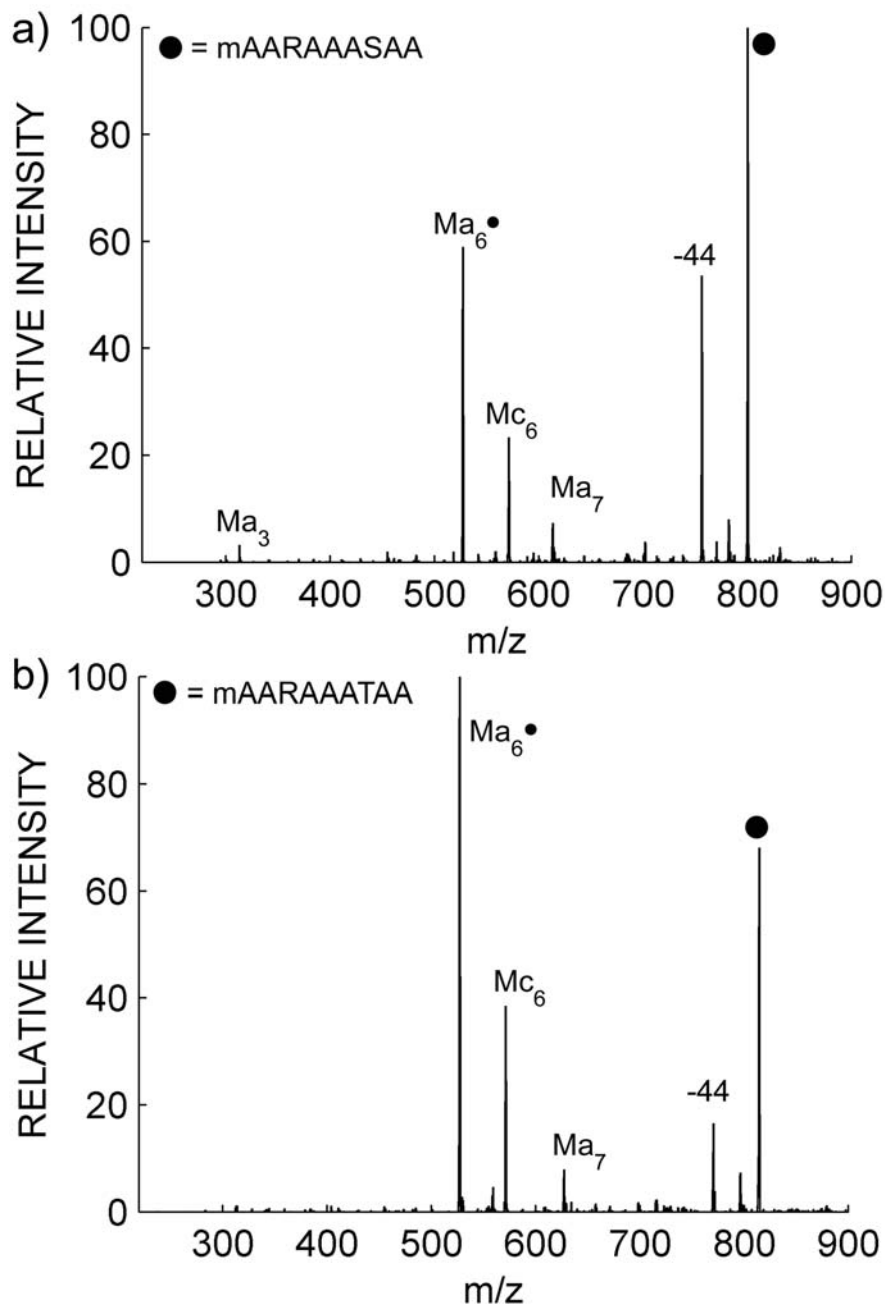


Figure 6.6: FRIPS spectra of AARAAASAA and AARAAATAA

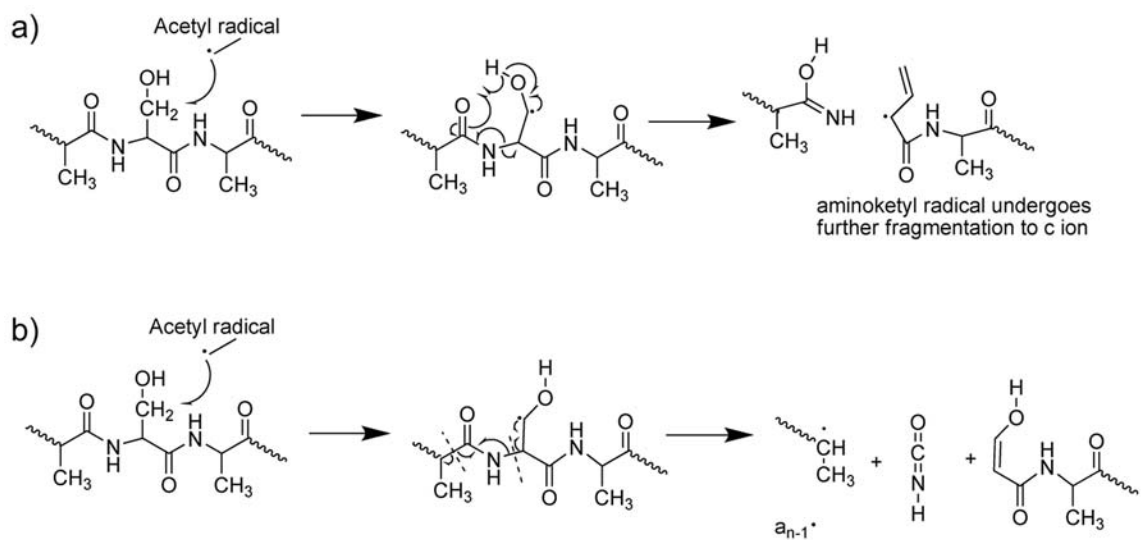
a) FRIPS spectrum of m(AARAAASAA). Directed fragmentation near the residue is observed, producing modified *a* and *c* fragments. b) FRIPS spectrum of m(AARAAATAA). Directed fragmentation near the residue is again observed, again producing modified *a* and *c* fragments. Taking the ratio of the peak heights for loss of CO₂ and formation of Ma₆ as a measure of reactivity, threonine is more reactive towards the acetyl radical than serine.

A fortuitous pattern of fragmentation is found for leucine and isoleucine residues. The side chain losses observed with leucine and isoleucine are distinct, allowing for the possible identification of these residues in sequence. Figure 6.8a is the FRIPS spectrum for mAARAAALAA, showing a distinctive loss of C_3H_7 while Figure 6.8b is the FRIPS spectrum for mAARAAAIAA, showing a distinctive loss of C_2H_5 . The predominant peak in the leucine peptide spectrum is due to the characteristic loss, while the primary fragment observed in the isoleucine peptide is the Ma_7 fragment. The differences can be understood with reference to Scheme 6.4. If the hydrogen abstracted by the radical portion of mAARAAALAA is the backbone α hydrogen of leucine, the reaction can proceed *via* β cleavage to lose C_3H_7 . Likewise, in the case of isoleucine, α hydrogen abstraction followed by β cleavage results in the loss of C_2H_5 . Different fragmentation results if a hydrogen is abstracted from the side chain of the amino acid. Formation of a tertiary radical requires abstraction at the γ hydrogen in leucine or the β hydrogen in isoleucine. Beta (β) fragmentation would then result in the loss of C_4H_8 for leucine or the formation of the Ma_7 fragment for isoleucine. These constitute the major fragment ions in both spectra shown in Figure 6.8. It appears that although both backbone and side chain hydrogens are abstracted from leucine or isoleucine residues, side chain abstraction is the preferred pathway.

6.4 Conclusion

Site-specific cleavage of peptides through collisional activation of free radical initiator-peptide conjugates was demonstrated. Specifically, of the group of model peptides of the general sequence AARAAAXAA where X was any one of the 20 commonly occurring amino acids, four distinct classes of reactivity were found. Peptides containing the residues G,A, or P exhibited only the loss of carbon dioxide as a significant product after reaction with the carbon centered radical. Peptides containing X=D,N,H,Y,F,V, or W exhibited the formation of the Ma_7 fragment as the major product, and this is a specific cleavage near the X residue which is likely due to abstraction of the side chain beta hydrogen, followed by beta cleavage. A small percentage of the Ma_6 fragment

was observed as well. Peptides exhibiting backbone cleavage to form primarily the Ma_6 included residues $X=S,T$ and this class can also be included with the previous as specific backbone cleavage. The last class of peptides containing $X=K,Q,E,R,M$ and C exhibit other side chain losses and do not exhibit specific peptide backbone cleavage. Although reaction with such residues may not be useful in peptide sequencing efforts, some of the specific losses observed could be useful for identification of the residues themselves. Leucine and isoleucine shown signature losses which are unique to these residues, which allow for the identification of which residue is in sequence in a peptide.



Scheme 6.3: Scheme for formation of c and a_6 fragments for serine, threonine

Proposed mechanisms for formation of c and $a_{n-1}\cdot$ fragments for serine. Mechanisms for threonine would be similar. a) Abstraction of hydrogen by acetyl radical forms an aminoketyl radical which can subsequently undergo fragmentation to form the observed c ions. b) Proposed mechanism for the formation of $a_n\cdot$ fragment relies on radical migration after hydrogen abstraction.

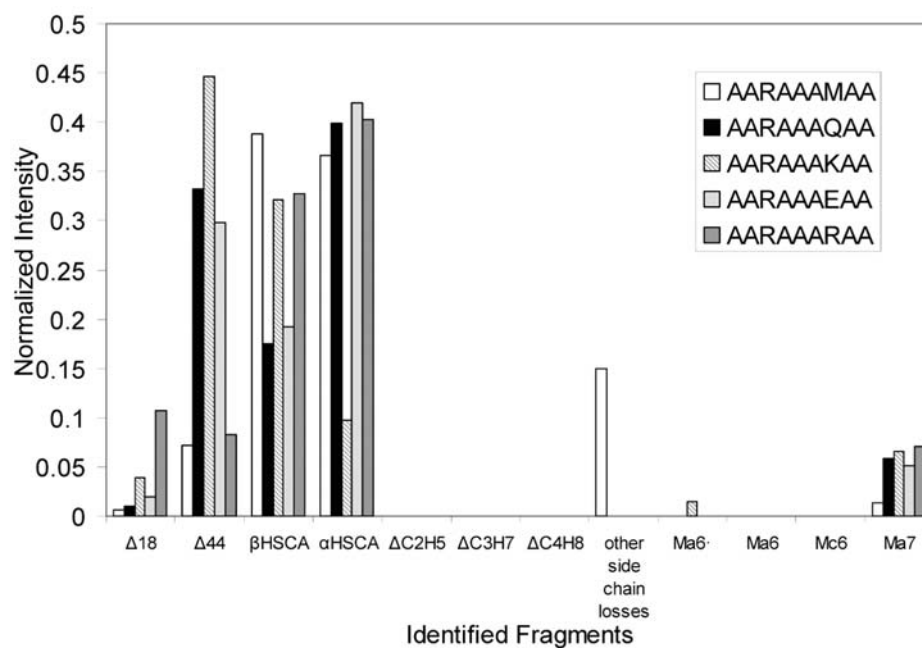


Figure 6.7: Graph showing relative abundances of products resulting from side chain losses in the Xth residue

Graph showing relative abundances of products resulting from side chain losses in the Xth residue. Each amino acid residue undergoes reaction with the acetyl radical with the end result being reaction with the amino acid side chain, and resultant fragments exhibit loss from the side chain.

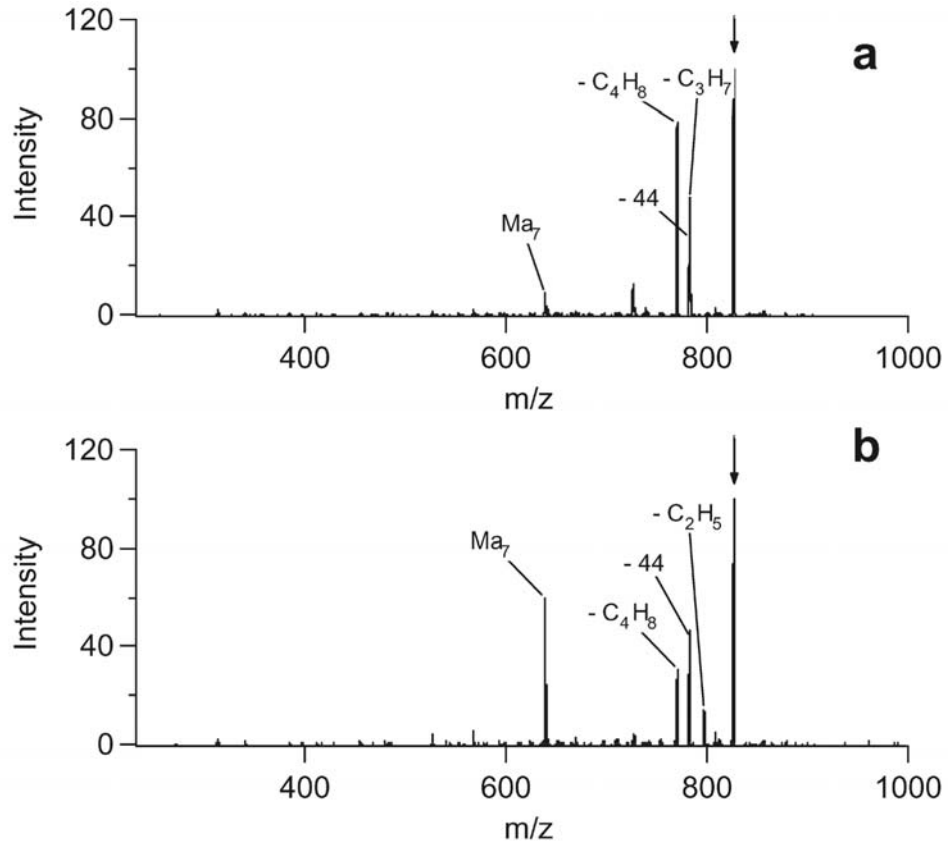
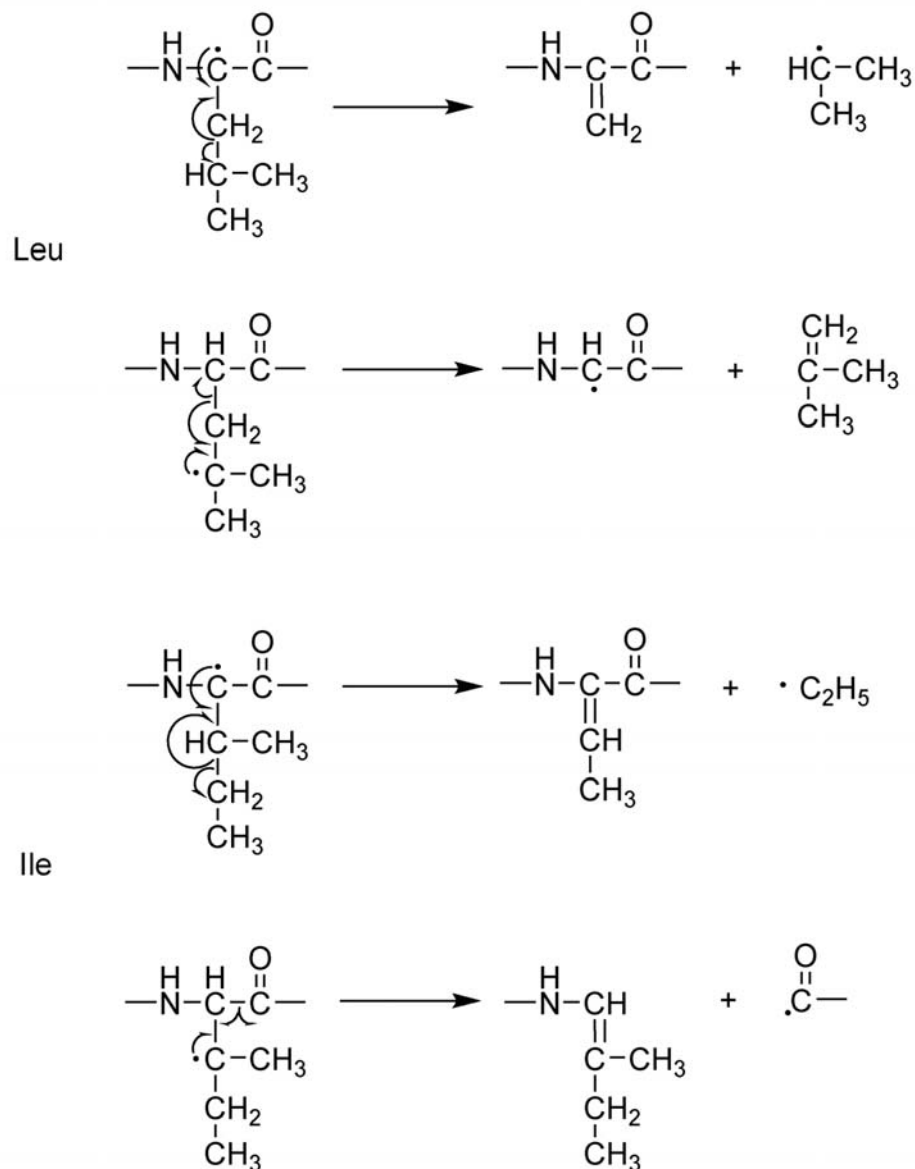


Figure 6.8: FRIPS spectra of AARAAALAA and AARAAAIAA

FRIPS spectra of AARAAALAA and AARAAAIAA. For each peptide, signature losses allowing the distinguishing of the isobaric residues are observed.



Scheme 6.4: Proposed mechanism for cleavage near isoleucine and leucine

Fragmentation mechanisms for cleavage around isoleucine and leucine. For isoleucine, the loss of ethyl radical is most easily explained through α hydrogen extraction, while the large Ma_7 peak is most naturally explained by formation of a tertiary radical on the isoleucine side chain. Leucine can lose C_3H_7 if the α hydrogen radical is abstracted, or C_4H_8 by forming a radical at the tertiary carbon on the side chain.

Peptide	$\Delta\text{H}_2\text{O}$	ΔCO_2	βHSCA	αHSCA	$\Delta\text{C}_2\text{H}_5$	$\Delta\text{C}_3\text{H}_7$	$\Delta\text{C}_4\text{H}_8$	S.C.	M_{a_6}	M_{a_6}	M_{c_6}	M_{a_7}
AARAAAGAA	4.4	79.4	-	-	-	-	-	-	-	-	-	7.9
AARAAAAAA	3.6	76.5	-	-	-	-	-	-	-	3.6	-	8.5
AARAAAPAA	1.9	73.1	-	-	-	-	-	-	13.6	-	-	-

Table 6.1: Relative abundances of products observed from activation of model peptides containing X=G,A,P

Peptide	$\Delta\text{H}_2\text{O}$	ΔCO_2	βHSCA	αHSCA	$\Delta\text{C}_2\text{H}_5$	$\Delta\text{C}_3\text{H}_7$	$\Delta\text{C}_4\text{H}_8$	S.C.	Ma_6	Mc_6	Ma_7
AARAAADAA	0.0	72.4	-	-	-	-	-	-	-	-	27.5
AARAAANAA	1.1	63.4	-	-	-	-	-	-	-	-	32.2
AARAAAHAA	3.2	32.2	-	-	-	-	-	-	-	-	55.9
AARAAAYAA	0.0	29.4	-	-	-	-	11.9	1.9	-	-	56.7
AARAAAFAA	1.1	38.0	-	-	-	-	-	0.74	-	-	58.3
AARAAAVAA	1.6	35.6	-	-	-	-	-	1.9	-	-	58.3
AARAAAWAA	1.8	26.1	-	-	-	-	-	4.7	-	-	64.6

Table 6.2: Relative abundances of products observed from activation of model peptides containing X=D,N,H,Y,F,V,W

Peptide	$\Delta\text{H}_2\text{O}$	ΔCO_2	βHSCA	αHSCA	$\Delta\text{C}_2\text{H}_5$	$\Delta\text{C}_3\text{H}_7$	$\Delta\text{C}_4\text{H}_8$	S.C.	Ma_6	Ma_6	Mc_6	Ma_7
AARAAAKAA	3.8	44.5	32.1	9.6	-	-	-	-	1.4	-	-	6.6
AARAAQAA	0.93	33.1	17.5	39.9	-	-	-	-	-	-	-	5.8
AARAAEAA	1.9	29.8	19.2	41.9	-	-	-	-	-	-	-	5.1
AARAAARA	10.7	8.2	32.7	40.2	-	-	-	-	-	-	-	7.0
AARAAAMA	0.61	7.2	38.8	36.6	-	-	-	15.0	-	-	-	1.3
AARAAACAA	0.37	7.9	-	-	-	-	-	91.7	-	-	-	-

Table 6.3: Relative abundances of products observed from activation of model peptides containing X=K,Q,E,R,M,C

Chapter 7

Regioselective Cleavage at Aspartic Acid Sites in Model Peptides

Protonated arginine, sodium cation, and guanidinium ion are shown to effect selective cleavage at aspartic acid sites in model peptides containing multiple aspartic acid residues. This energetically favorable process proceeds through a salt bridge intermediate, in which proton transfer from the aspartic acid side chain to the adjacent nitrogen precedes cleavage of the amide bond and formation of an acid anhydride. In the present study we investigate the regioselectivity of this process with the model peptides R(AAD)₅AA, (AAD)₅AAR, R(AAD)₅AAR, and (AAD)₅AA. Electrospray ionization is used to generate reactant ions which are isolated and subjected to collisional activation using an ion trap mass spectrometer. Peptides with attached arginine residues exhibit regioselective cleavage patterns at aspartic acid sites, dependent on the charge on the molecule and the position of arginine. Cleavage at aspartic acid by the mobile metal cation as well as the untethered guanidinium ion is less regioselective, exhibiting a slight preference for cleavage near the C-terminus of the peptide. The mobile cation preferentially forms an adduct with the larger of the two cleavage products.

7.1 Introduction

Tandem mass spectrometry (MS/MS) has become a ubiquitous technique in proteomics efforts. Database searching of peptide fragmentation data has allowed for

automated sequencing when the fragmentation induced by collisional activation produces fragments which are primarily those resulting from cleavage of the amide bond. Occasionally, extensive fragmentation is not observed but instead only one or two major fragments appear in the mass spectrum. Such selective fragmentation can often be used as a tool for probing specific amino acid residues, in both the gas phase and solution phase. In the solution phase, many transition metal complexes specifically hydrolyze the amide bond adjacent to certain amino acids. Platinum(II) complexes have been observed to effect selective cleavage near tryptophan residues [87], while palladium(II) complexes have been demonstrated to behave similarly near histidine [88] and serine [89] residues.

In the gas phase, several techniques for specific cleavage exist. In the previous chapter, the technique of free radical initiated peptide sequencing (FRIPS) was presented, whereby a radical initiator is covalently attached to the n-terminus of a peptide and through subsequent steps of collisional activation a carbon centered radical is formed which interacts with the various amino acid residues in the peptide. Specific fragmentation is observed in a number of situations, and the nature of the fragmentation observed is indicative of the residue of interaction. Many other gas phase cleavage techniques exist as well. Coordination with chromium(III) followed collisional activation of a peptide in the gas phase causes specific cleavage in acidic peptides [90]. For protonated peptides, some selective cleavage in the gas phase at histidine is readily observed [91] as well as lysine [92]. Of particular interest has been selective cleavage at acidic residues in protonated and metallated peptides. Energetics of cleavage at the acidic group sites [93] as well as selective cleavage in peptides containing glutamic [94] and aspartic acid [95] has been fairly thoroughly studied.

In this study, regioselective cleavage of the model peptide AADAADAADAAD-AADAA (from here forward abbreviated (AAD)₅AA) by protonated arginine, sodium, and guanidinium cation is studied, and compared to the non-selective cleavage observed from collisional activation of the singly charged peptide. The model peptides used are longer in sequence than those used in previous studies and should allow for determination of statistical distributions for cleavages in a longer peptide. For proto-

nated arginine and sodium cation, a salt bridge structure involving the aspartic acid side chain is cited as the primary mechanism for selective cleavage. For guanidinium cation, localization of the cleaving proton at the guanidinium group due to hydrogen bonding in much the same way as that for the arginine side chain results in cleavage.

7.2 Experimental

Mass spectrometry experiments were performed on a Thermo Scientific LCQ Deca XP ion trap mass spectrometer in positive ion mode. Relevant settings for the electrospray experiment were an inlet capillary voltage of 3.45 V and heated capillary temperature of 275 °C. The gas pressure inside the ion trap is approximately 10^{-3} Torr of helium. Analytes were isolated and fragmented using the typical collisional activation capabilities afforded by the instrument. To allow for the observation of lower mass fragments, a *q* value of 0.20 was used for the experiments. To the best of our knowledge, *m/z* dependent mass discrimination was not present. The mass spectra reported here are averages of 300 scans.

It should be noted that some modulation in apparent relative intensities can arise from fragments with neutral losses being isobaric with other fragments with no losses. For example, it may appear that the total amount of formed *b* ions and *y* ions are roughly the same, but the relative amount of *b* ions is in fact greater than that for the *y* ions. This is due to the fact that in a symmetric peptide *y* ions with water losses have the same mass as *b* ions, increasing the perceived amounts of *b* ions and decreasing the amount of *y* ions.

The peptides R(AAD)₅AA, (AAD)₅AAR, R(AAD)₅AAR, and (AAD)₅AA were purchased from Biomer Technology (Hayward, CA) at crude purity level (70% purity) and used without further purification. Model peptides were electrosprayed from a 1:1 mixture of water and methanol at concentrations in the 30 to 60 μ M range. For experiments with sodium cation, NaCl was added to the peptide solution at a concentration of 40 μ M. Guanidinium chloride was added to solution to achieve similar concentration levels for experiments with the guanidinium cation.

7.3 Results and Discussion

7.3.1 Cleavage of protonated (AAD)₅AA

The dissociation of protonated (AAD)₅AA upon collisional activation was studied to develop a baseline upon which to gauge fragmentation behavior of a peptide containing multiple aspartic acid residues. Because no basic residues are present to stabilize a positive charge, the (AAD)₅AA peptide is cleaved by a mobile proton. Cleavage occurs primarily toward the C-terminal end of the peptide, producing *b* ions corresponding to cleavage of amide bonds. Figure 7.1a is a full mass spectrum of the model peptide. Figure 7.1b is the spectrum resulting from collisional activation of the peptide in the ion trap. Figure 7.1c shows the relative intensities of each of the product ions where the ions are grouped on the plot according to the bond cleaved. This simplified form allows for comparison of ion intensities and evaluation of regiospecificity. The peptide readily cleaves amino acids from its C-terminal end with a preference for sites proximal to the C-terminus. The most common ion was the *b*₁₆ ion, a result of the loss of one alanine residue from the C-terminus. In general, regiospecific cleavage was not observed.

7.3.2 Cleavage of the peptide (AAD)₅AA with sodium cation

When metal cations such as Na⁺ are complexed to the model peptide, collisional activation induces dissociation of A–D bonds with a preference for sites near the C-terminus of the peptide. Figure 7.2a is the spectrum resulting from collisional activation of the model peptide complexed with sodium cation. Figure 7.2b is a plot showing the observed cleavage in terms of the bond that is broken. A salt bridge mechanism is suspected which promotes cleavage at the aspartic acid site, and Scheme 7.1a depicts cleavage with a salt bridge intermediate. After cleavage, the metal cation is free to associate with any energetically favorable site in the peptide, and a slight preference for association with the larger of the cleavage fragment is observed. It is suspected that favorable interactions between the peptide backbone and metal cation

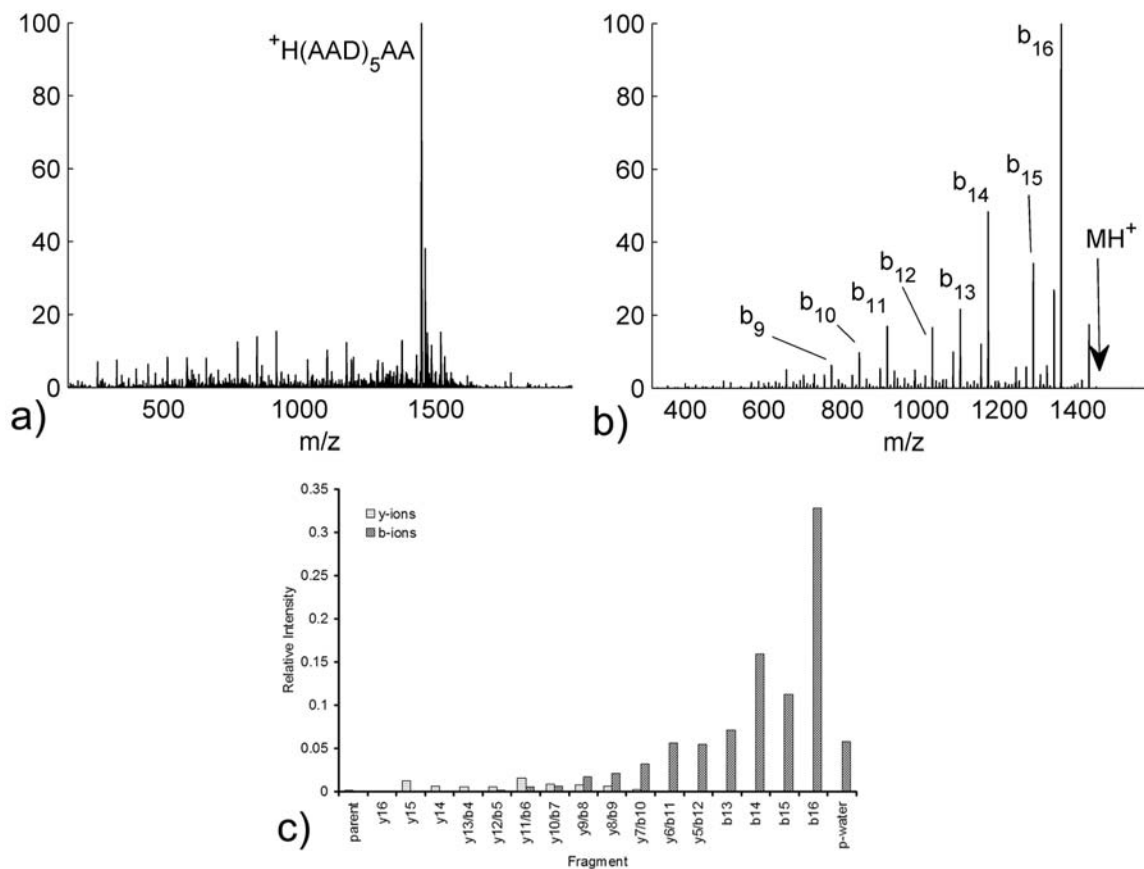


Figure 7.1: Mass spectrum and CAD spectrum of the peptide (AAD)₅AA

Mass spectrum and collisional activation spectrum of the peptide (AAD)₅AA. a) Full mass spectrum of the peptide (AAD)₅AA. The peptide is the major peak observed. Other small peaks in the spectrum are synthesis fragments present in the electrospray solution, owing to the fact that this peptide was purchased at a crude purity level. b) Collisional activation spectrum of the peptide from (a). A fairly typical pattern of *b* and *y* ion formation is observed. Backbone fragments most typically arise from collisional activation of a singly charged peptide. c) Bar graph showing relative abundances of each observed fragment. This type of plot will be used to better show regioselectivity in experiments that follow.

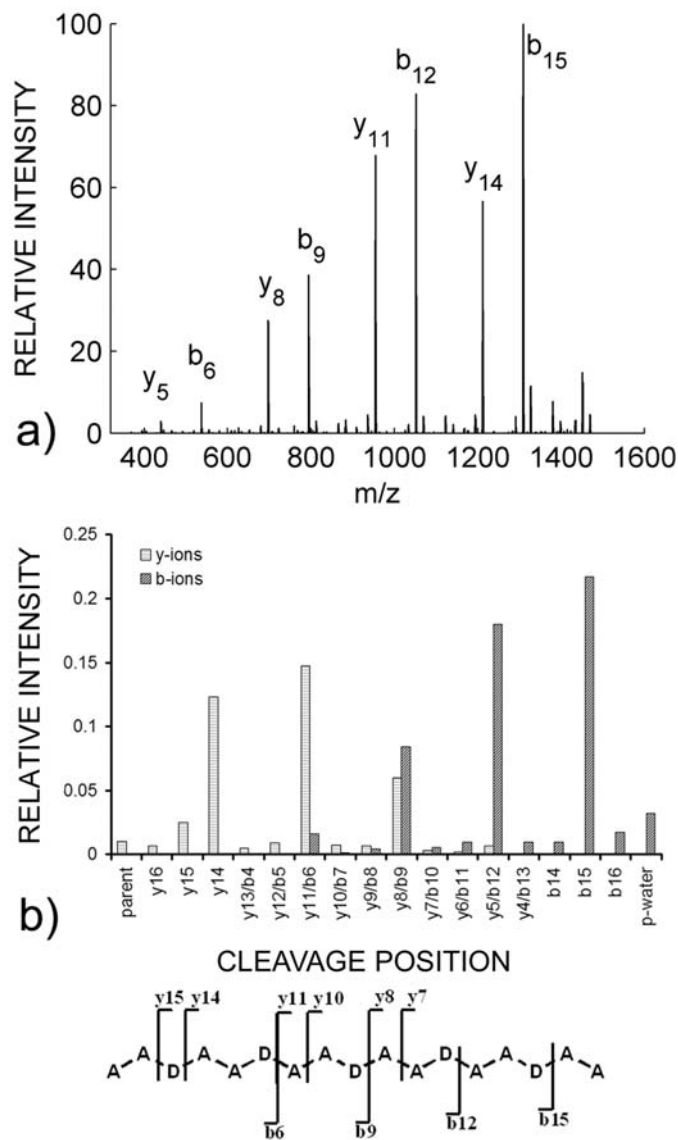
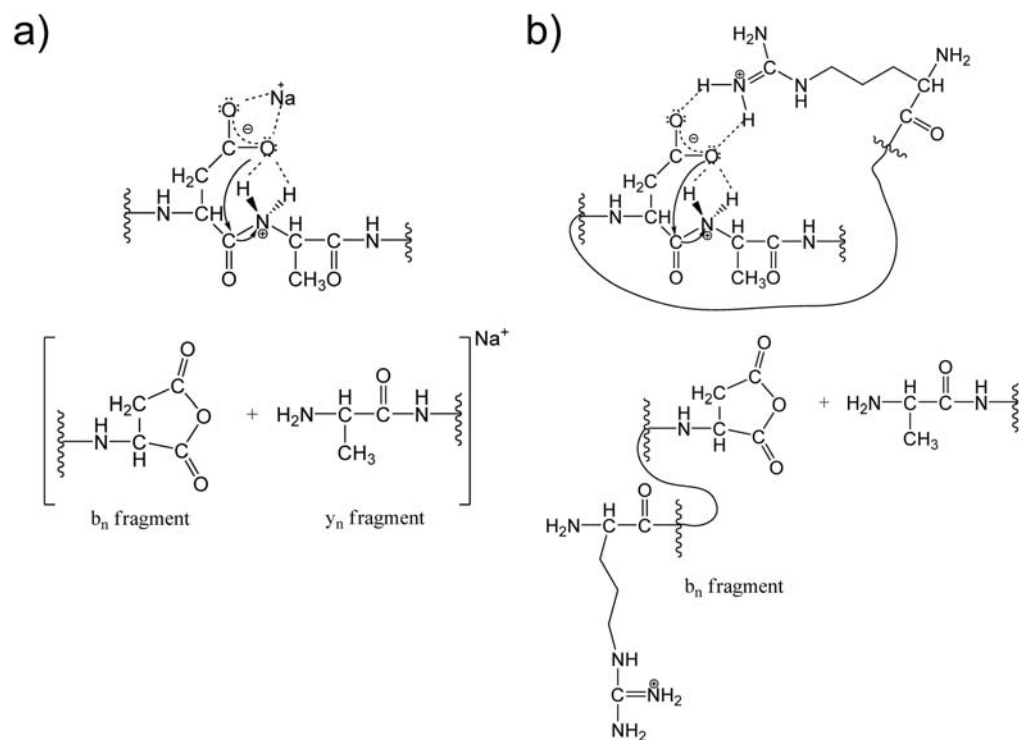


Figure 7.2: Cleavage of model peptide by sodium ion

Cleavage of model peptide by sodium ion. a) Collisional activation spectrum of the peptide (AAD)₅AA complexed with sodium cation. In contrast to experiments with protonated (AAD)₅AA, where non-specific backbone cleavage was observed, only cleavage near the aspartic acid residues was observed, indicating regioselectivity of cleavage. b) Bar graph emphasizing cleavage position. Only cleavage near aspartic acid sites was observed. No strong bias with respect to which aspartic acid was complexed was observed, however a slight preference for complexation near the c-terminus of the peptide was observed.



Scheme 7.1: Proposed mechanism for cleavage with a salt bridge intermediate for both sodium cation and protonated arginine

Proposed mechanism for cleavage with a salt bridge intermediate for both sodium cation and protonated arginine. a) Proposed mechanism for salt bridge formation and cleavage with sodium cation. Sodium cation associates with the deprotonated aspartic acid side chain, which has transferred a proton to the peptide backbone. Extensive hydrogen bonding between the peptide backbone and aspartic acid side chain facilitates stability and cleavage near the aspartic acid site, forming *b* and *y* ions. b) Proposed mechanism for complex formation and cleavage by the side chain of protonated arginine. Again, extensive hydrogen bonding between the protonated arginine side chain and the deprotonated aspartic acid side chain facilitates stability and complex formation, and subsequent cleavage to form *b* and *y* fragments.

are resultant in the observed preference with association with the larger fragment. The manifestation of this is the formation of y ions from cleavages before the midpoint of the peptide sequence and formation of b ions after the midpoint.

7.3.3 (AAD)₅AAR, R(AAD)₅AA,R(AAD)₅AAR

A study with model peptides containing the base sequence (AAD)₅AA and additionally having an arginine attached covalently to one or both ends was performed to examine cleavage by a proton associated with a basic site in the peptide. Figure 7.3a and b shows the MS/MS spectral data for collisional activation of protonated (AAD)₅AAR and R(AAD)₅AA. With protonated arginine on the C-terminus, only y ions are observed, whereas when the arginine is on the N-terminus of the peptide only b ions are observed because the arginine retains the charge after the cleavage. Scheme 7.1b depicts cleavage by protonated arginine. In the case of either peptide, ions are formed from specific cleavage at the C-terminal ends of the aspartic acid residues. Generally, sites three to four residues from the arginine residue are cleaved most often in the (AAD)₅AAR and R(AAD)₅AA peptides. The length of the arginine side chain is likely responsible for the regioselectivity of the position of cleavage. A significant fragment that was observed which does not fit with the primary distribution of cleavage sites occurs upon cleavage of the peptide (AAD)₅AAR where cleavage at the N-terminal end of the first aspartic acid residue produces the y_{16} ion instead of the expected corresponding b ion. This result is due to the competition of two effects: the attraction of the mobile proton to the base and its attraction to the backbone of the larger peptide fragment, which has multiple sites on which to solvate the proton.

The peptide R(AAD)₅AAR was examined in both the singly and doubly charged states. In the case of the singly charged peptide, primarily y_{17} , y_{18} , and b and y ions resulting from specific cleavage at the C-terminal ends of the aspartic acid residues are formed. Figure 7.4a shows this result. Formation of y ions is more prominent at the first three aspartic acid residues, while the b ions prevail at the fourth and fifth aspartic acid sites. For the singly charged peptide, the ionizing proton could

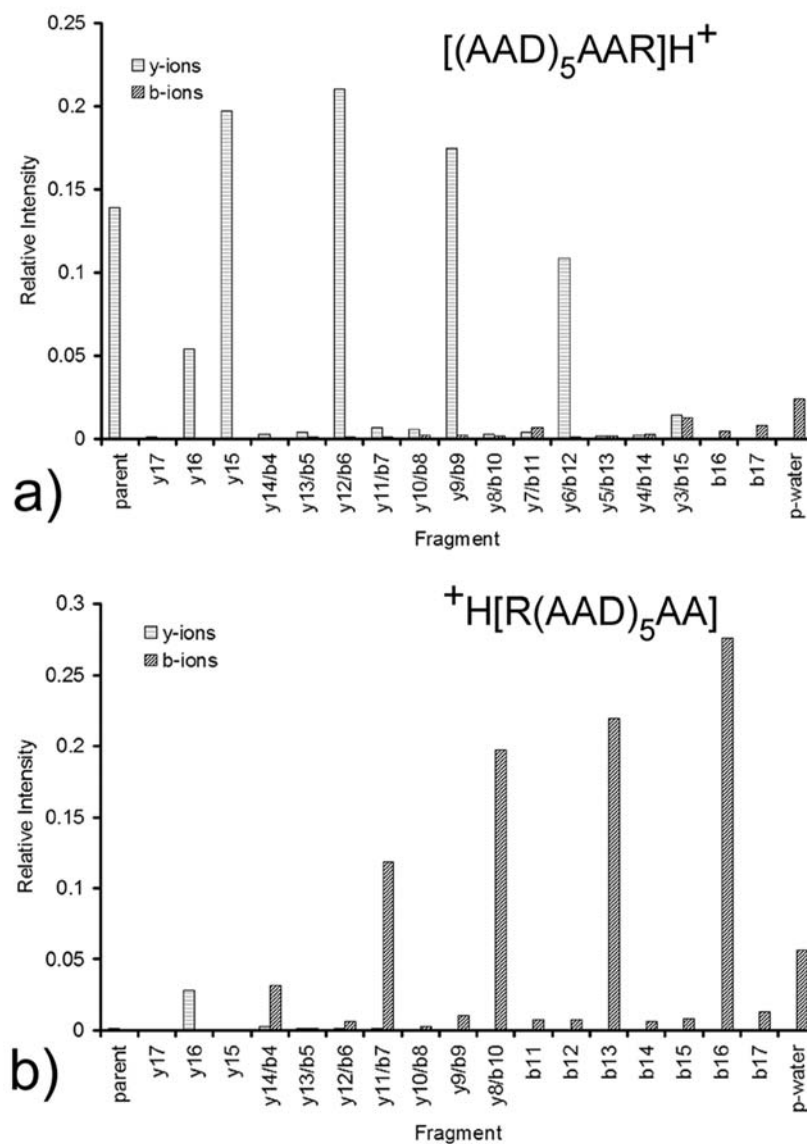


Figure 7.3: Cleavage of protonated model peptide with arginine on either terminal end

Cleavage of protonated model peptide with arginine on either terminal end. a) With arginine at the end of the amino acid sequence, *y* fragments are observed corresponding with selective cleavage at aspartic acid residues in the peptide. Reaction toward the end of the peptide opposite the arginine residue is observed, and this is to be expected owing to steric concerns; a less strained intermediate state is expected for complexing the first aspartic acid, while complexing the aspartic acid closest to the arginine would likely result in a very strained intermediate. b) With arginine at the beginning of the amino acid sequence, *b* fragments are observed corresponding with selective cleavage at aspartic acid residues in the peptide. Again, reaction with aspartic acid residues more distant from the arginine is observed.

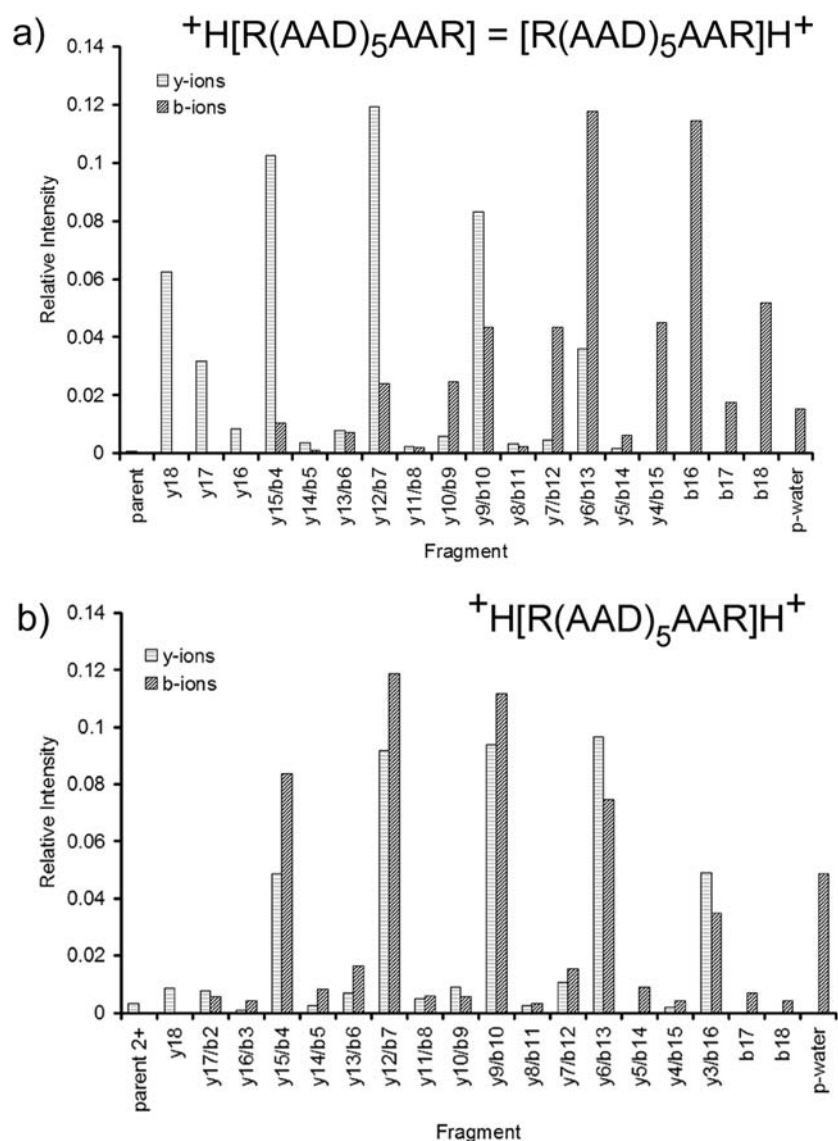


Figure 7.4: Cleavage of singly and doubly charged R(AAD)₅AAR

Cleavage of singly and doubly charged R(AAD)₅AAR. a) Cleavage observed for the singly charged peptide. Determining which arginine was charged is not possible because the singly charged peptide would have the same mass in either case. If the n-terminal arginine is charged, it would be expected that primarily *b* ions be observed; if the c-terminal arginine is charged, it would be expected that primarily *y* ions be observed, in accordance with previous experiments. This is the case, and the bar graph in a) is essentially the sum of the results from Figure 7.3 a and b. b) Cleavage observed for the doubly charged peptide. A trend toward cleavage near the middle of the peptide is observed, likely due to charge repulsion of the protonated arginines.

be sequestered at either basic site with equal probability. The type of ion formed, either y or b , is determined by which arginine was charged, and thus involved in the cleavage. As a result, the same y ion fragmentation pattern as in the (AAD)₅AAR peptide and the same b ion fragmentation pattern as in the R(AAD)₅AA appear in the singly charged R(AAD)₅AAR spectrum. Overall, cleavage occurs with nearly equal probability at each aspartic acid residue, and the total peak intensity of b ions and y ions formed are approximately equal, as would be expected if combining the two spectral series from the peptide containing a single arginine.

When the number of ionizing protons is the same as the number of arginines, for the $[M+2H]^{2+}$ case, selective cleavage on the C-terminal side of aspartic acids is the only fragmentation pattern observed. Figure 7.4b shows this result. Each arginine will retain its charge after fragmentation, and thus both b and y ions are formed with each cleavage. Cleavage near the center of the peptide, at the second, third, and fourth residues, is favored due to the apparent repulsion of the positively charged guanidinium groups on the arginine residues, inhibiting the likelihood of them coming close together to induce cleavage near a terminal end of the peptide.

7.3.4 Cleavage of the peptide (AAD)₅AA by the guanidinium ion

The guanidinium ion was also investigated as an ionic, non-covalent cleaver that has similar properties to the arginine side-chain. Similarly to the metal cation, it is mobile; however, it can form hydrogen bonds with the acidic residues analogous to the arginine side chain and effect cleavage in much the same way. Similar to Scheme 7.1b, Scheme 7.2 depicts complexation and cleavage by the guanidinium cation. The MS/MS spectrum of $[M + CH_6N_3]^+$ is shown in Figure 7.5a and the bond cleavage position plot is shown in Figure 7.5b. The spectrum is very similar to the spectrum of the sodiated complex in that there is a preference for cleaving at acidic sites near the C-terminus and y ions are formed by cleavages before the midpoint of the molecule while b ions are formed from cleavages after the midpoint.

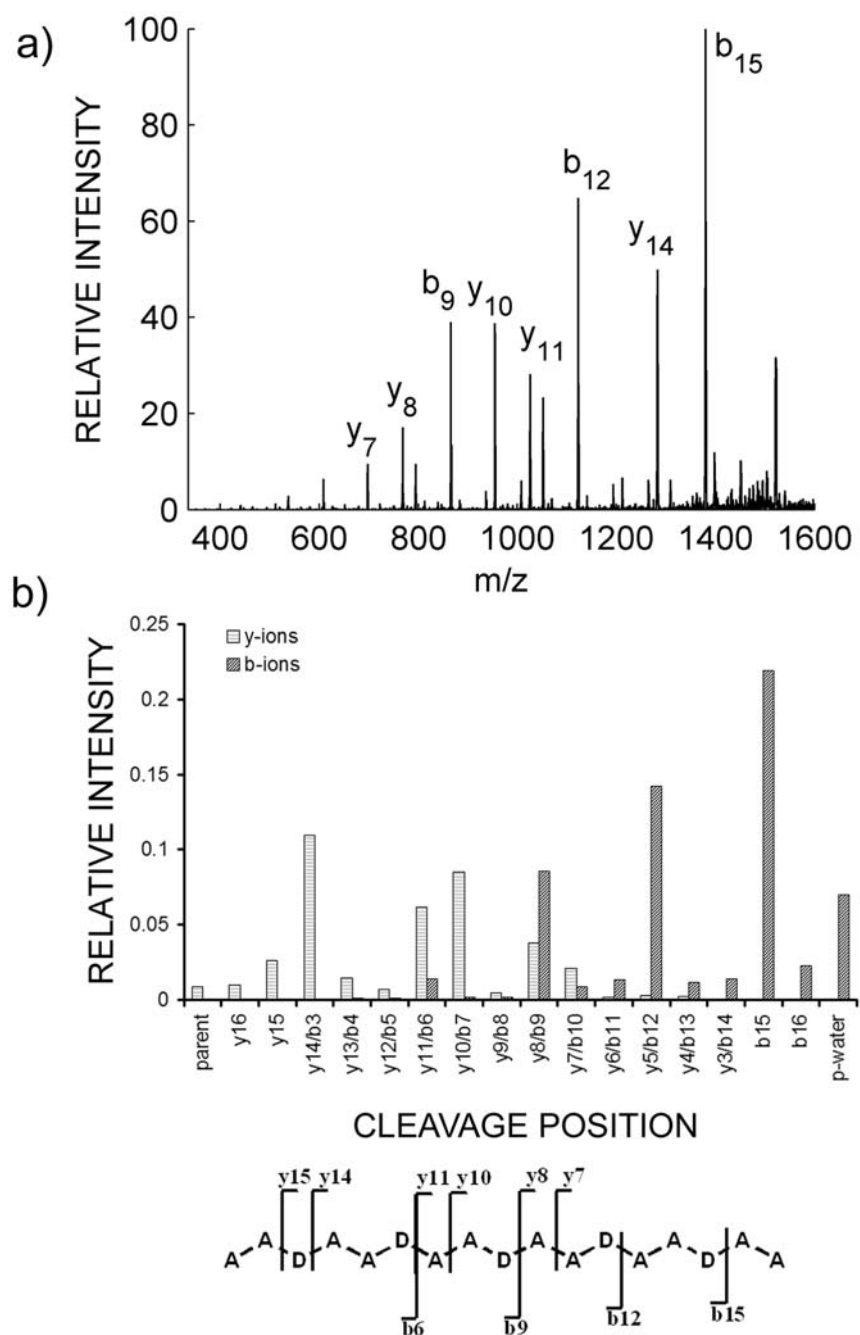


Figure 7.5: Cleavage of model peptide by guanidinium cation

Cleavage of model peptide by guanidinium cation. Regioselective cleavage is observed at aspartic acid sites, proceeding according to Scheme 7.2. Hydrogen bonding between guanidinium ion and the deprotonated arginine side chain forms a stable complex, which can undergo peptide backbone fragmentation upon collisional activation.

For this complex, the appearance of the y_{10} ion was unexpected. It is believed that cleavage at this location is due to the interaction of the guanidinium ion with multiple acidic residues at once. Location of the guanidinium ion between two acid residues, as if the two acids were acting as a bidentate ligand for guanidinium, appears to induce cleavage in a position along the peptide backbone between the two acid residues.

7.4 Conclusion

Peptides with attached arginine residues exhibit regioselective cleavage patterns at acidic sites, dependent on the charge on the molecule and the position of the arginine. Cleavage at aspartic acid by the mobile metal cations as well as the untethered guanidinium ion is less regioselective, exhibiting a slight preference for cleavage near the C-terminus of the peptide. The mobile cation preferentially aggregates with the larger of the two cleavage products. Peptides and possibly proteins containing acidic residues can be broken down into smaller units by the specific cleavages effected by arginine residues, metal cations, or guanidinium ions. The sequence of each smaller unit can be determined by further collisional activation, allowing top-down sequencing of the entire peptide or protein to be accomplished in the gas phase.

Appendix A

Electronics and Experimental Designs for Improved Operation of SwiFerr and APPIS

APPIS and SwiFerr have proven to be simple yet robust and versatile ion sources for ambient mass spectrometry experiments. Applications where CBW agents, explosives, and neat powders were sampled have been demonstrated and the sources show good sensitivity and signal-to-noise ratios in each experiment. Previously, the rate of discharge was a limiting factor in ion signal observed in the mass spectrometer. The next steps in the development of APPIS and SwiFerr will be presented here. First, an embodiment of APPIS having a properly configured grounded grid attached to the $-z$ crystal face will be proposed. It is known that electron emission occurs from the surface of pyroelectric materials when the crystal face has a high negative potential due to temperature cycling. If the source were configured similarly to SwiFerr with respect to the grid arrangement, additional discharging could be promoted and increased sensitivity in negative mode operation could be achieved. For SwiFerr, a study on the timescale of discharge on each switching cycle was performed. It was found previously that the capacitative nature of SwiFerr dictates operation at the lowest possible frequency if minimization of power consumption is the goal (that is, increased operational efficiency). A pitfall of this approach is not achieving the proper duty cycle for the instrument being used, and the appearance of not producing any ions for analysis. Presented here is a proposed method for the operation of SwiFerr

in a ‘constant discharge’ mode, whereby either three crystals or one crystal divided into three sections is employed. By applying the correct phase-locked waveform to the crystals or crystal sections, a discharge (and thereby reagent ion production) occurs at every point in time in spite of the operation of a single crystal being non-continuous. A benefit of this operational mode is reduced power consumption by the ion source itself because of reduced operational frequency, making the drive electronics the limiting factor in miniaturization and portability efforts. To this end, a preliminary design for drive electronics for both the single crystal and tri-mode SwiFerr are presented.

A.1 Introduction

Continued development of the APPIS and SwiFerr ion sources should yield devices which operate more efficiently and are more useful in future studies. For APPIS, a particular concern is the rate of production of ions from the source. The short discharges encountered in the APPIS source mean that ions are produced in discrete packets, and the source is by no means continuous. This has been a problem in the past, for example in experiments where the APPIS source is intended as the front end ion source for differential mobility spectrometry (DMS) experiments [96],[97]. Efforts to integrate APPIS with DMS have been undertaken, and the rate of ion production was found to be a particular limitation. For SwiFerr, it was also found that the discharge and ion production was not continuous, and it is expected that this may be a problem when attempting to integrate the source with detectors other than ion trap mass spectrometers.

A scheme whereby the ion production rate for APPIS is increased by taking advantage of the electron emission properties of the pyroelectric materials is presented. A grounded grid should be attached to the face of the pyroelectric crystal in the APPIS source which, when negatively charged, will undergo electron emission and plasma formation between the crystal face and grid. Also, a scheme for a continuous discharge mode for SwiFerr will be presented. A three-phase excitation scheme is proposed which, when used in conjunction with a source containing three crystals,

or a single crystal divided into three sections, will give an effectively continuous discharge from the point of view of the detector. This should allow for simpler and more facile integration of the SwiFerr source into field portable instrumentation of many kinds. Schematics for the drive circuits for both standard operation of SwiFerr as well as the three-phase mode are also presented and comprise circuits obtained from the literature and applied in a unique way so as to operate the SwiFerr source in its various modes.

A.2 Experimental

A.2.1 Design and construction of drift cell

An ion drift cell was constructed which would allow for the study of ion production from the APPIS ionizer. The drift cell comprises 5 plates with 1.25" holes, spaced 0.300" apart and connected with a string of 1 M Ω resistors. Figure A.1 is a schematic and photograph of that drift cell. The detector plate, in between the last two drift rings, was connected through a Keithley 485 autoranging picoammeter or a home-built transimpedance amplifier for detection of ion current. Sampling rate for the Keithley was 125 Hz; for the transimpedance amplifier, sampling rate varied between 2 and 5 kHz. The temperature of the crystal was varied using a Thorlabs TC200 temperature controller and 16W cartridge heater. Ion current data were collected for approximately 1–2 minutes, and subsets of those data were examined and averaged to establish a statistically significant ion production rate.

A.3 Results and Discussion

A.3.1 Rate of ion production with APPIS; Increasing rate with appropriate grid

Figure A.2 is a plot relating heating rate of the crystal to the average observed ion production rate. Goodness of fit of the trend line, along with analysis of the data

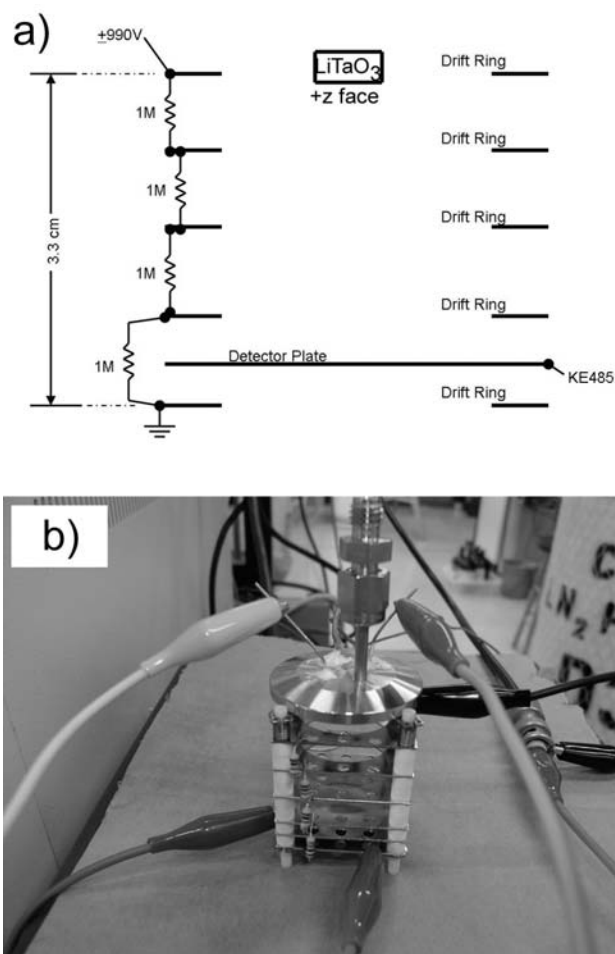


Figure A.1: Schematic and photo of drift cell

a) Schematic of the constructed drift cell. The cell comprises five drift rings that are of 1.25" (32 mm) inner diameter, separated by 0.300" (7.6 mm). A detector plate is located between the last two drift rings, and is backed by ground potential. Ions created in the space between the first and second rings encounter an electric field of approximately 300 V/cm and travel toward the detector plate. Both a negative and positive high voltage potential can be applied to the cell to analyze negative and positive ions, respectively. Current on the detector plate is analyzed using either a Keithley 485 autoranging picoammeter or a home-built transimpedance amplifier. b) Photograph of the drift cell.

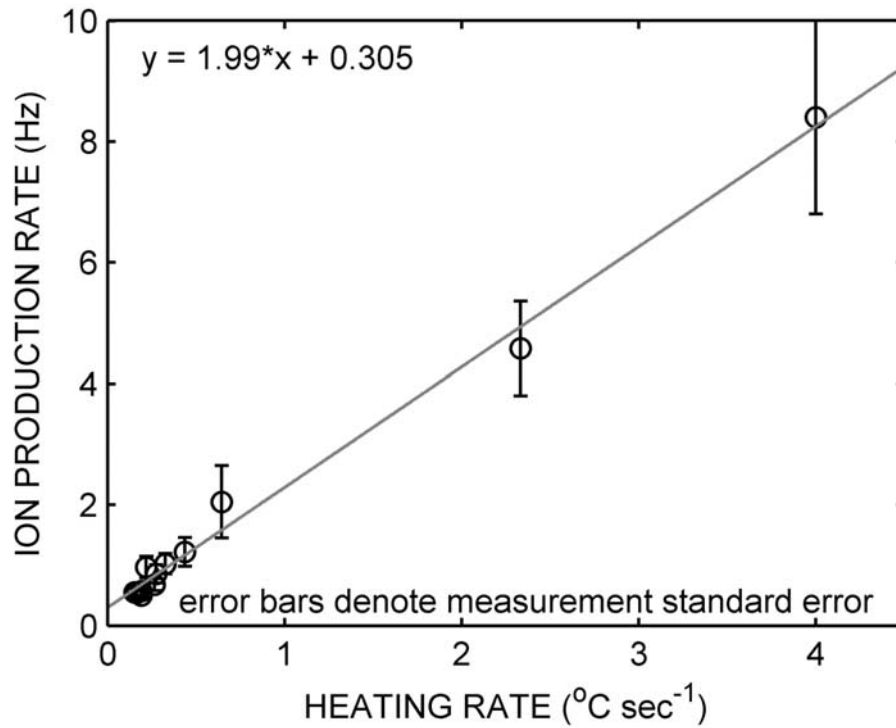


Figure A.2: Plot relating heating rate to ion production for a pyroelectric crystal

Plot relating heating rate to ion production for a pyroelectric crystal. Ion production rate increases in a linear fashion with crystal heating rate in the current embodiment. Most experiments use a heating rate between 0.5 and 2 °C per second, giving ion production rates in the 1 to 4 events per second range.

residuals indicate that a linear fit is appropriate for the data collected. The end of this chapter contains statistical methods used to construct the plot. The correlation between crystal heating rate and ion production rate for the tested crystal is a 2 Hz increase in ion production for every degree Celsius per second increase in heating. The power needed to raise the temperature of the crystal a certain amount is given by Equation A.1, where C_p is the specific heat of lithium tantalate ($0.06 \text{ cal (g } ^\circ\text{C)}^{-1}$), ρ is the density of lithium tantalate (7.45 g cm^{-3}), V is crystal volume, and r is the rate of heating.

$$P = C_p \rho V r \quad (\text{A.1})$$

The amount of power required to change the crystal temperature for a heating rate of 1 Kelvin/second is 187 mW, under ideal heating conditions (assuming no heat lost). This corresponds to an approximate 2 Hz ion production rate for the current implementation. It can be seen that achieving an ion production in the hundreds of ion events per second becomes prohibitive from a power budget point of view; producing 100 ion events per second (requiring a heating rate of 50 Kelvin/second will require 9.3 W of power.

Taking advantage of the electron emission properties of the pyroelectric materials should allow for an increased ion production rate. A way to achieve this is to incorporate a grounded grid onto the $-z$ face of the pyroelectric crystal, so that when the crystal is cooling electron emission occurs and a plasma is formed between the crystal face and grid, in much the same way as with SwiFerr. The new embodiment could be constructed just as easily to function as the crystal is heated by placing the grid on the $+z$ face, which becomes negatively charged upon heating. A higher ion production rate is expected with the grid due to the decreased distance between the crystal face and the grounded grid and a corresponding increase in electric field strength. The increased electric field coupled with electron emission from a negatively charged face should have an increased ion production rate as the end result.

A proper implementation of the grid is critical. The revised source would have a

TEM grid (same as used in Chapter 5) affixed to the pyroelectric crystal face using electrically conductive epoxy. A wire should also be attached to the crystal face and grid and connected to ground. Once constructed, a plasma similar to that in the SwiFerr source should arise whenever the crystal face is negatively charged. It is unknown if a plasma will arise when the face is positively charged, as the timescale of charge buildup and polarization change is very different in the pyroelectric and ferroelectric experiments. In the ferroelectric case, domain formation and polarization switching give rise to high electric field across domain walls which results in electron emission, and this occurs on both negative and positive voltage swings. In the pyroelectric case, charge buildup in the surface layers of the material is responsible for the electric fields necessary to promote electron emission, and this occurs only when the face becomes negatively charged. Lastly, consideration for ion extraction either by ion optics or transport in gas is critical, since it is expected that there will be a reduced electric field between the crystal face and capillary inlet which usually aids in transport of the ions into the mass spectrometer.

A.3.2 Operation of SwiFerr using a ‘stand alone’ power supply

Currently, a high voltage amplifier/generator is used to supply a sinusoidal AC waveform to the SwiFerr source. The specific unit used is rather cumbersome and while ideal for testing purposes, is too complicated and not portable enough for the day-to-day operation of SwiFerr. A ‘stand alone’ power supply for the source has been constructed, but is currently not in use owing to an operational mode not previously appreciated. The stand alone supply utilizes a high voltage generator intended for use with plasma generators (MINIMAX2, Information Unlimited, Amherst, NH, USA). While the stand alone supply was completely functional, the output waveform was of a frequency of approximately 50 kHz which in later study was realized to excessively excite the source capacitance and was a source of waste heat. A properly designed supply would have a frequency of approximately 1 kHz in the appropriate voltage

level. Several high voltage generators and amplifiers much simpler than the current TREK supply used are also available from TREK, but none fit the need of being portable or being easy to integrate into field portable instrumentation. The design of an appropriate drive circuit is thus desirable.

Below, a design for a power supply for the SwiFerr source which operates in the proper voltage and frequency range will be presented. Figure A.3 is a schematic of the proposed supply. A waveform generated from a unique oscillator [98] is supplied to a high voltage amplifier [99], which amplifies the voltage from the oscillator and applies this voltage to the rear electrode of the crystal. Frequency of oscillation is adjusted by adjusting the value of the capacitor. Output voltage can be set at 900 V pk-pk (318 V RMS) and this is sufficient to operate both the first and second generation SwiFerr sources. The current state of electronics packaging and printed circuit board manufacture should enable the easy construction of this circuit for future use so that the SwiFerr source is portable between different laboratories.

A.3.3 Timescale of discharge with SwiFerr; Constant discharge mode SwiFerr

A study of the time scale of plasma formation for SwiFerr was performed. Since plasma formation is due to polarization switching and domain wall formation, and such switching has a finite time scale, it cannot be the case that a constant discharge is present. An arrangement as depicted in Figure A.4 was employed to study the plasma formed between the crystal face and grid. Voltage across the resistor is a result of current flowing between the grid and ground. It was found that a discharge of finite length occurs during the positive voltage swing, and one occurs during the negative voltage swing. The width of this discharge period scales with frequency. Figure A.5a shows the waveform and discharge at a frequency of 1.5 Hz. The discharge is approximately 1/4 of the excitation cycle in length. Figure A.5b shows the excitation and discharge at a frequency of 2.5 kHz. Again, the discharge is of finite width and approximately 1/4 of the excitation wave in length. Also, two discharges

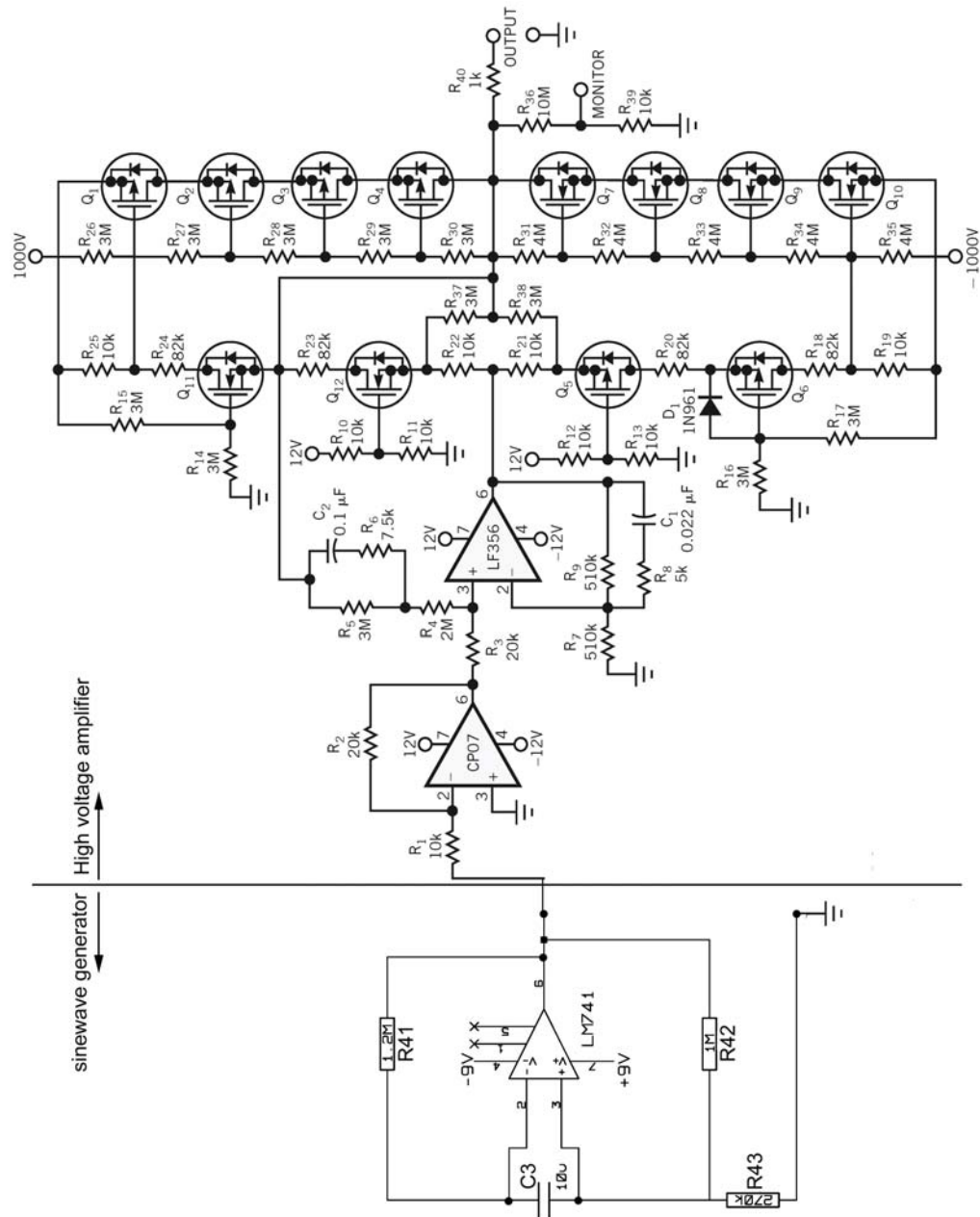


Figure A.3: Schematic for a stand-alone power supply for SwiFerr

Schematic for a power supply which operates the SwiFerr source apart from the bench top power supply that is currently used. A unique oscillator supplies a sinusoidal waveform to a high voltage amplifier circuit, the output of which would be connected to the rear electrode of the SwiFerr source. For the resistor and capacitor values shown, frequency is approximately 3.8 kHz. Changing capacitance values changes frequency for this oscillator. Gain can be controlled using the high voltage amplifier circuit so output can be controlled.

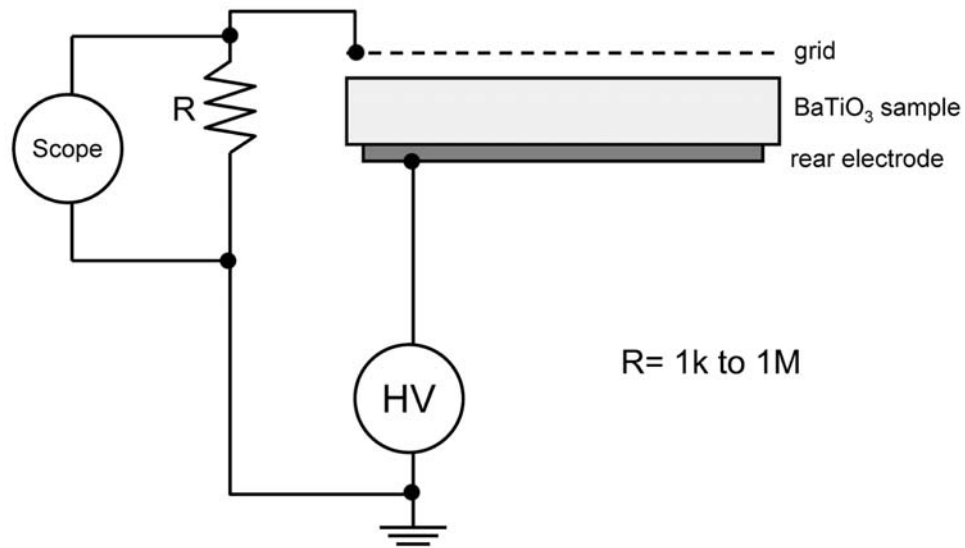


Figure A.4: Circuit for monitoring discharge current in SwiFerr experiment

Schematic for monitoring discharge occurring between the crystal face and grid in a SwiFerr experiment. Current flowing from the grid to ground is detected as voltage across the resistor R , which can vary in value from $1\text{ k}\Omega$ to $100\text{ M}\Omega$. Use lower resistance values for higher frequencies. Waveform for discharge current used to determine discharge width and shape is recorded by the oscilloscope.

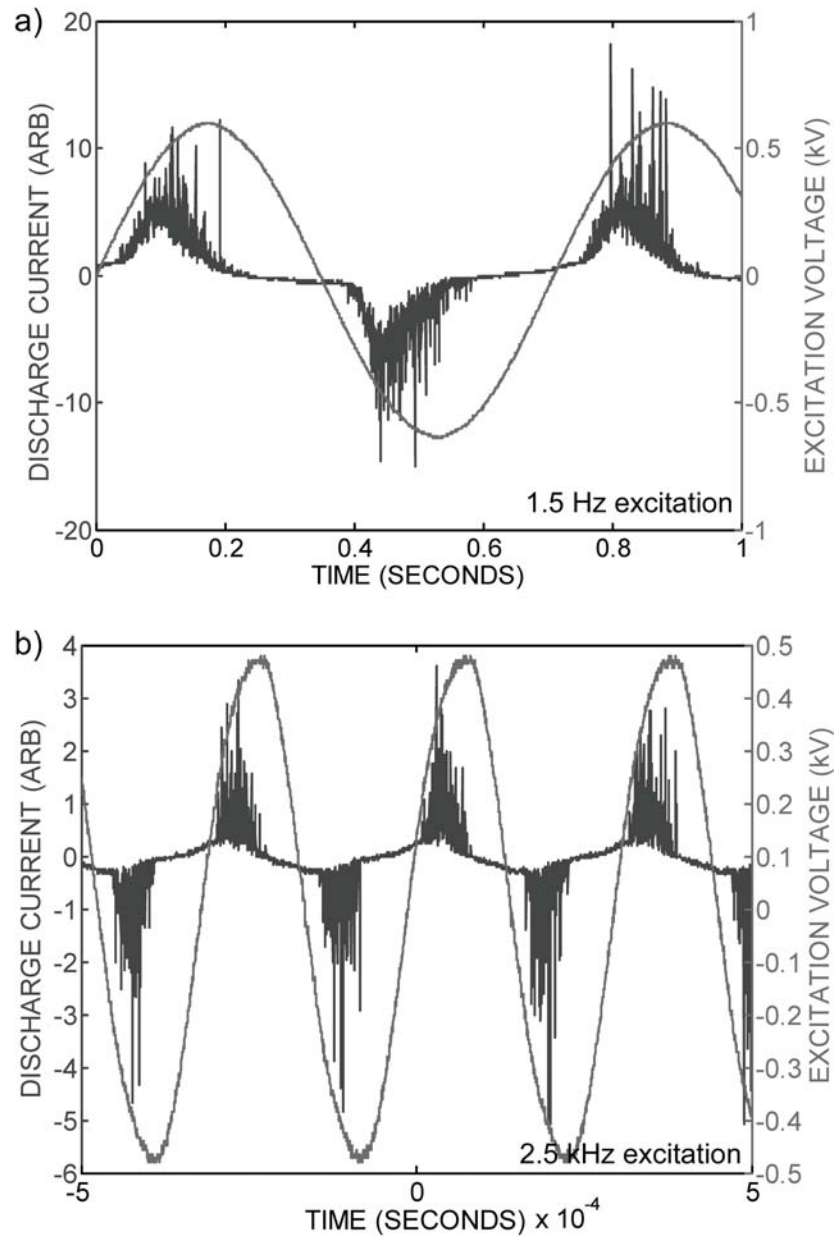


Figure A.5: Discharge profiles for SwiFerr at various frequencies

a) Plot relating excitation waveform of 1.5 Hz to detected discharge. This discharge was also visible to the eye in a dark room. Discharge occurred during each half cycle of excitation, and was approximately 1/4 cycle in length. b) Plot relating excitation waveform of 2.5 kHz to detected discharge. Discharge occurred again during each half cycle of excitation, and was approximately 1/4 cycle in length.

occur for every one excitation cycle. It is the case then that the discharge frequency is twice the excitation frequency. An excitation frequency of 1 kHz gives discharging at a frequency of 2 kHz. For most work with ion trap instruments, this duty cycle is more than sufficient because the sampling rate for an ion trap instrument is on the order of 20 Hz at the fastest, and many ion events take place during a sampling cycle. On other instruments, however, a truly continuous source is needed to achieve detection. If a survey of some of the more common and successful ionization methods for ambient mass spectrometry is performed, it can be seen that all the major techniques are continuous. These include ^{63}Ni , corona discharge, glow discharge, electrospray ionization, DESI, and dielectric barrier discharge.

Since the discharge appears to occur for approximately 1/4 of the excitation wave, a device with three crystals or a crystal with three separate sections should give what appears as a continuous discharge. Figure A.6 shows three waveforms and their resulting discharge traces superimposed, and it can be seen that the appearance of a constant discharge would result. A three-phase excitation waveform, where the phases are either 60 or 120 degrees out of phase, would supply such a device adequately. An additional advantage of this method is that operation at relatively low frequency is possible owing to the fact that the discharge width scales with excitation frequency. As an example, a 60 Hz three-phase waveform would operate the source in this mode. A device where three crystals are present could be constructed just as easily. Since it is the location of the rear electrode and grid that determines where the plasma on the front of the crystal will occur, simply dividing the crystal into sections with sectioned rear electrodes should be sufficient for forming discharge zones on the front of the crystal.

The power supply to operate the ion source in the multi-phase mode is a variant of the design presented previously. Instead of the oscillator previously presented, a three phase oscillator operating at 60 Hz [100] will be employed to feed a stack of three high voltage amplifier boards (Figure A.7). The high voltage amplifier boards (same as the circuit in Figure A.3) will supply the crystals or crystal sections with an AC waveform of frequency 60 Hz, in this case phase separated by 120 degrees. Phases

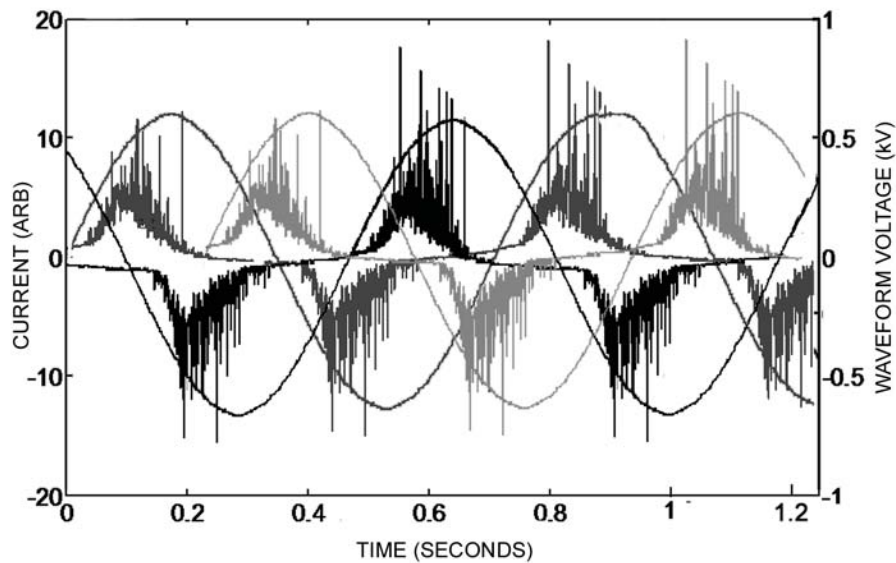


Figure A.6: Simulated three phase excitation and resulting discharge

Simulated three-phase excitation waveform where each phase is separated by 120 degrees, as is common in three-phase waveform generation. The discharge waveforms for each excitation waveform are also plotted, and if such a waveform were applied to the appropriate crystal arrangement a continuous discharge would result. Operation at frequencies as low as 1.5 Hz are apparently possible, and would minimize power consumption in the device. A suggested operational frequency is 60 Hz, as this is a common frequency at which three-phase waveforms are generated.

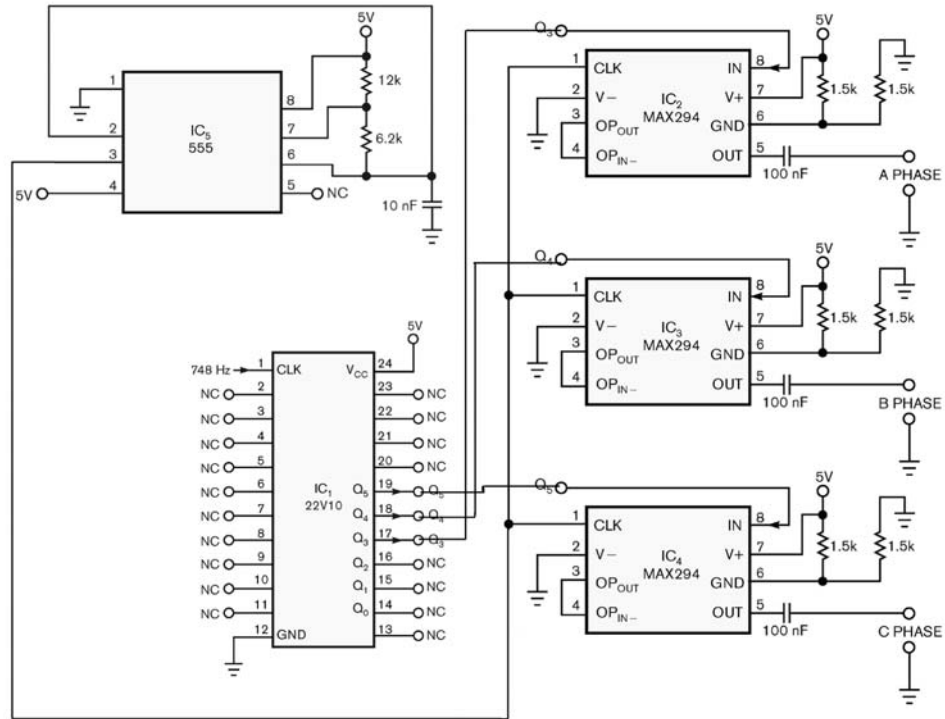


Figure A.7: Schematic for three-phase generator

Schematic for a three-phase generator to be used in a ‘constant discharge mode’ SwiFerr experiment. Phases A, B, and C would then connect to separate high voltage amplifier boards of the same type as in Figure A.3. Then, a self-contained power supply for the operation of SwiFerr in constant discharge mode where the ion source consumes very little power is possible.

A, B, and C will connect to separate high voltage amplifier boards. As before, a peak-to-peak voltage of 900 V will suffice for operation of the source, and adjustment of gain of the high voltage amplifier will allow for application of the proper magnitude voltage.

A.4 Statistical Methods

Here we present the statistical methods used to produce Figure A.2. For each heating rate, a measurement was made where the crystal was heated at a linear rate while ion current was monitored on the Faraday plate in the drift cell. To obtain an average ion production rate for each heating scenario (shown in bold face in each data table), the ion current data were temporally subdivided into ten second intervals and each subdivision manually searched for ion events. Thus, each heating scenario had between 5 and 15 separate determinations of ion production rate. It is already evident from the plots of ion current that production rate is not constant. Rather, more ions are produced near the low temperature boundary of the experiment than near the upper temperature boundary. To achieve statistical significance and gauge measurement error, the averaging was employed. Data statistics for the ion rates in each interval were calculated using the descriptive statistics functionality in Microsoft Excel. Below are the data used to construct Figure A.2. Statistics were run on the “Rate” column to determine the average ion production rate; heating rate was determined using a trendline analysis of the temperature plot (e.g., Figure 1a). Production rates of zero near the beginning or end of the experimental timeframe were omitted from statistical analysis. The descriptive statistics output for the “Rate” column are also shown, so that any reader may evaluate the statistical significance of these data.

Time Span (s)	Ion Events	Rate (Hz)	Test	Result
0-10	4	0.4	Mean	0.32
10-20	3	0.3	Standard Error	0.040473
20-30	5	1	Median	0.3
30-40	4	1	Mode	0.4
40-50	4	0.4	σ	0.156753
50-60	4	0.4	Sample Variance	0.024571
60-70	3	0.3	Kurtosis	1.212922
70-80	7	0.7	Skewness	0.775465
80-90	3	0.3	Range	0.6
90-100	3	0.3	Minimum	0.1
100-110	1	0.1	Maximum	0.7
110-120	4	0.4	Sum	4.8
120-130	2	0.2	Count	15
130-140	1	0.1		
140-150	2	0.2		

Table A.1: Data for .1365 K per second

Time Span (s)	Ion Events	Rate (Hz)	Test	Result
0-10	2	0.2	Mean	0.55
10-20	2	0.2	Standard Error	0.066298
20-30	12	1.2	Median	0.55
30-40	6	0.6	Mode	0.2
40-50	9	0.9	σ	0.281278593
50-60	6	0.6	Sample Variance	0.079117647
60-70	9	0.9	Kurtosis	-0.026171557
70-80	7	0.7	Skewness	0.633392855
80-90	5	0.5	Range	1
90-100	8	0.8	Minimum	0.2
100-110	4	0.4	Maximum	0.2
110-120	7	0.7	Sum	9.9
120-130	4	0.4	Count	18
130-140	4	0.4		
140-150	3	0.3		
150-160	6	0.6		
160-170	3	0.3		
170-180	2	0.2		

Table A.2: Data for .1527 K per second

Time Span (s)	Ion Events	Rate (Hz)	Test	Result
0–10	11	1.1	Mean	0.546667
10–20	7	0.7	Standard Error	0.06822
20–30	8	0.8	Median	0.6
30–40	6	0.6	Mode	0.8
40–50	8	0.8	σ	0.264215
50–60	8	0.8	Sample Variance	0.06981
60–70	4	0.4	Kurtosis	-0.45142
70–80	6	0.6	Skewness	0.405052
80–90	6	0.6	Range	0.9
90–100	5	0.5	Minimum	0.2
100–110	2	0.2	Maximum	1.1
110–120	2	0.2	Sum	8.2
120–130	3	0.3	Count	15
130–140	3	0.3		
140–150	3	0.3		

Table A.3: Data for .1655 K per second

Time Span (s)	Ion Events	Rate (Hz)	Test	Result
0–10	7	0.7	Mean	0.5
10–20	4	0.4	Standard Error	0.071228712
20–30	10	1	Median	0.4
30–40	10	1	Mode	0.4
40–50	5	0.5	σ	0.293683503
50–60	10	1	Sample Variance	0.08625
60–70	7	0.7	Kurtosis	-0.550040508
70–80	6	0.6	Skewness	0.604022025
80–90	4	0.4	Range	0.9
90–100	4	0.4	Minimum	0.1
100–110	3	0.3	Maximum	1
110–120	4	0.4	Sum	8.5
120–130	3	0.3	Count	17
130–140	4	0.4		
140–150	2	0.2		
150–160	1	0.1		
160–140	1	0.1		

Table A.4: Data for .19 K per second

Time Span (s)	Ion Events	Rate (Hz)	Test	Result
0-10	13	1.3	Mean	0.57333
10-20	6	0.6	Standard Error	0.07398
20-30	8	0.8	Median	0.5
30-40	4	0.4	Mode	0.4
40-50	9	0.9	σ	0.286523
50-60	5	0.5	Sample Variance	0.082095
60-70	8	0.8	Kurtosis	1.597419
70-80	4	0.4	Skewness	1.171089
80-90	5	0.5	Range	1.1
90-100	7	0.7	Minimum	0.2
100-110	4	0.4	Maximum	1.3
110-120	4	0.4	Sum	8.6
120-130	3	0.3	Count	15
130-140	3	0.3		
140-150	2	0.2		

Table A.5: Data for .1907 K per second

Time Span (s)	Ion Events	Rate (Hz)	Test	Result
0-10	20	2	Mean	0.966667
10-20	25	2.5	Standard Error	0.178263
20-30	20	2	Median	0.7
30-40	13	1.3	Mode	0.7
40-50	12	1.2	σ	0.690411
50-60	7	0.7	Sample Variance	0.476667
60-70	8	0.8	Kurtosis	0.317774
70-80	7	0.7	Skewness	1.195306
80-90	7	0.7	Range	2.2
90-100	6	0.6	Minimum	0.3
100-110	5	0.5	Maximum	2.5
110-120	5	0.5	Sum	14.5
120-130	4	0.4	Count	15
130-140	3	0.3		
140-150	3	0.3		

Table A.6: Data for .2188 K per second

Time Span (s)	Ion Events	Rate (Hz)	Test	Result
0–10	5	0.5	Mean	0.68
10–20	17	1.7	Standard Error	0.098174
20–30	8	0.8	Median	0.5
30–40	11	1.1	Mode	0.5
40–50	10	1	σ	0.380225
50–60	8	0.8	Sample Variance	0.144571
60–70	9	0.9	Kurtosis	2.558721
70–80	5	0.5	Skewness	1.464182
80–90	5	0.5	Range	1.5
90–100	5	0.5	Minimum	0.2
100–110	4	0.4	Maximum	1.7
110–120	5	0.5	Sum	10.2
120–130	4	0.4	Count	15
130–140	4	0.4		
140–150	2	0.2		

Table A.7: Data for .2651 K per second

Time Span (s)	Ion Events	Rate (Hz)	Test	Result
20–30	8	0.8	Mean	0.85625
30–40	24	2.4	Standard Error	0.154641723
40–50	18	1.8	Median	0.8
50–60	15	1.5	Mode	0.8
60–70	8	0.8	σ	0.618566892
70–80	5	0.5	Sample Variance	0.382625
80–90	13	1.3	Kurtosis	1.366040182
90–100	8	0.8	Skewness	1.198691768
100–110	8	0.8	Range	2.3
110–120	5	0.5	Minimum	0.1
120–130	7	0.7	Maximum	2.4
130–140	8	0.8	Sum	13.7
140–150	4	0.4	Count	16
150–160	1	0.1		
160–170	4	0.4		
170–180	1	0.1		

Table A.8: Data for .27 K per second

Time Span (s)	Ion Events	Rate (Hz)	Test	Result
0-10	0	0.0	Mean	1.025
10-20	0	0.0	Standard Error	0.168201
20-30	14	1.4	Median	1.05
30-40	24	2.4	Mode	1.5
40-50	15	1.5	σ	0.672805
50-60	15	1.5	Sample Variance	0.452667
60-70	16	1.6	Kurtosis	-0.73735
70-80	17	1.7	Skewness	0.236785
80-90	15	1.5	Range	2.3
90-100	12	1.2	Minimum	0.1
100-110	8	0.8	Maximum	2.4
110-120	9	0.9	Sum	16.4
120-130	6	0.6	Count	16
130-140	5	0.5		
140-150	3	0.3		
150-160	1	0.1		
160-170	2	0.2		
170-180	2	0.2		

Table A.9: Data for .3265 K per second

Time Span (s)	Ion Events	Rate (Hz)	Test	Result
0-10	0	0.0	Mean	1.21875
10-20	35	3.5	Standard Error	0.239656
20-30	25	2.5	Median	1.2
30-40	16	1.6	Mode	1.6
40-50	20	2.0	σ	0.958623
50-60	18	1.8	Sample Variance	0.918958
60-70	16	1.6	Kurtosis	0.517609
70-80	16	1.6	Skewness	0.815889
80-90	13	1.3	Range	3.5
90-100	11	1.1	Minimum	0
100-110	6	0.6	Maximum	3.5
110-120	6	0.6	Sum	19.5
120-130	5	0.5	Count	16
130-140	3	0.3		
140-150	4	0.4		
150-160	0	0		
160-170	1	0.1		

Table A.10: Data for .4368 K per second

Time Span (s)	Ion Events	Rate (Hz)	Test	Result
0–10	5	0.5	Mean	2.05
10–20	58	5.8	Standard Error	0.507445
20–30	26	2.6	Median	1.95
30–40	35	3.5	Mode	2.6
40–50	36	3.6	σ	1.75784
50–60	26	2.6	Sample Variance	3.09
60–70	30	3.0	Kurtosis	0.070173
70–80	13	1.3	Skewness	0.754597
80–90	9	0.9	Range	5.7
90–100	6	0.6	Minimum	0.1
100–110	3	0.3	Maximum	5.8
110–120	3	0.3	Sum	24.6
120–130	1	0.1	Count	12

Table A.11: Data for .6447 K per second

Time Span (s)	Ion Events	Rate (Hz)	Test	Result
0–10	0	0.0	Mean	4.58
10–20	40	4.0	Standard Error	0.781921
20–30	55	5.5	Median	5
30–40	65	6.5	Mode	N/A
40–50	50	5.0	σ	1.748428
50–60	19	1.9	Sample Variance	3.057
60–70	8	0.8	Kurtosis	0.832976
70–80	4	0.4	Skewness	-0.89752
80–90	1	0.1	Range	4.6
			Minimum	1.9
			Maximum	6.5
			Sum	22.9
			Count	5

Table A.12: Data for 2.333 K per second

Time Span (s)	Ion Events	Rate (Hz)	Test	Result
0–10	0	0.0	Mean	8.4
10–20	68	6.8	Standard Error	1.6
20–30	100	10	Median	8.4
30–40	30	3	Mode	N/A
40–50	30	3.0	σ	2.2627417
50–60	8	0.8	Sample Variance	5.12
			Kurtosis	NaN
			Skewness	NaN
			Range	3.2
			Minimum	6.8
			Maximum	10
			Sum	16.8
			Count	2

Table A.13: Data for 4 K per second

Appendix B

Pulsed High Voltage Power Supply for Field Induced Droplet Ionization Experiments

B.1 Introduction

The field induced droplet ionization (FIDI) experiment, developed in the Beauchamp laboratory, has proven a robust and useful method for studying interfacial chemistry. Several accounts now exist in the literature [101],[102] whereby reaction products from an interfacial reaction are analyzed using the technique. The experiment, which has been described in detail previously, requires that a liquid droplet (often quiescent and hanging from a stainless steel capillary) be subjected to a pulsed electric field on the order of 10–20 kV/cm. Subjecting the droplet to such fields causes it to elongate and emit jets of smaller charged droplets and ions when the electric field applied is above the critical field for the particular droplet size in the experiment. The droplets are then typically sampled using an ion trap mass spectrometer, resulting in the contents of the droplet being analyzed mass spectrometrically. There is some recent evidence that FIDI has a particular tendency to sample surface species preferentially [103].

To perform the experiment, the electric field is switched on for a period of 5–20 ms. Grimm has determined quite rigorously [104] the timescale of jetting for various sized droplets, and for the hanging droplet FIDI experiment the droplet jetting timescale is between 5 and 10 ms. To achieve this, the previous iteration of this experiment used a

rack of electronics which included two 30 kV high voltage power supplies, a +12V DC and -12V DC power supply, oscilloscope, video monitor, and home-built pulse control electronics. The voltages applied to the liquid supply capillary (often termed 'needle electrode') and back plate electrode were separately controlled using the knobs on the 30 kV supplies, and pulse width was controlled with a knob on the electronics box while the actual pulse width was monitored using the oscilloscope. To pulse the field, a mechanical button was pushed which began a TTL-pulse sequence resulting in the closing of two normally open high voltage relays and the application of high voltage to the back plate and needle. In order to switch from positive to negative high voltage polarity, it was necessary to remove and reinstall a junction block on the back of each of the 30 kV power supplies. In the years after the initial build of these electronics, the experiment suffered reliability problems including the wearing out of the pulsing button, frequent failure of any one of the integrated circuits, and wiring failures owing to the research nature of the experiment (which was originally constructed using Protoboard). It was identified that a more robust and reliable system was needed for the experiment, especially if future automation was a goal. The supply should not be susceptible to damage from a short circuit or electrical arcing occurring in the FIDI source. Ideally, it would be controlled using a simple software interface which allows for the setting of voltage levels and polarity using the software so that no hardware changes are required. In most experiments, it is still desirable to manually control the pulsing of the voltage; that is, determine the moment the voltage pulse occurs using some type of push-button or mechanical trigger which is robust and designed for frequent cycling.

Such an instrument is described here. The current instrument is a significant improvement over the previous with respect to durability, reliability, ease of control, reduction in complexity, and portability. The instrument comprises a three rack unit chassis in which is housed high and low voltage power supplies, control circuitry, and a high voltage relay. Using the current power supply design and a modification of the FIDI source itself, we have reduced the amount of equipment necessary to perform an experiment from 12 rack spaces to three, as well as turning the apparatus into a

bench top instrument which is easily serviceable and considerably simpler than the original embodiment.

B.2 Component Reduction; Supply Changes

The experiment originally required two separate high voltage power supplies for applying potential to the needle and back plate electrodes. In addition, two sets of pulse control electronics and two high voltage relays were required to apply the pulsed potential to the FIDI source. Figure B.1 shows the original block diagram for the experiment. It was identified that independent voltage control for the needle and back plate electrode were not needed, as in practice the needle electrode was maintained at one half the voltage of the back plate electrode. The use of a voltage divider was more appropriate, and reduced the number of control components as well as ensured synchronization of electrode pulsing. Figure B.2 shows the block diagram of the revised experiment, which is currently in use with the new computer-interfaced high voltage supply.

Originally, pulse width was variable so that the time the field was switched on could be varied for different sized droplets. Since in practice the droplets used are of a similar size, and since the jetting process requires a quick switching on of high voltage but not necessarily a switching off of the voltage, a fixed pulse width of 10 ms was chosen and is specified in the block diagram of the LabVIEW virtual instrument that was written to control the revised experiment. This pulse width is sufficient for all droplets used in the experiment, and eliminates the need for a control to change the pulse width as well as eliminating the oscilloscope for pulse width monitoring.

B.3 Description of Instrument

The instrument is a self contained unit capable of supplying pulsed high voltage at levels up to 10 kV, in both positive and negative polarity. It has the capability for “hot” polarity switching using the software interface. The supply has been con-

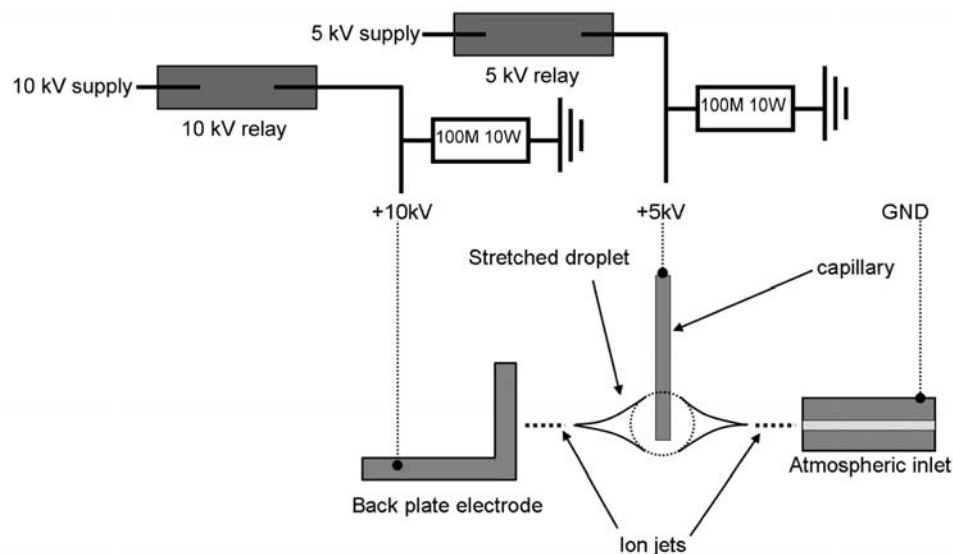


Figure B.1: Original arrangement for supplying high voltage to FIDI source

Original arrangement for supplying high voltage to the FIDI source. Two high voltage relays, fed by two high voltage power supplies and control circuitry, must open and close in unison for effective application of pulsed high voltage to the source. Problems with component failure and pulse synchronization characterized this early embodiment of the experiment.

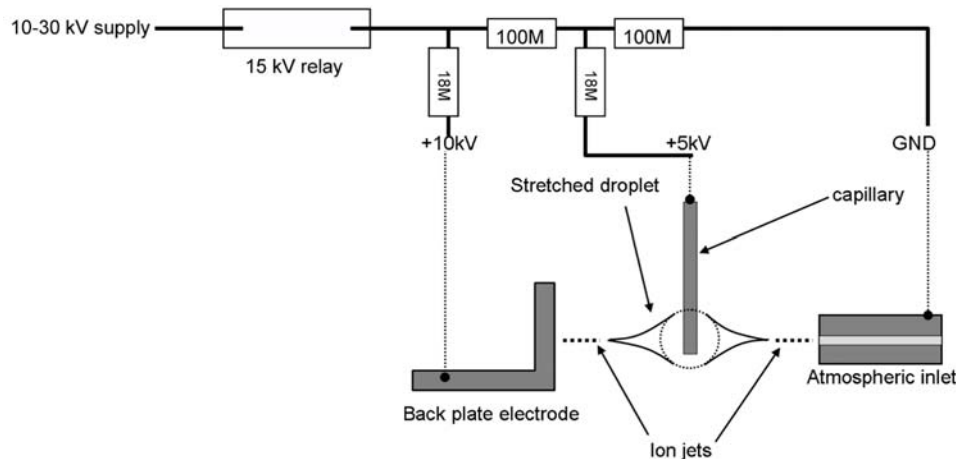


Figure B.2: Revised arrangement for supplying high voltage to the FIDI source

Revised arrangement for supplying high voltage to the FIDI source. A scheme where a voltage divider is employed and the result is a reduction in the number of components needed for operation of the source. Another benefit of the revised arrangement is exact synchronization of pulses to the hanging droplet and back plate. Lastly, the inclusion of current limiting resistors in line with voltage paths helps suppress discharge in the source region.

structed with particular attention to durability, since use in the FIDI experiment often subjects the unit to some level of electrical discharge. The instrument is controlled using a LabVIEW Virtual Instrument from a personal computer. A single high voltage connection to the FIDI source supplies the high voltage necessary for operation. Figure B.3 is a photograph of the instrument. Two switches control main power and power to the high voltage circuitry, and an LCD panel displays the high voltage output level. Connections for high voltage to the FIDI source, ground, and a connector for the computer interface are on the rear panel of the supply. The power input for the supply is 110–120V, 60 Hz single phase.

B.3.1 Global control design

The instrument is controlled using a LabVIEW virtual instrument written for use with the power supply. The software interface has the capability for controlling voltage level from 0–10 kV, polarity, pulsing, as well as an enable/disable function. Figure B.4 is a screen shot of the control interface, showing the control ‘switches’ for polarity and enable/disable, as well as a high voltage control ‘knob’ and pulse initiation button. Currently, pulse length is set directly in the VI block diagram and is not configurable from the VI. It has been found that pulse length for FIDI is not critical with respect to maximum pulse length; so long as the voltage is switched on quickly enough, and left at potential for a sufficient amount of time, the droplet will fission. As a result, pulse length has been set to 10 ms which is sufficient for droplets up to about 2 mm in diameter (smaller droplets require shorter voltage pulses). ‘Hard’ controls include the instrument power and high voltage enable switches. The ability to separately switch off the 30 kV supply presents an element of necessary safety.

B.3.2 Hardware interface

Hardware interfacing between the personal computer used for controlling the instrument and the power supply itself is achieved using National Instruments CompactDAQ hardware. Table B.1 lists the pinouts for the two DB9 connectors and DB15

Signal/Supply	Wire Color	Pin on Rear Pnl DB9	Pin on Breakout DB9	Pin on DB15
Voltage Program 0-10V DC	Red	1	1	2
Voltage Monitor 0-10V DC	Purple	2	2	5
TTL HV Enable/Disable	Blue	3	3	12
TTL Polarity	Yellow	4	4	6
Counter Pulse	White	4	4	6
TTL Common	Black	6	6	—
Monitor Common	Black	7	7	7
Current Monitor	Purple	8	8	13 (not connected)
Voltage Common	Black	9	9	7
Power Ground	Green	—	—	15
No Connection	—	—	—	1,3,4,9,10,11,13,14

Table B.1: Pinouts for FIDI pulsed high voltage supply.

connector on the instrument. Figure B.5 is a block/wiring diagram showing the wiring of the control circuits, including the breakout box which serves to interface the CompactDAQ hardware and its separate inputs and outputs to the DB9 connector to which the interface cable attaches. Figure B.6 is an electrical schematic for the circuit board in the supply. The board is constructed using wire wrap technology for connection reliability. Parts were obtained from the Caltech Electrical Engineering Stockroom. The Chemistry Electronics Shop also has considerable experience in wire wrap if assistance is required.

B.4 Experiment Start-Up Procedures

A specific start-up procedure for the experiment must be followed in order not to damage components on the circuit board. The reason for this is that the logic state in which the LabVIEW TTL module remains idle is occasionally logic LOW. The idle state prescribed by the software is logic HIGH. If stuck in logic LOW, this actuates the high voltage relay and causes current to flow through the voltage divider resistors. Currently, these resistors are 1/4 W rated, yet the current which flows is on the order of watts. Normally, this is not a problem when pulsing is used because this current only flows for a matter of milliseconds, which is not sufficient to heat up and burn the resistors. If stuck in logic LOW, the power dissipated by these resistors exceeds ratings and the resistors burn.

The proper start-up procedure is to load and run the LabVIEW VI entitled 'FIDI.vi,' followed by pressing the PULSE button a few times. This resets the logic, and only then is it safe to turn on the main power switches to the supply.



Figure B.3: Photograph of pulsed power supply

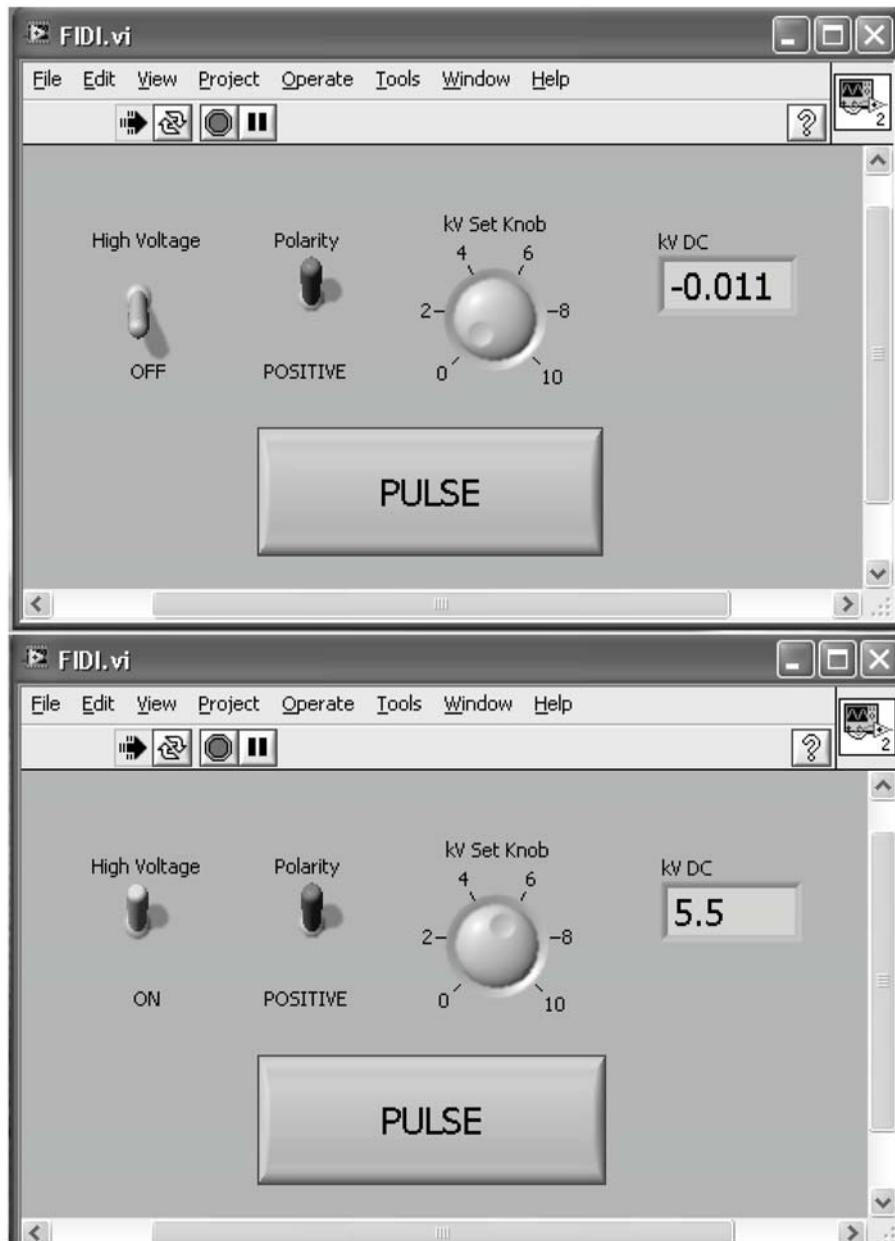


Figure B.4: Screen shot of control program for the experiment

Screen shot of the control program for operating the experiment. Top panel shows the state when high voltage supply is turned off with the software. Bottom panel shows the state when the high voltage supply is switched on using the software. A voltage readout, which is the same as the LCD panel meter on the power supply box itself, is available on the software panel. To apply a pulsed voltage to the source, click the “PULSE” button.

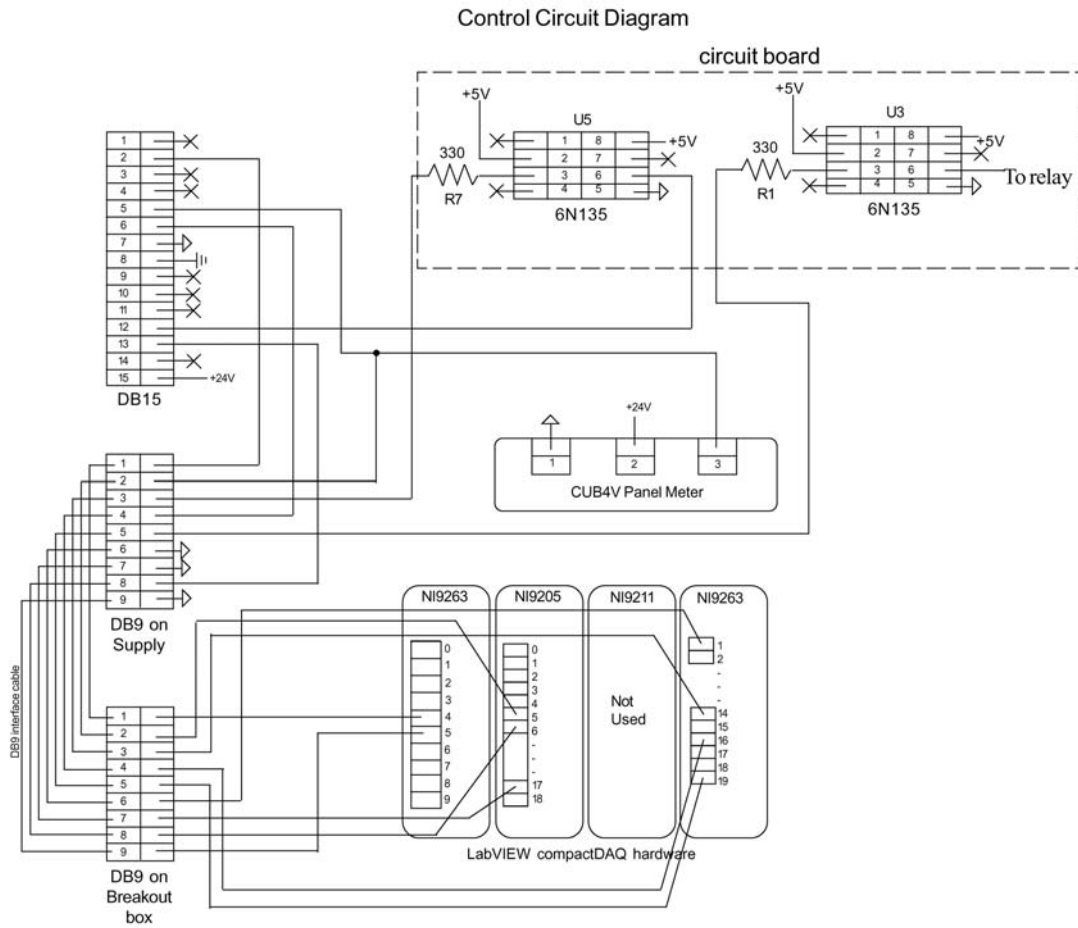


Figure B.5: Control circuitry for FIDI power supply

Bibliography

- [1] Lang, S.B. *Physics Today* **2005**, *August*, 3136.
- [2] Bayssie, M.; Brownridge, J.D.; Kukhtarev, N.; Wang, J.C. *Nucl. Inst. and Meth. in Phys. Res. B* **2005**, *241*, 913–916.
- [3] Geuther, J.A.; Danon, Y. *J. Appl. Phys.* **2005**, *97*, 074109.
- [4] Brownridge, J.D.; Shafroth, S. M. *J. Electrostat.* **2005**, *63*, 249–259.
- [5] Kukhtarev, N.; Kukhtareva, J.D.T.; Bayssie, M.; Wang, J.; Brownridge, J.D. *J. Appl. Phys.* **2004**, *96*, 6794–6798.
- [6] Brownridge, J.D.; Shafroth, S.M. *Appl. Phys. Lett.* **2003**, *83*, 1477–1479.
- [7] Brownridge, J.D.; Shafroth, S.M. *Appl. Phys. Lett.* **2001**, *79*, 3364–3366.
- [8] Brownridge, J.D.; Shafroth, S.M. *Appl. Phys. Lett.* **2001**, *78*, 1158–1159.
- [9] Rosenblum, B.; Braulich, P.; Carrico, J.P. *Appl. Phys. Lett.* **1974**, *25*, 17–19.
- [10] Geuther, J.; Danon, Y. *J. Appl. Phys.* **2005**, *97*, 104916.
- [11] Brownridge, J.D.; Shafroth, S.M. *Appl. Phys. Lett.* **2004**, *85*, 1298–1300.
- [12] Ida, H.; Kawai, J. *Anal. Bioanal. Chem.* **2004**, *379*, 735–738.
- [13] Ida, H.; Kawai, J. *X-Ray Spectrom.* **2005**, *34*, 225–229.
- [14] Brownridge, J.D.; Raboy, S. *J. Appl. Phys.* **1999**, *86*, 640–647.
- [15] Brownridge, J.D. *Nature* **1992**, *358*, 287–288.

- [16] Naranjo, B.; Gimzewski, J.K.; Putterman, S. *Nature* **2005**, *434*, 1115–1117.
- [17] Geuther, J.; Danon, Y.; Saglime, F. *Phys. Rev. Lett.* **2006**, *96*, 054803.
- [18] Sato, H.; Seino, T.; Yamamoto, A.; Torimura, M.; Tao, H. *Chem. Lett.* **2005**, *34*, 1178–1179.
- [19] Lang, S.B. *Sourcebook of Pyroelectricity*. New York: Gordon and Breach, **1974**.
- [20] Neidholdt, E.L.; Beauchamp, J.L. *Anal. Chem.* **2007**, *79*, 3945–3948.
- [21] McLuckey, S.A.; Glish, G.L.; Asano, K.G.; Grant, B.C. *Anal. Chem.* **1988**, *60*, 2220–2227.
- [22] Harrison, W.W.; Hess, K.R.; Marcus, R.K.; King, F.L. *Anal. Chem.* **1986**, *58*, A-341–A-356.
- [23] Mason, R.; Milton, D. *Int. J. Mass Spec. Ion Proc.* **1989**, *91*, 209–225.
- [24] Carroll, D.I.; Dzidic, I.; Stillwell, R.N.; Haegele, K.D.; Horning, E.C. *Anal. Chem.* **1975**, *47*, 2369–2373.
- [25] Na, N.; Zhao, M.; Zhang, S.; Yang, C.; Zhang, X. *J. Am. Soc. Mass Spec.* **2007**, *18*, 1859–1862.
- [26] Steiner, W.E.; Clowers, B.H.; Haigh, P.E.; Hill, H.H. *Anal. Chem.* **2003**, *75*, 6068–6076.
- [27] Steiner, W.E.; English, W.A.; Hill, H.H. *Anal. Chim. Acta* **2005**, *532*, 37–45.
- [28] Steiner, W.E.; Klopsch, S.J.; English, W.A.; Clowers, B.H.; Hill, H.H. *Anal. Chem.* **2005**, *77*, 4792–4799.
- [29] Riley, D.P. *J. Chem. Soc., Chem. Commun.* **1983**, *24*, 1530–1532.
- [30] Riley, D.P.; Correa, P.E. *J. Org. Chem.* **1985**, *50*, 1564–1566.
- [31] Ma, S.; Chowdhury, S.K.; Alton, K.B. *Anal. Chem.* **2005**, *77*, 3676–3682.

- [32] Atkinson, R. *Chem. Rev.* **1985**, *85*, 69–201.
- [33] Cooks, R.G.; Ouyang, Z.; Takats, Z.; Wiseman, J.M. *Science* **2006**, *311*, 1566–1570.
- [34] Laiko, V.V.; Baldwin, M.A.; Burlingame, A.L. *Anal. Chem.* **2000**, *72*, 652–657.
- [35] Laiko, V.V.; Moyer, S.C.; Cotter, R.J. *Anal. Chem.* **2000**, *72*, 5239–5243.
- [36] Sampson, J.S.; Hawkridge, A.M.; Muddiman, D.C. *J. Am. Soc. Mass Spec.* **2006**, *17*, 1712–1716.
- [37] Sheia, J.; Huang, M.; Hsu, H.; Lee, C.; Yuan, C.; Beech, I.; Sunner, J. *Rapid Commun. Mass Spectrom.* **2005**, *19*, 3701–3704.
- [38] Harper, J.D.; Charipar, N.A.; Mulligan, C.C.; Zhang, X.; Cooks, R.G.; Ouyang, Z. *Anal. Chem.* **2008**, *80*, 9097–9104.
- [39] Zhang, Y.; Ma, X.; Zhang, S.; Yang, C.; Ouyang, Z.; Zhang, X. *Analyst* **2009**, *134*, 176–181.
- [40] Cody, R.B.; Laramée, J.A.; Durst, H.D. *Anal. Chem.* **2005**, *77*, 2297–2302.
- [41] Ratcliffe, L.V.; Rutten, F.J.M.; Barrett, D.A.; Whitmore, T.; Seymour, D.; Greenwood, C.; Aranda-Gonzalvo, Y.; Robinson, S.; McCoustra, M. *Anal. Chem.* **2007**, *79*, 6094–6101.
- [42] Van Berkel, G.J.; Pasilis, S.P.; Ovchinnikova, O. *J. Mass Spectrom.* **2008**, *43*, 1161–1180.
- [43] Harris, G.A.; Nyadon, L.; Fernandez, F.M. *Analyst* **2008**, *133*, 1297–1301.
- [44] Guharay, S.K.; Dwivedi, P.; Hill, H.H. *IEEE Trans. Plasma Sci.* **2008**, *36*, 1458–1470.
- [45] Neidholdt, E.L.; Beauchamp, J.L. *Anal. Chem.* **2007**, *79*, 3945–3948.
- [46] Kim, S.; Gopalan, V.; Gruverman, A. *Appl. Phys. Lett.* **2002**, *80*, 2740–2742.

- [47] Gopalan, V.; Mitchel, T.E.; Furukawa, Y.; Kitamura, K. *Appl. Phys. Lett.* **1998**, *72*, 1981–1983.
- [48] Biedrzycki, K.; Markowski, L.; Czapla, Z. *Physica Stat. Sol. A* **1998**, *165*, 283–293.
- [49] Latham, R.V. *Brit. J. Appl. Phys.* **1967**, *18*, 1383–1388.
- [50] Rosenman, G.; Shur, D.; Krasik, Y.E.; Dunaevsky, A. *J. Appl. Phys.* **2000**, *88*, 6109–6161.
- [51] Krasik, Y.E. *IEEE Trans. Plasma. Sci.* **2003**, *31*, 49–59.
- [52] Dunaevsky, A.; Krasik, Ya. E.; Felsteiner, J.; Dorfman, S. *J. Appl. Phys.* **1999**, *85*, 8464–8473.
- [53] Sroubek, Z. *J. Appl. Phys.* **2000**, *88*, 4452–4454.
- [54] Sroubek, Z. *Appl. Phys. Lett.* **2002**, *80*, 838–840.
- [55] Chirko, K.; Krasik, E.; Felsteiner, J. *J. Appl. Phys.* **2002**, *91*, 9487–9493.
- [56] Kusz, J.; Musielok, J.; Wanik, B. *Beitr. Plasmaphysik* **1982**, *22*, 381–386.
- [57] Janus, H.; Kusz, J.; Musielok, J. *Beitr. Plasmaphysic* **1985**, *25*, 277–288.
- [58] Biedrzycki, K. *J. Phys. Chem. Solids* **1991**, *52*, 1031–1035.
- [59] Goly, A.; Lopatka, G.; Wujec, T. *J. Quant. Spectrosc. Radiat. Transfer* **1992**, *47*, 353–358.
- [60] Dixon, R.B.; Sampson, J.S.; Hawkridge, A.M.; Muddiman, D.C. *Anal. Chem.* **2008**, *80*, 5266–5271.
- [61] Eiceman, G.A.; Krylov, E.V.; Krylova, N.S.; Nazarov, E.G.; Miller, R.A. *Anal. Chem.* **2004**, *76*, 4937–4934.
- [62] Stubbe, J.; van der Donk, W.A. *Chem. Rev.* **1998**, *98*, 705–762.

- [63] Stadtman, E.R. *Ann. Rev. Biochem.* **1993**, *62*, 797–821.
- [64] Hensley, K.; Carney, J.M.; Mattson, M.P.; Aksenova, M.; Harris, M.; Wu, J.F.; Floyd, R.A.; Butterfield, D.A. *Proc. Nat. Acad. Sci.* **1994**, *91*, 3270–3274.
- [65] Murakami, K.; Irie, K.; Ohgashi, H.; Hara, H.; Nagao, M.; Shimizu, T.; Shirasawa, T. *J. Am. Chem. Soc.* **2005**, *127*, 15168–15174.
- [66] Garrison, W.M. *Chem. Rev.* **1987**, *87*, 381–398.
- [67] Guan, J.-Q.; Almo, S.C.; Chance, M.R. *Chem. Res.* **2004**, *37*, 221–229.
- [68] Maleknia, S.D.; Brenowitz, M.; Chance, M.R. *Anal. Chem.* **1999**, *71*, 3965–3973.
- [69] Wee, S.; O’Hair, R.A.J.; McFadyen, W.D. *Int. J. Mass Spectrom.* **2004**, *234*, 101–122.
- [70] Bagheri-Majdi, E.; Ke, Y.; Orlova, G.; Chu, I.K.; Hopkinson, A.C.; Siu, K.W.M. *J. Phys. Chem. B* **2004**, *108*, 11170–11181.
- [71] Barlow, C.K.; Wee, S.; McFayden, W.D.; O’Hair, R.A.J. *Dalton Trans.* **2004**, 3199–3204.
- [72] Gatlin, C.L.; Turecek, F.; Vaisar, T. *J. Am. Chem. Soc.* **1995**, *117*, 3637–3638.
- [73] Chu, I.K.; Rodriguez, C.F.; Lay, T.-C.; Hopkinson, A.C.; Siu, K.W.M. *J. Phys. Chem. B* **2000**, *104*, 3393–3397.
- [74] Barlow, C.K.; McFayden, W.D.; O’Hair, R.A.J. *J. Am. Chem. Soc.* **2005**, *127*, 6109–6115.
- [75] Zubarev, R.A.; Kelleher, N.L.; McLafferty, F.W. *J. Am. Chem. Soc.* **1998**, *120*, 3265–3266.
- [76] Zubarev, R.A.; Horn, D.M.; Fridriksson, E.K.; Kelleher, N.L.; Kruger, N.A.; Lewis, M.A.; Carpender, B.K.; McLafferty, F.W. *Anal. Chem.* **2000**, *72*, 563–573.

- [77] Mirgorodskaya, E.; Roepstorff, P.; Zubarev, R.A. *Anal. Chem.* **1999**, *71*, 4431–4436.
- [78] Stensballe, A.; Jensen, O.N.; Olsen, J.V.; Haselmann, K.F.; Zubarev, R.A. *Rapid Commun. Mass Spectrom.* **2000**, *14*, 1793–1800.
- [79] Heeren, R.M.A.; Kleinnijenhuis, A.J.; McDonnell, L.A.; Mize, T.H. *Anal. Bioanal. Chem.* **2004**, *378*, 1048–1058.
- [80] Masterson, D.S.; Yin, H.; Chacon, A.; Hachey, D.L.; Norris, J.L.; Porter, N.A. *J. Am. Chem. Soc.* **2004**, *126*, 720–721.
- [81] Ly, T.; Julian, R.R. *J. Am. Chem. Soc.* **2008**, *130*, 351–358.
- [82] Diedrich, J.; Julian, R.R. *J. Am. Chem. Soc.* **2008**, *130*, 12212–12213.
- [83] Hodyss, R.P.; Cox, H.A.; Beauchamp, J.L. *J. Am. Chem. Soc.* **2005**, *127*, 12436–12437.
- [84] Ly, T.; Julian, R.R. *Angew. Chem. Int. Ed.* **2009**, *48*, 7130–7137.
- [85] Biemann, K., “Appendix 5.” *Methods in Enzymology* **1990**, *193*, 886–887.
- [86] Moore, B.; Ly, T.; Julian, R.R. *J. Am. Chem. Soc.* **2009**. (*submitted for publication*).
- [87] Kaminskaya, N.V.; Kostic, N.M. *Inorg. Chem.* **2000**, *40*, 2368–2377.
- [88] Parac, T.N.; Kostic, N.M. *J. Am. Chem. Soc.* **1996**, *118*, 51–58.
- [89] Zhu, L.; Kostic, N.M. *Inorg. Chim. Acta.* **2002**, *339*, 104–110.
- [90] Pu, D.; Vincent, J.B.; Cassady, C.J. *J. Mass Spectrom.* **2008**, *43*, 773–781.
- [91] Tsaprailis, G.; Nair, H.; Zhong, W.; Kuppannan, K.; Futrell, J.; Wysocki, V. *Anal. Chem.* **2004**, *76*, 2083–2094.
- [92] Kish, M.; Wesdemiotis, C. *Int. J. Mass Spectrom.* **2003**, *227*, 191–203.

- [93] Bailey, T.H.; Laskin, J.; Futrell, J.H. *Int. J. Mass Spectrom.* **2003**, *222*, 313-327.
- [94] Harrison, A.G. *J. Mass Spectrom.* **2003**, *38*, 174-187.
- [95] Tsapraillis, G.; Somogyi, A.; Nikolaev, E.N.; Wysocki, V.H. *Int. J. Mass Spectrom.* **2000**, *195/196*, 467-479.
- [96] Neidholdt, E.L. "Design and Testing of Prototype Ambient Pressure Pyroelectric Ionization Source for Use with Differential Mobility Spectrometry," Technical report. Walnut, CA: Ionfinity LLC, **2008**.
- [97] Neidholdt, E.L. "Testing of APPIS with DMS; Sensitivity Measurements with APPIS; and Ion Drift Cell Experiments," Technical report. Walnut, CA: Ionfinity LLC, **2009**.
- [98] Lucas, J.S. "Unusual sinewave generator." *Wireless World* **1977**, *May*, 81.
- [99] Tsai, J.-I.; Shieh, J.-M.; Liao, T.-S.; Teng, C.-C. "High-voltage amplifier uses simplified circuit." *Electronics Design, Strategy, News (EDN)* **2004**, *October 14*, 110.
- [100] Perez-Lobato, E. "Three-phase sinusoidal-waveform generator uses PLD." *Electronics Design, Strategy, News (EDN)* **2006**, *October 12*, 104-106.
- [101] Grimm, R.L.; Hodyss, R.P.; Beauchamp, J.L. *Anal. Chem.* **2006**, *78*, 3800-3806.
- [102] Kim, H.I.; Kim, H.; Shin, Y.S.; Beegle, L.W.; Jang, S.S.; Neidholdt, E.L.; Goddard, W.A.; Heath, J.R.; Kanik, I.; Beauchamp, J.L. *J. Am. Chem. Soc.* **2010** (article in press).
- [103] Jia, T.Z.; Neidholdt, E.L.; Sohn, C.H.; Beauchamp, J.L. *Anal. Chem.* **2009** *in preparation*
- [104] Grimm, R.L.; Beauchamp, J.L. *J. Phys. Chem. B* **2005**, *109*, 8244-8250.